Strojniški vestnik

Journal of Mechanical Engineering

Since 1955

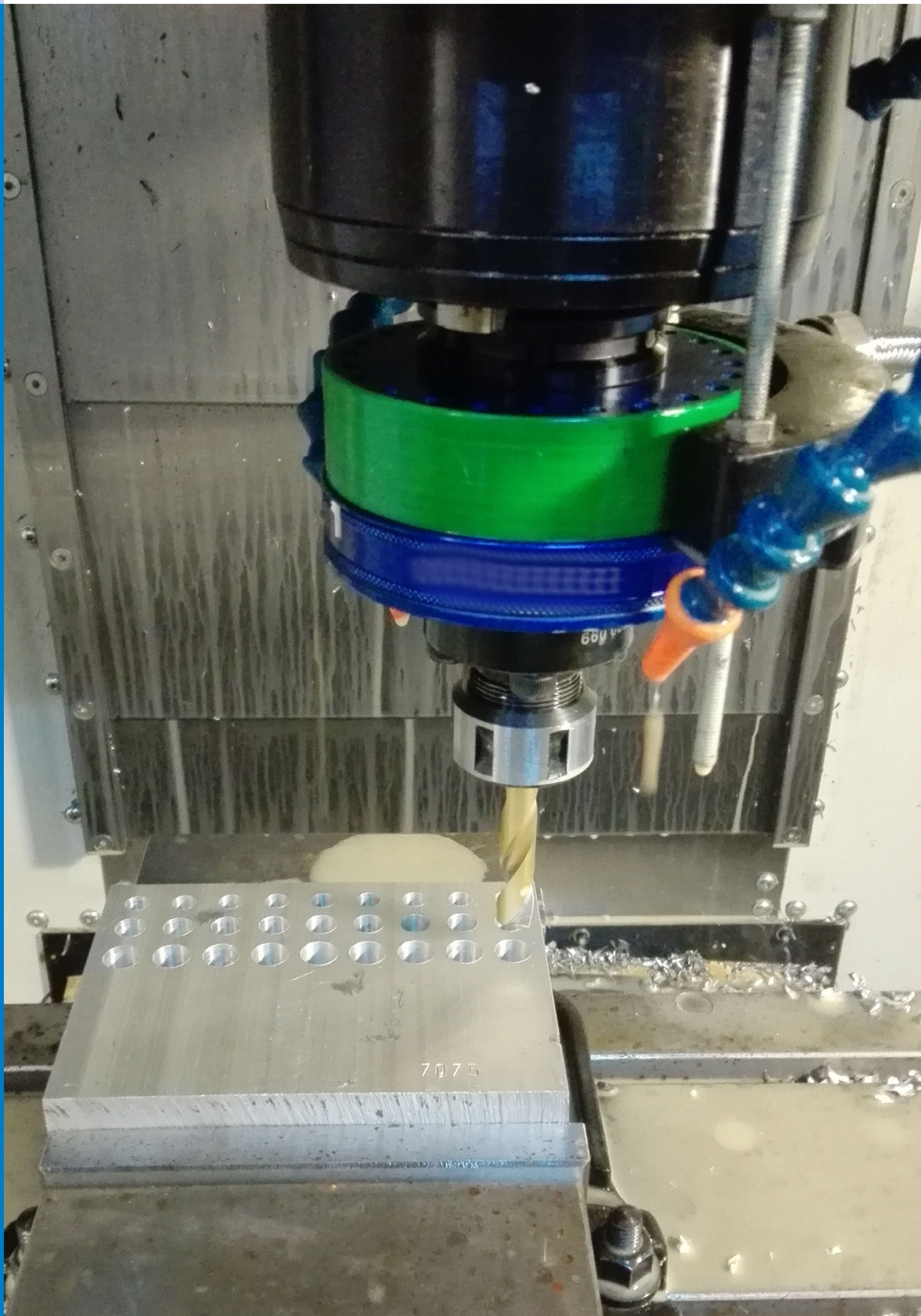

no. 6

year 2018

volume 64

Strojniški vestnik – Journal of Mechanical Engineering (SV-JME)

Aim and Scope

The international journal publishes original and (mini)review articles covering the concepts of materials science, mechanics, kinematics, thermodynamics, energy and environment, mechatronics and robotics, fluid mechanics, tribology, cybernetics, industrial engineering and structural analysis.
The journal follows new trends and progress proven practice in the mechanical engineering and also in the closely related sciences as are electrical, civil and process engineering, medicine, microbiology, ecology, agriculture, transport systems, aviation, and others, thus creating a unique forum for interdisciplinary or multidisciplinary dialogue.
The international conferences selected papers are welcome for publishing as a special issue of SV-JME with invited co-editor(s).

Editorial Office
University of Ljubljana, Faculty of Mechanical Engineering
SV-JME, Aškerčeva 6, SI-1000 Ljubljana, Slovenia
Phone: 386 (0)1 4771 137
Fax: 386 (0)1 2518 567
info@sv-jme.eu, http://www.sv-jme.eu

Print: Abografika, printed in 300 copies

Founders and Publishers
University of Ljubljana, Faculty of Mechanical Engineering, Slovenia
University of Maribor, Faculty of Mechanical Engineering, Slovenia
Association of Mechanical Engineers of Slovenia
Chamber of Commerce and Industry of Slovenia, Metal Processing Industry Association

Cover:
Experimental investigation of thrust force (*Fz*) and torque (*Mz*) values during the drilling tests of Al7075 workpiece material are presented. A full factorial set of tests was performed for all the combinations of different cutting speeds, feed rates and solid carbide tool diameters. Experiments were performed in cooperation with the University of Zaragoza and Centre of Professional Training "Corona de Aragón".

Image Courtesy: Nikolaos Efkolidis, Department of Design and Manufacturing Engineering, University of Zaragoza, Spain

ISSN 0039-2480

General information

Strojniški vestnik – Journal of Mechanical Engineering is published in 11 issues per year (July and August is a double issue).

Institutional prices include print & online access: institutional subscription price and foreign subscription €100,00 (the price of a single issue is €10,00); general public subscription and student subscription €50,00 (the price of a single issue is €5,00). Prices are exclusive of tax. Delivery is included in the price. The recipient is responsible for paying any import duties or taxes. Legal title passes to the customer on dispatch by our distributor.

Single issues from current and recent volumes are available at the current single-issue price. To order the journal, please complete the form on our website. For submissions, subscriptions and all other information please visit: *http://en.sv-jme.eu/*.

You can advertise on the inner and outer side of the back cover of the journal. The authors of the published papers are invited to send photos or pictures with short explanation for cover content.

We would like to thank the reviewers who have taken part in the peer-review process.

The journal is subsidized by Slovenian Research Agency.

Strojniški vestnik - Journal of Mechanical Engineering is available on http://www.sv-jme.eu, where you access also to papers' supplements, such as simulations, etc.

Contents

Strojniški vestnik - Journal of Mechanical Engineering
volume 64, (2018), number 6
Ljubljana, June 2018
ISSN 0039-2480

Published monthly

Papers

Strojniški vestnik - Journal of Mechanical Engineering 64(2018)6, 351-361

DOI:10.5545/sv-jme.2017.5188
Original Scientific Paper
Received for review: 2017-12-29
Received revised form: 2018-03-15
Accepted for publication: 2018-04-11

Modelling and Prediction of Thrust Force and Torque in Drilling Operations of Al7075 Using ANN and RSM Methodologies

Nikolaos Efkolidis[1,*] – César García Hernández[1] – José Luis Huertas Talón[1] – Panagiotis Kyratsis[2]
[1]University of Zaragoza, Department of Design and Manufacturing Engineering, Spain
[2]Western Macedonia University of Applied Sciences, Department of Mechanical Engineering & Industrial Design, Greece

Many developed approaches for the improvement of sustainability during machining operations; one of which is the optimized utilization of cutting tools. Increasing the efficient use of cutting tool results in better product quality and longer tool life. Drilling is one of the most popular manufacturing processes in the metal-cutting industry. It is usually carried out at the final steps of the production process. In this study, the effects of cutting parameters (cutting velocity, feed rate) and tool diameter on thrust force (Fz) and torque (Mz) are investigated in the drilling of an Al7075 workpiece using solid carbide tools. The full factorial experimental design is implemented in order to increase the confidence limit and reliability of the experimental data. Artificial neural networks (ANN) and response surface methodology (RSM) approaches are used to acquire mathematical models for both the thrust force (Fz) and torque (Mz) related to the drilling process. RSM- and ANN-based models are compared, and it is clearly determined that the proposed models are capable of predicting the thrust force (Fz) and torque (Mz). Nevertheless, the ANN models estimate in a more accurate way the outputs used in comparison to the RSM models.
Keywords: sustainable manufacturing, Al7075, artificial neural networks, response surface methodology, thrust force, torque

Highlights
- *Investigations of the effects of cutting parameters (cutting velocity, feed rate) and tool diameter on thrust force (Fz) and torque (Mz) in the drilling of an Al7075 workpiece using solid carbide tools are performed.*
- *Artificial neural networks (ANN) and response surface methodology (RSM) approaches are used to acquire mathematical models.*
- *RSM and ANN models are capable of predicting the thrust force (Fz) and torque (Mz) to a great extent.*
- *ANN models estimate in a more accurate way the outputs used in comparison to the RSM models.*

0 INTRODUCTION

Drilling is an essential part of processes used in subtractive manufacturing for achieving the desired products. Its massive usage requires that any parameter optimization in the process promotes the efficiency and the greener machining. Cutting tool technology is considered one of the most significant impact factors on the sustainability of machining processes and systems. Therefore, the best choice of cutting tools and parameters for the quality of the products and the tool life criterion are both critical for the sustainability metrics of a drilling process. The correct usage of the cutting tool can affect the reduction of needed resources and energy for the production of a new one. Aluminium alloy 7075 (Al7075) is suitable for a variety of specific applications in the aerospace and chemical industries because of its excellent mechanical properties. Its strength, which is comparable to many steels and its excellent corrosion resistance are the main reasons that researchers focus on it [1] to [3]. The chemical composition of Al7075 is given in Table 1.

The development of an appropriate cutting factor analytical model is challenging. Nevertheless, there is much research developed about the suitability of different empirical models to predict different factors during several cutting processes. A number of methods, such as artificial neural networks (ANN) and response surface methodology (RSM), have been developed for modelling many manufacturing parameters. The successful application of ANN for prediction and modelling purposes in several science and engineering domains is substantial. ANN is utilized for modelling and prediction purposes due to its advantages in non-linear response and when time variability occurs. It covers the difficulty in inferring input/output mapping [4] and [5] and the search algorithms for optimization, based on genetic and evolution principles [6] to [8]. RSM is a reliable statistical tool for the mathematical modelling of engineering systems and for the optimization of different manufacturing processes.

Table 1. Chemical composition of Al7075

Elements	Zn	Mg	Cu	Cr	Fe	Si	Mn	Ti	Al
Percentage	6	3	2	0.3	0.6	0.5	0.4	0.3	Balance

*Corr. Author's Address: University of Zaragoza, Department of Design and Manufacturing Engineering, Spain. efkolidi@unizar.es

It has been considered to be useful with minimum knowledge about the process under consideration, while simultaneously reducing the resources needed for experiments. It is an appropriate methodology when many factors and interactions affect the desired responses for a given process and an effective technique for evaluating the process parameters with the least number of experiments [9] to [12].

The present paper deals with the study of the drilling process of Al7075 when using solid carbide tools. A series of different diameters were used, together with a number of different cutting speeds and feed rates. A complete set of experimental work was implemented, and different mathematical models of the thrust force and torque developed were calculated. Both RSM and ANN methodologies were applied, and although their results were highly accurate, the ANN model was more effective.

1 METHODS

As mentioned before, a number of researchers have focused on the development of empirical models to predict different factors during several cutting processes. Nouioua et al. [13] developed ANN and RSM models related to cutting force and surface roughness during the turning process of X210Cr12 steel under dry, wet, and MQL machining. Multilayer-coated tungsten carbide inserts with various nose radii were used for the experiment. Measurements were taken combining cutting speed, feed rate, and cutting depth. The comparison between ANN and RSM models showed that ANN models are more accurate for the prediction of surface roughness and cutting force. Kumar and Chauhan [14] used RSM and ANN methodologies in turning, for the validation of the results obtained during experimentation and the prediction of the behaviour of the system under any condition within the operating range. Al7075 hard ceramic composite and Al7075 hybrid composite were under investigation according to the effect of cutting parameters (cutting speed, feed rate, and approach angle) on roughness, using a polycrystalline diamond tool (PCD).

Furthermore, RSM, ANN and support vector regression (SVR) in turning operations were used [15] for the development of empirical models for predicting surface roughness, tool wear, and power required. These response parameters were mainly dependent upon cutting velocity, feed, and cutting time. The result was that ANN and SVR models are much better than RSM models for predicting the three response parameters. ANN and multiple regression approaches were also used for the measurement of the surface roughness of AISI 1040 steel during turning at different cutting parameters, including speed, feed, and depth of cut [16]. The full factorial experimental design was implemented to increase the confidence limit and reliability of the experimental data. Finally, it was proved that the ANN model estimated the surface roughness more accurately than the multiple regression model did.

Many researchers have inestigated the appropriateness of different empirical models to predict burr size during drilling. Karnik et al. [17] described the comparison of the burr size predictive models based on ANN and RSM on AISI 316L stainless steel workpiece with cutting speed, feed and point angle as the critical parameters. The comparison showed that the ANN models provide more accurate predictions than the RSM models do. The result was the same for Çiçek et al. [18] for the investigation of the effects of cutting parameters (i.e. cutting speed, feed rate) and deep cryogenic treatment on thrust force in the drilling of AISI 316 stainless steel. Using the same techniques Mayyas et al. [19] investigated the influence of cutting speed, feed and volume fraction of the reinforcement particles used on the thrust force and torque in the drilling processes of self-lubricated hybrid composite materials. While Bajić et al. [20] examined the influence of three cutting parameters (cutting speed, feed per tooth and depth of cut) on surface roughness, tool wear and cutting force components in a face milling as part of the off-line process control. Alharthi et al. [21] developed ANN and regression analysis models for the prediction of surface roughness in a face milling of an AZ61 magnesium alloy workpiece, for different spindle speed [rpm], depth of cut [mm], and table feed [mm/min]. The coefficient of determination was found to be sufficiently accurate for the best neural network and regression analysis model from the comparison of the models with thirteen experimental validation tests.

Rooki et al. [22] described a simple and more reliable ANN method and multiple linear regressions (MLR) for the prediction of cutting concentration during foam drilling operation. The results indicated the high ability in the prediction of ANN methods. Kahraman [23] investigated the predictability of penetration rate for the diamond drilling from the operational variables and the rock properties, such as the uniaxial compressive strength, the tensile strength and the relative abrasiveness. Finally, Chavoshi [24] using methods, such as regression analysis (RA), ANN, and co-active neuro-fuzzy inference system (CANFIS) attempted to predict the surface roughness, material removal rate, and over-cut of SAE-XEV-F valve-steel during electrochemical drilling in NaCl and NaNo3 electrolytic processes.

2 EXPERIMENTAL

2.1 Experimental Settings

In this study, an Al7075 plate was used as the workpiece material (150 mm × 150 mm × 15 mm). The drilling tests were performed using a HAAS VF1 CNC machining centre with continuous speed and feed control within their boundaries. The cutting forces were measured by utilizing a Kistler four components dynamometer (type 9123) with all the appropriate accessories. The dynamometer signals were processed via charge amplifiers and an A/D converter to a personal computer. The measured thrust force and torque were displayed and analysed to implement an early error detection strategy.

During the drilling tests, thrust force (*Fz*) and torque (*Mz*) values were measured in 36 experiments which were performed by using solid carbide drill tools (Kennametal - multilayer TiAlN-PVD-coated universal fine-grain grade). Fig. 1 shows details of the cutting tool geometry.

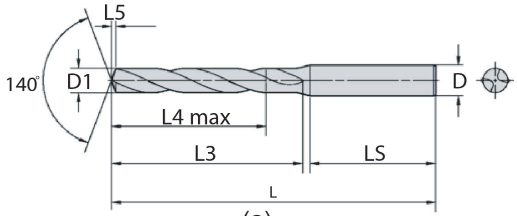

(a)

Catalogue number	(L4) max drill depth [mm]	(L3) flute length [mm]	(LS) flute length [mm]	(D) shank diameter [mm]
B041A08000CPG	29	41	36	8
B041A10000CPG	35	47	40	10
B041A10000CPG	40	55	45	12
B041A10000CPG	43	60	45	14

(b)

Fig. 1. *Cutting tool; a) geometry details; and b) dimensions*

The cutting tools are not through coolant category tools; therefore, coolant fluid (90 % water,

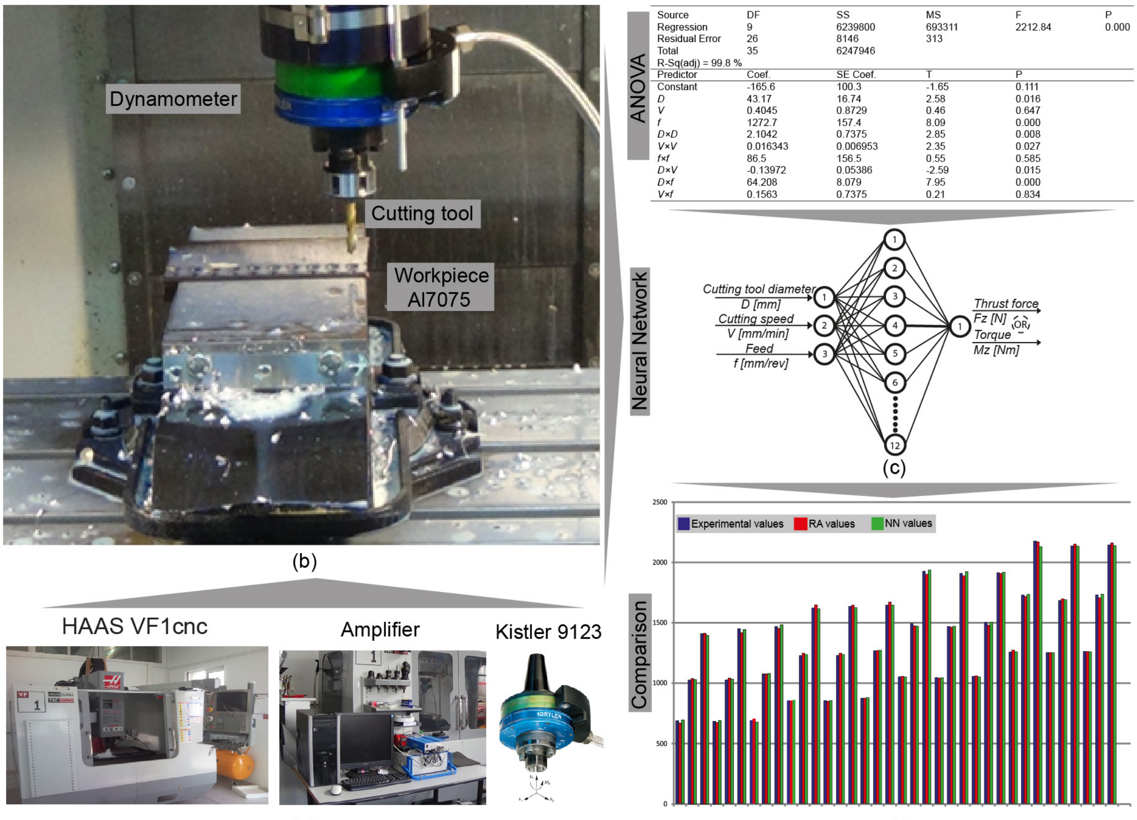

Fig. 2. *Experimental workflow; a) The required hardware equipment, b) Drilling process, c) Development of mathematical models, d) Comparison between experimental and predicted values for thrust force and cutting torque*

10 % KOOLRite 2270 coolant) was provided by the delivery system near the cutting tool. The feed rates of 0.2 mm/rev, 0.4 mm/rev, and 0.6 mm/rev were used together with cutting velocity values of 10 m/min, 40 m/min, and 70 m/min. The constant depth of the holes drilled was 15 mm. The full factorial set of tests was performed for all the combinations of cutting speeds, feed rates, and tool diameters. The workflow of the research is depicted in Fig. 2 and the cutting parameters, units, and notations are listed in Table 2.

Table 2. *Cutting variables used in the experiments*

Parameters	Values
Cutting velocity, V [m/min]	10, 40 ,70
Feed rate, f [mm/rev]	0.2, 0.4, 0.6
Tool diameter, D [mm]	8, 10, 12, 14
Axial depth of cut, a_p [mm]	15
Workpiece dimension [mm]	150 × 150 × 15

Fig. 3 expresses the evolution of thrust force and the cutting torque related to different feed rates and cutting speeds. According to the graph, it can be seen that when the tool diameter increases, both the thrust force and the cutting torque values are increased as expected. The same happens in the case of the feed rate. As feed rate values are increased, the thrust force and the cutting torque are then increased respectively. In contrast, the different values of cutting speed do not noticeably affect the experimental values. The importance of cutting tool diameter and feed rate is much greater than that of cutting speed related to thrust force and cutting torque.

2.2 RSM-Based Predictive Models

The RSM is an accurate tool used to check the influence of a series of input variables on the response when studying a complex phenomenon. The models produced use the least square fitting in order to provide a reliable mathematical model. In this case, a full factorial strategy was followed, 36 drilling experiments were performed, and both the thrust force and torque were modelled using polynomial

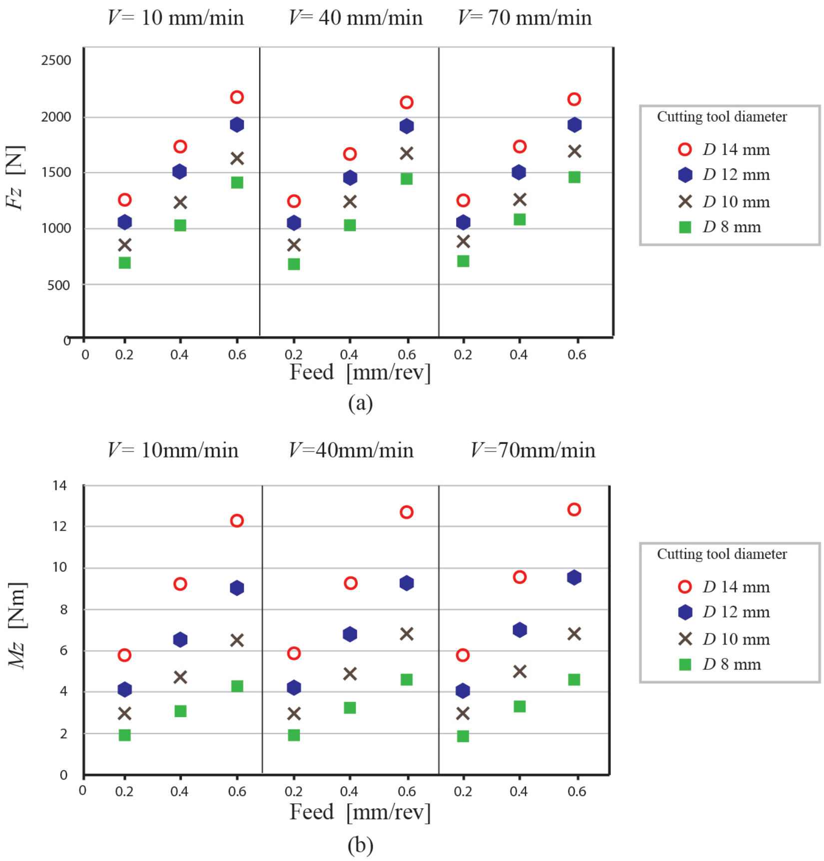

Fig. 3. *Experimental values derived from Kistler 9123, a) Fz and b) Mz*

mathematical models. The following form was selected for this case:

$$Y = b_0 + b_1 X_1 + b_2 X_2 + b_3 X_3 + b_4 X_4 + b_{11} X_1^2 + b_{22} X_2^2 + b_{33} X_3^2 + b_{44} X_4^2 + b_{12} X_1 X_2 + b_{13} X_1 X_3 + b_{14} X_1 X_4 + b_{23} X_2 X_3 + b_{24} X_2 X_4 + b_{34} X_3 X_4, \quad (1)$$

where Y is the response, X_i stands for the coded values and b_0, …, b_{34} stand for the models' regression coefficients.

Based on this mathematical model, the data acquired formed the following equations for the thrust forces [N] and the torque [Nm] respectively:

$$Fz = -166 + 43.2\,D + 0.405\,V + 1273\,f + 2.10\,D\times D + 0.0163\,V^2 + 86\,f^2 - 0.140\,D\times V + 64.2\,D\times f + 0.156\,V\times f \quad (2)$$

and

$$Mz = 4.52 - 0.913\,D - 0.00502\,V - 7.31\,f + 0.0548\,D\times D - 0.000046\,V^2 - 1.39\,f^2 + 0.000405\,D\times V + 1.73\,D\times f + 0.0197\,V\times f \quad (3)$$

where D is the tool diameter [mm], f is the feed rate [mm/rev], and V is the cutting speed used [m/min] and solid carbide tools and Al7075 workpiece.

The adequacy of the models is provided at a 5 % level of significance. ANOVA was used for establishing the validity of the developed models. The calculated values of the F-ratio of the developed models (Tables 3 and 4), are significantly increased compared to the tabulated value of the F-table at a 95 % confidence level (2212.84 for the Fz and 2908.77 for the Mz), while the P-values are 0.000, which proves the highest correlation between data and model in each case. The validity of the models is also proved because the R-sq(adj) is very high in both cases (99.8 % for the Fz and 99.9 % for the Mz). In addition, the significant terms of the models, when a level of significance of 5 % is used, are those with a P-value less than 0.05. For the Fz these factors are: D (P = 0.016), f (P = 0.000), $D\times D$ (P = 0.008), $V\times V$ (P = 0.015) and $D\times f$ (P = 0.000), while for the Mz the significant terms are: D (P = 0.000), f (P = 0.000), D^2 (P = 0.000), $D\times f$ (P = 0.000), $V\times f$ (P = 0.000).

Residual analysis was performed to test the models' accuracy; in both cases, the residuals follow the normal distribution. They follow straight lines (almost linear patterns) proving that the errors follow the normal distribution. All the scatter diagrams of the Fz and Mz residuals versus the fitted values depict that the residuals are evenly distributed on both sides of the centreline.

The same is true for the residuals versus the order of the data (see Fig. 4). The accuracy achieved is very high when comparing the measured values and those calculated from the mathematical models (3 % and 5.6 %, respectively). The derived mathematical models can be considered to be very accurate and can be used directly for predicting both the thrust force and the cutting torque within the limits of the tool diameter, feed rate, and cutting speed used.

Table 3. *ANOVA table for the Fz (thrust force)*

Source	DF	SS	MS	F	P
Regression	9	6239800	693311	2212.84	0.000
Residual Error	26	8146	313		
Total	35	6247946			
R-Sq(adj) = 99.8 %					

Predictor	Coef.	SE Coef.	T	P
Constant	–165.6	100.3	–1.65	0.111
D	43.17	16.74	2.58	0.016
V	0.4045	0.8729	0.46	0.647
f	1272.7	157.4	8.09	0.000
$D\times D$	2.1042	0.7375	2.85	0.008
$V\times V$	0.016343	0.006953	2.35	0.027
$f\times f$	86.5	156.5	0.55	0.585
$D\times V$	–0.13972	0.05386	–2.59	0.015
$D\times f$	64.208	8.079	7.95	0.000
$V\times f$	0.1563	0.7375	0.21	0.834

Table 4. *ANOVA table for the Mz (torque)*

Source	DF	SS	MS	F	P
Regression	9	322.187	35.799	2908.77	0.000
Residual Error	26	0.320	0.012		
Total	35	322.507			
R-Sq(adj) = 99.9 %					

Predictor	Coef.	SE Coef.	T	P
Constant	4.5188	0.6287	7.19	0.000
D	–0.9134	0.1049	–8.71	0.000
V	–0.005017	0.005471	–0.92	0.368
f	–7.3081	0.9862	–7.41	0.000
$D\times D$	0.054812	0.004622	11.86	0.000
$V\times V$	–0.00004644	0.00004358	–1.07	0.296
$f\times f$	–1.3917	0.9806	–1.42	0.168
$D\times V$	0.0004053	0.0003376	1.20	0.241
$D\times f$	1.73142	0.05064	34.19	0.000
$V\times f$	0.019729	0.004622	4.27	0.000

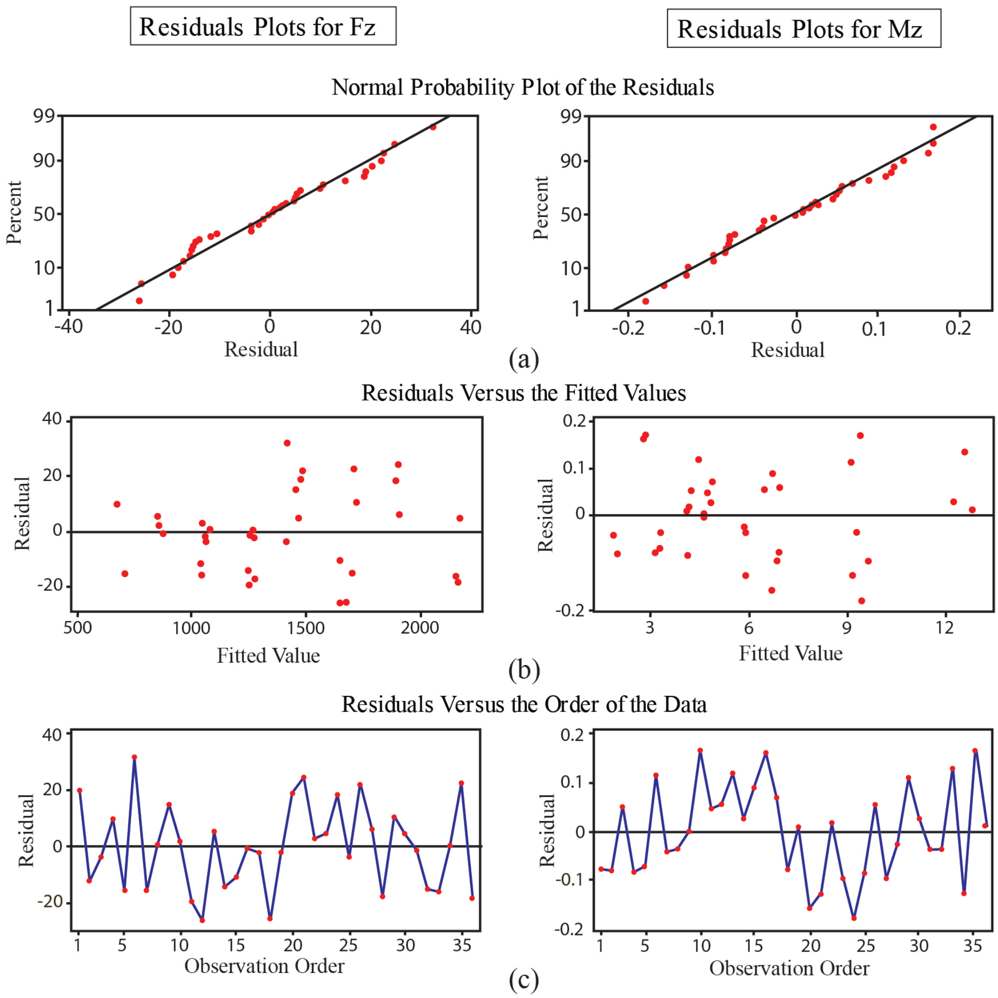

Fig. 4. *Residuals analyses for the Fz and Mz a) Normal Probability Plot of the Residuals, b) Residuals Versus the Fitted Values, c) Residuals Versus the Order of the Data*

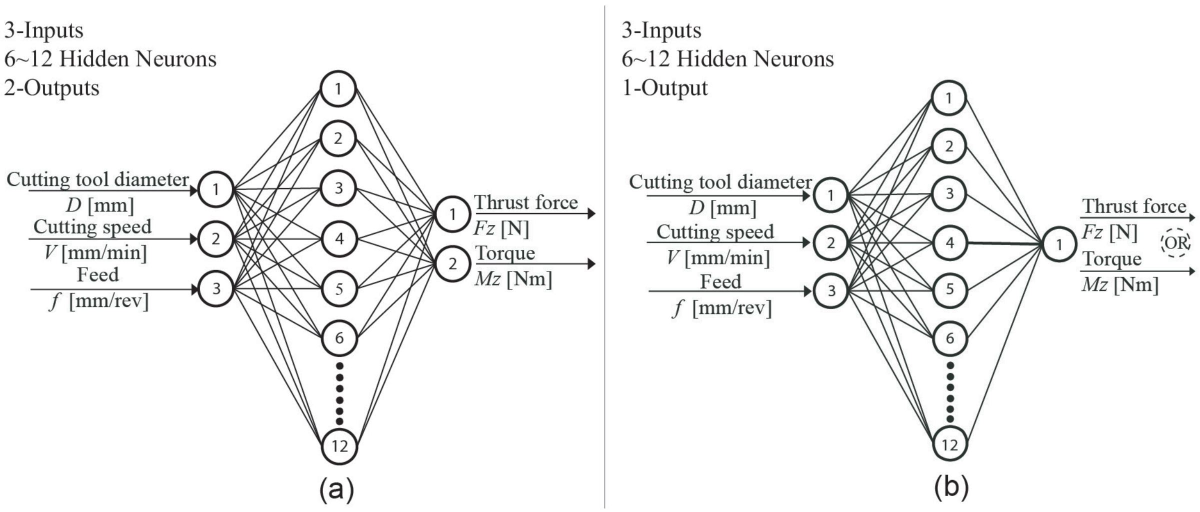

Fig. 5. *Architecture of ANN with a) 3 inputs-6 to 12 hidden neurons -2 outputs, and b) 3 inputs-6 to 12 hidden neurons-1 output topology*

2.3 ANN Modelling

Artificial Neural Network ability to learn complex non-linear and multivariable relationships between process parameters makes them very useful in many applications. An ANN consists of a number of neurons, which are divided into the three basic layers: input, hidden, and output. The neurons between the layers are linked, having synaptic weights. One of the basic advantages of ANN is its ability to learn from the process. When the architecture of the network is defined, then, through a learning process, weights are calculated to present the desired output.

The present research used a series of neural network pieces of software available for the development of a multilayer feedforward neural network. An elementary neuron with *R* inputs is shown in Figure 6a. Each input is weighted with an appropriate value (*w*). The sum of the weighted inputs and the bias forms the input to the transfer function (*f*). Neurons can use any differentiable transfer function (*f*) to generate their output.

The standard network that is used for function fitting is a two-layer feedforward network, with a tan-sigmoid transfer function in the hidden layer and a linear transfer function in the output layer (see Fig. 6b). Assuming that the activation function used in the hidden and the outer layer is sigmoidal, the outputs of the hidden and outer layer were calculated using the following equation:

$$f(net) = \frac{1}{1+e^{-net}}. \tag{4}$$

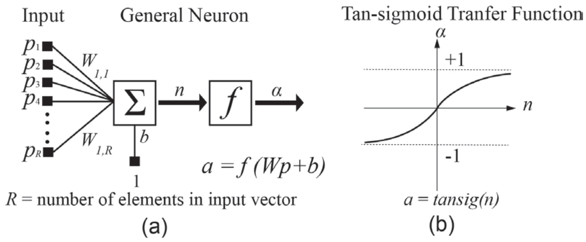

Fig. 6. *Multilayer neuron network architecture, a) elementary neuron with R inputs, b) linear transfer function*

All of the original (36) experimental data were randomly divided into three data sets including training, validation and testing. The back-propagation training algorithms, the scaled conjugate gradient (SCG) and Levenberg–Marquardt (LM), were used for ANNs training. The training set used 70 % of the data to build the network, 15 % to measure network generalization and 15 % as a testing set of the neural network. Three-layer network architectures were used to predict the thrust force and torque as shown in Fig. 5.

In the first case, a 3-(6~12)-2 ANN topology was used, which consists of three input nodes (tool

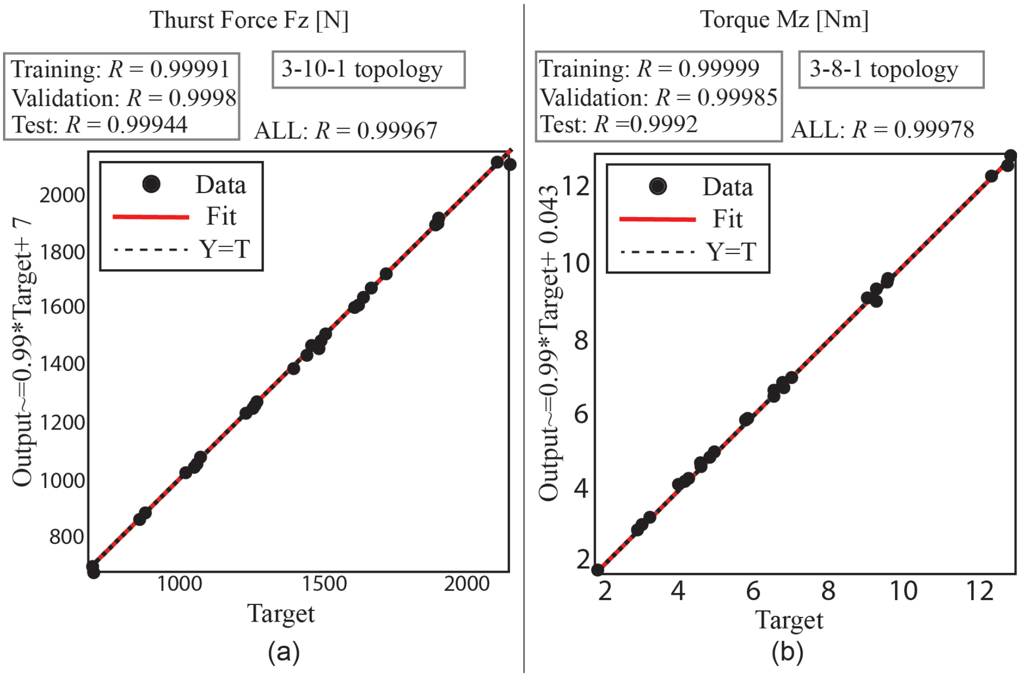

Fig. 7. *Neural network plot linear regressions for a) Fz and b) Mz*

diameter, cutting speed, feed rate), one hidden layer (6 to 12 neurons) and two outputs (thrust force and torque). In the second case, two different 3-(6~12)-1 ANN topologies were used as the output layer consists of one neuron corresponding to one output variable *Fz* and *Mz*, respectively.

In consequence of trials, the best network architecture for the prediction of thrust force was the 3-10-1 topology. The comparison of predicted results from ANN model with experimental measurements shows that there is a very good correlation between them. It is obvious that a neural network is an excellent tool for predicted values of *Fz* according to experimentally measured ones. The correlation coefficient (*R* value) between the outputs and targets is a measure of model accuracy. The *R* value for the entire dataset (training, validation and testing) is 0.99967, and it represents high correlation. In addition, all the categorized *R*-values (training, validation and test) are very close to 1 (see Fig. 7). When comparing both the measured and the predicted *Fz* values the highest discrepancy observed is 2.18%. In the case of *Mz*, the best network architecture for the prediction of the experimental values was the 3-8-1 topology. The *R* value for all the dataset (training, validation and testing) is 0.99978 and in each one of them separately is close to 1. As a result, the network achieves high accuracy (see Fig. 7). When comparing the measured with the predicted *Mz* values the highest difference observed is 3.15%. From the output of both cases, it

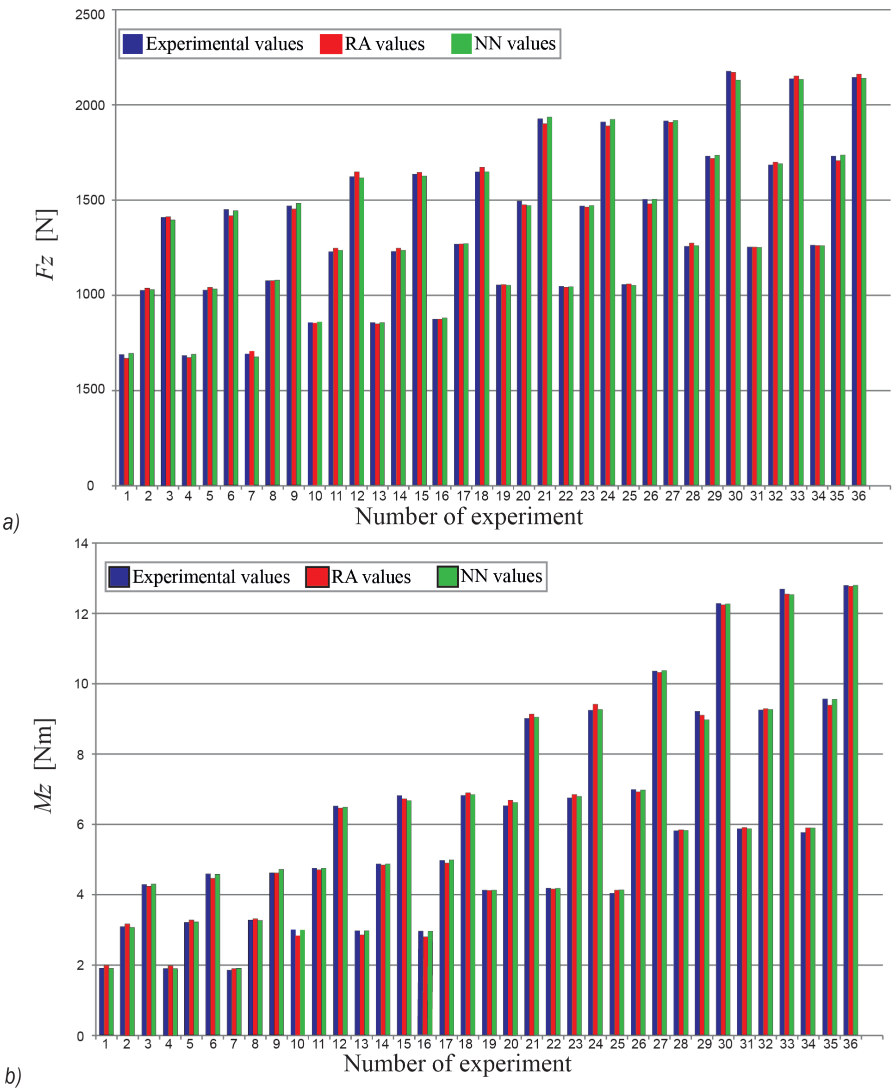

Fig. 8. *Comparison of the experimental values with the predicted values for a) Fz and b) Mz*

is concluded that the training of the ANN with one output for each case offers greater accuracy than in the case of the network with two outputs.

3 COMPARISON BETWEEN RSM AND ANN MODELS

A full factorial experimentation design is implemented to search for the effects of the cutting parameters (i.e. cutting speed, feed rate, and tool diameter) on the thrust force and torque in the case of drilling.

After each hole was made, the measurements of thrust force and torque were documented. Artificial neural network and response surface methodology models were developed to predict the thrust force and torque using the experimental data.

A comparison was established between the experimental values of *Fz* and *Mz* (see Fig. 8) and their values of ANN and RSM model, respectively. It is obvious that the predicted values from both models approximate the experimental values. Nevertheless, the predicted values from the ANN more accurately predict the experimental values than the regression analysis model. This can also be proved from the calculated percentage of error between experimental and predicted values of the models which are depicted in Fig. 9 for both the *Fz* and the *Mz*. In the case of

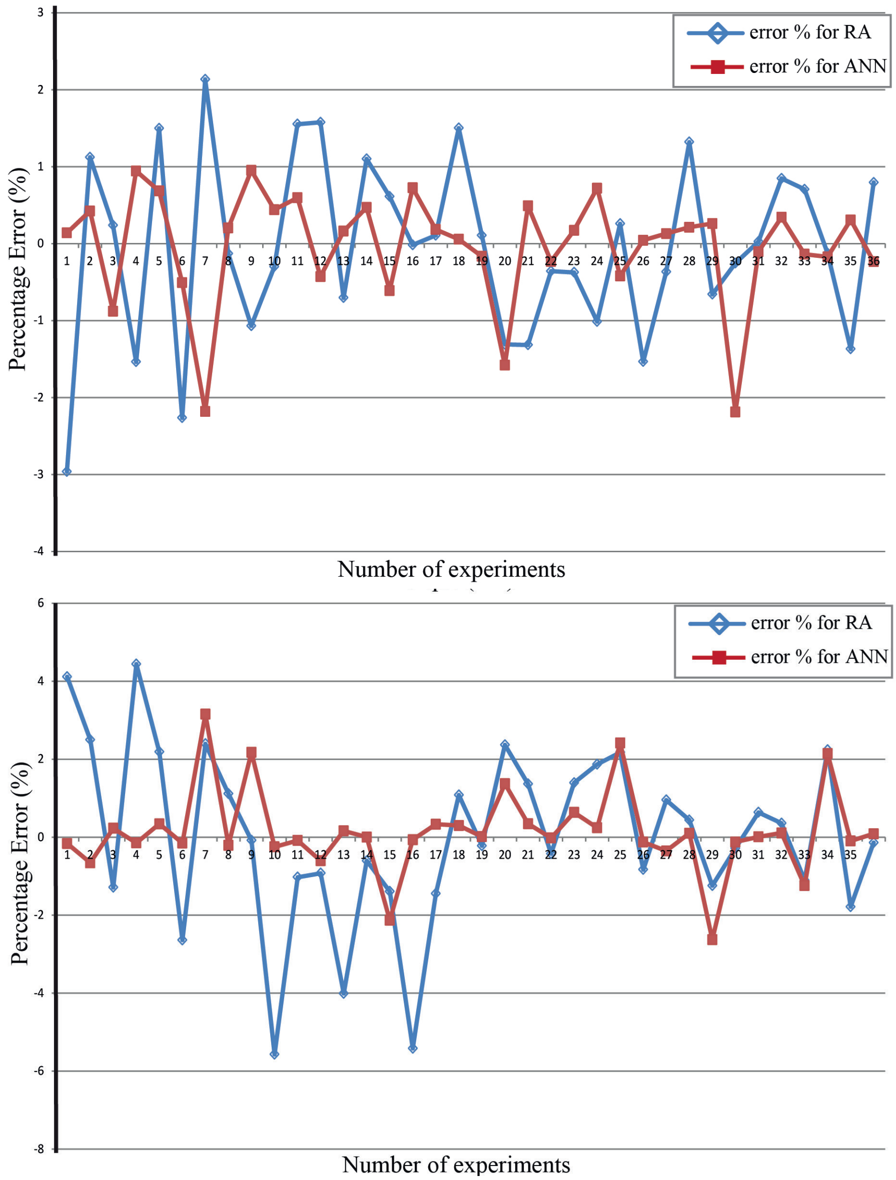

a)

b)

Fig. 9 *Error between experimental and predicted values for a) Fz and b) Mz* the ANN models, the accuracy achieved was 2.18 % and 3.15 % for both the thrust force and torque, while in the case of the response surface methodology model the accuracy achieved was 3 % and 5.6 %, respectively.

4 CONCLUSIONS

The optimization of a drilling process focused on cutting tools and parameters is a basic part of the entirely machining process, which influences sustainability. The aim of this study was the generation of mathematical models for the prediction of the thrust force (*Fz*) and torque (*Mz*) related to the cutting tools and other crucial cutting parameters as feed rate and cutting velocity during the drilling process. Two modelling techniques the RSM and ANN were used to predict the thrust force and torque in a series of drilling operations of Al7075. The developed models were considered to be very accurate for the prediction of the *Fz* and *Mz* within the range of the manufacturing parameters used. A number of different ANN architectures (3-(6~12)-2) and (3-(6~12)-1) have been tested to obtain the best neural network configuration in each case. Finally, the best architecture was the (3-10-1) for the case of the thrust force and the (3-8-1) for the case of torque. The outcomes proved that the accuracy achieved was 2.18 % and 3.15 % when using the ANN models for both the thrust force and torque measured, respectively. In the case of the RSM model, the accuracy achieved was 3 % and 5.6 %, respectively. As a result, both strategies are suitable for modelling and predicting thrust force and torque when drilling is concerned, but the application of ANN is slightly more accurate than the RSM one.

5 ACKNOWLEDGEMENTS

The authors would like to thank the Direction Team of the C3 CAD/CAM/CAE) Laboratory in the University of Applied Sciences of Western Macedonia, for its valuable help, making available human and technical resources.

6 REFERENCES

[1] Ucun, I. (2016). 3D finite element modelling of drilling process of Al7075-T6 alloy and experimental validation. *Journal of Mechanical Science and Technology*, vol. 30, no. 4, p. 1843-1850, **DOI:10.1007/s12206-016-0341-0**.

[2] Suryaa, V.R., Kumara, K.M.V., Keshavamurthya, R., Ugrasenb G., Ravindrac H.V. (2017). Prediction of machining Characteristics using artificial neural network in wire EDM of Al7075 based in-situ composite. 5*th International Conference of Materials Processing and Characterization (ICMPC) Proceedings*, p. 203-212, **DOI:10.1016/j.matpr.2017.01.014**.

[3] Karabulut, S., Karakoc, H. (2017) Investigation of surface roughness in the milling of Al7075 and open-cell SiC foam composite and optimization of machining parameters. *Neural Computing & Applications*, vol 28, p. 313-327, **DOI:10.1007/s00521-015-2058-x**.

[4] Osman, A., Mohd, N., Suziah, S., Wan F. (2009). Study of genetic algorithm to fully-automate the design and training of artificial neural network. *International Journal of Computer Science and Network Security*, vol. 9, no. 1, p. 217-226.

[5] Leite, W.O., Campos Rubio, J.C., Duduch J.G., Maciel de Almeida P.E. (2015). Correcting geometric deviations of CNC Machine-Tools: An approach with Artificial Neural Networks. *Applied Soft Computing*, vol. 36, p. 114–124, **DOI:10.1016/j.asoc.2015.07.014**.

[6] Patra, K., Jha, A.K., Szalay, T., Ranjan J., Monostori L. (2017). Artificial neural network based tool condition monitoring in micromechanical peck drilling using thrust force signals. *Precision Engineering*, vol. 48, p. 279-291, **DOI:10.1016/j.precisioneng.2016.12.011**.

[7] Qin, X., Wang, B., Wang, B., Li, H., Jiang, Y., Zhang, X. (2014). Delamination analysis of the helical milling of carbon fiber-reinforced plastics by using the artificial neural network model. *Journal of Mechanical Science and Technology*, vol. 28, no. 2, p. 713-719, **DOI:10.1007/s12206-013-1135-2**.

[8] Cornea, R., Natha, C., Mansorib, M., Kurfessa, T. (2016). Enhancing spindle power data application with neural network for real-time tool wear/breakage prediction during inconel drilling. *Procedia Manufacturing*, vol. 5. no. 1–14, **DOI:10.1016/j.promfg.2016.08.004**.

[9] Çiçek, A., Kıvak, T., Samtaş, G. (2012). Application of Taguchi method for surface roughness and roundness error in drilling of AISI 316 stainless steel. *Strojniški vestnik -Journal of Mechanical Engineering*, vol. 58, no. 3, p. 165-174, **DOI:10.5545/sv-jme.2011.167**.

[10] Rao, S., Sethi, A., Das, A.K., Mandal, N., Kiran, P., Ghosh, R., Dixit, A.R., Mandal, A. (2017). Fiber laser cutting of CFRP composites and process optimization through response surface methodology. *Materials and Manufacturing Processes*, vol. 32, no. 14,p. 1612-1621, **DOI:10.1080/10426914.2017.1279296**.

[11] Thakre, A.A., Soni, S. (2016). Modeling of burr size in drilling of aluminum silicon carbide composites using response surface methodology. *Engineering Science and Technology, an International Journal*, vol. 19, no. 3, p. 1199–1205, **DOI:10.1016/j.jestch.2016.02.007**.

[12] Boyacı, A.İ, Hatipoğlu, T., Balcı, E. (2017). Drilling process optimization by using fuzzy-based multi-response surface methodology. *Advances in Production Engineering & Management*, vol. 2, no. 2. p. 163-172, **DOI:10.14743/apem2017.2.248**.

[13] Nouioua, M., Yallese, M.A., Khettabi, R., Belhadi, S., Bouhalais, M. L., Girardin, F. (2017). Investigation of the performance of the MQL, dry, and wet turning by response surface methodology (RSM) and artificial neural network (ANN),

International Journal of Advanced Manufacturing Technology, vol. 93, p. 2485-2504, **DOI:10.1007/s00170-017-0589-2**.

[14] Kumar. R., Chauhan. S. (2015). Study on surface roughness measurement for turning of Al 7075/10/SiCp and Al 7075 hybrid composites by using response surface methodology (RSM) and artificial neural networking (ANN). *Measurement*, vol. 65, p. 166-180, **DOI:10.1016/j.measurement.2015.01.003**.

[15] Gupta, A.K. (2010). Predictive modelling of turning operations using response surface methodology, artificial neural networks and support vector regression. *International Journal of Product Research*, vol. 48, no. 3, p. 763-778, **DOI:10.1080/00207540802452132**.

[16] Asiltórk, I., Hunkas, M. (2011). Modeling and prediction of surface roughness in turning operations using artificial neural network and multiple regression method. *Expert Systems with Applications*, vol. 38, no. 5, p. 5826–5832, **DOI:10.1016/j.eswa.2010.11.041**.

[17] Karnik, S.R., Gaitonde, V.N., Davim, J.P.A. (2008). Comparative study of the ANN and RSM modeling approaches for predicting burr size in drilling. *International Journal of Advanced Manufturing Technology*, vol. 38, p. 868-883, **DOI:10.1007/s00170-007-1140-7**.

[18] Çiçek, A., Kıvak, T., Samtaş, G., Çay, Y. (2012). Modelling of thrust forces in drilling of AISI 316 stainless steel using artificial neural network and multiple regression analysis. *Strojniški vestnik - Journal of Mechanical Engineering*, vol. 58, no. 7-8, p. 492-498, **DOI:10.5545/sv-jme.2011.297**.

[19] Mayyas, A., Qasaimeh, A., Alzoubi, K., Lu, S., Hayajneh, M., Hassan, A. (2012). Modeling the drilling process of aluminum composites using multiple regression analysis and artificial neural networks. *Journal of Minerals and Materials Characterization and Engineering*, volo 11, no. 10, p. 1039-1049, **DOI:10.4236/jmmce.2012.1110108**.

[20] Bajić, D., Celent, L., Jozić, S., Bajić, D., Celent, L., Jozić, S. (2012). Modeling of the influence of cutting parameters on the surface roughness, tool wear and cutting force in face milling in off-line process control. *Strojniški vestnik - Journal of Mechanical Engineering*, vol. 58, no. 11, p. 673-682, **DOI:10.5545/sv-jme.2012.456**.

[21] Alharthi, N.H., Bingol, S., Abbas, A.T., Ragab, A.E., El-Danaf, E.A., Alharbi, H.F. (2017). Optimizing cutting conditions and prediction of surface roughness in face milling of AZ61 using regression analysis and artificial neural network, *Advances in Materials Science and Engineering,* vol. 2017, art. ID 7560468, **DOI:10.1155/2017/7560468**.

[22] Rooki, R., Ardejani, D.F., Moradzadeh, A. (2014). Hole cleaning prediction in foam drilling using artificial neural network and multiple linear regression. *Geomaterials*, vol. 4, no. 1, p. 47-53, **DOI:10.4236/gm.2014.41005**.

[23] Kahraman, S. (2016). Estimating the penetration rate in diamond drilling in laboratory works using the regression and artificial neural network analysis. *Neural Processing Letters*, vol. 43, no. 2, p. 523–535, **DOI:10.1007/s11063-015-9424-7**.

[24] Chavoshi, S.Z. (2011). Analysis and predictive modeling of performance parameters in electrochemical drilling process. *International Journal of Advanced Manufacturing Technologies*, vol. 53, no. 9-12, p. 1081–1101, **DOI:10.1007/s00170-010-2897-7**.

Strojniški vestnik - Journal of Mechanical Engineering 64(2018)6, 362-372

DOI:10.5545/sv-jme.2017.5110
Original Scientific Paper
Received for review: 2017-11-25
Received revised form: 2018-03-10
Accepted for publication: 2018-03-28

Design Methodology for Coplanar Axes Line Gear with Controllable Sliding Rate

Yangzhi Chen – Zheng Li – Xiongdun Xie – Yueling Lyu*
South China University of Technology, China

Line gear (LG) pair is a novel gear mechanism via point contact meshing on the basis of space curve meshing theory. In this paper, aiming to control the sliding rate, related to the shape of the contact curves of LGs, the driving contact curve of a coplanar axes LG pair was extended from a circular helix to a conic helix with variable cone angle, and the driven contact curve was subsequently obtained based on the space curve meshing theory. A new type of line tooth, of which two contact curves lie on each side, was proposed for forward-reverse transmission without backlash. The tooth surface is formed by a normal tooth profile moving along the contact curve and the tooth thickness auxiliary curve. The formulae of the contact curves, tooth thickness auxiliary curves, and spatial cylindrical tooth surfaces of the new type of line tooth are derived, which theoretically provides a foundation for the standardized production of LG pairs in industry. The calculation examples of the LG pairs show that the sliding rate can be reduced by using a conic helix as the driving contact curve. The results of the kinematics experiment show that the LG pair designed by the methodology could be capable of achieving forward-reverse transmission without backlash and with a controllable sliding rate.

Keywords: line gear, sliding rate, contact curve, tooth surface, non-backlash, forward-reverse transmission

Highlights

- *Design methodology for coplanar axes line gear with controllable sliding rate is deduced.*
- *The mechanism can transmit rotation at an arbitrary alternate angle within 0° to 180°.*
- *A conic helix with variable cone angle was chosen as the driving contact curve.*
- *A new type of line tooth, of which two contact curves lie on each side, was proposed for forward-reverse transmission without backlash.*
- *An example is illustrated in detail and simulated in the Pro/E software.*
- *An experiment was carried out to verified the LG pair designed by the methodology could be capable of achieving forward-reverse transmission without backlash and with controllable sliding rate.*

0 INTRODUCTION

In 1733, Camus' Theorem [1] was proposed for the conjugation of tooth profiles. In 1956, Beam [2] first proposed the so-called 'Beveloid gears', which can be adopted for power transmission between nearly-parallel shafts and allow for adjustment of the gearing backlash, following which many studies detailed their geometry, design and manufacturing [3] to [5]. In 1962, Baxter [6] analysed the basic geometric and tooth contact of hypoid gears. In the 1980s, Litvin et al. [7] systematically proposed the gear geometry theory. In recent decades, the design and manufacturing of gear pairs transmitting rotations between intersecting shafts have been a topic of research [8] to [10].

The line gear (LG) pair, also called a 'space curve meshing wheel' (SCMW) in studies before 2014, proposed by Chen [11], is a novel transmission mechanism via point contact meshing on the basis of space curve meshing theory. According to the basic theory of LG, the motion at the meshing point should satisfy the following equation [12]:

$$\boldsymbol{v}_{12} \times \boldsymbol{\beta} = \boldsymbol{0}, \tag{1}$$

where, $\boldsymbol{v}_{12}$ is the relative velocity at the meshing point between the driving contact curve and the driven contact curve, and $\boldsymbol{\beta}$ is the unit principal normal vector of the driving contact curve at the meshing point.

Compared with traditional gear, LG has characteristics of compact space, large transmission ratio and flexible design theory [11]. There is no undercut phenomenon on the line gear, and the minimum number of the line teeth of an line gear equals 1. It could be flexible to design for the application of the LGs to transmissions with perpendicular shafts [13], intersecting shafts [14] or skew shafts [15]. The driving contact curve of the coplanar axes of the LG pair is a circular helix, satisfying the condition of contact ratio [16], and a conjugated driven contact curve can be obtained through the coordinate system transformation based on space curve meshing equation Eq. (1), which may be a circular helix, a conic helix or a planar Archimedean spiral. An LG pair consists of a driving LG and a driven LG. The driving line teeth and the driven line teeth are uniformly distributed around the basal wheels of the driving LG and the driven LG, respectively [15]. There are mainly two forms of the line-tooth of LG, one of which is cantilever structural

*Corr. Author's Address: School of Mechanical and Automotive Engineering, South China University of Technology, Guangzhou, China, lvyl88@scut.edu.cn

form with a circular profile, and the other is that its line tooth is constructed by a convex or a concave arc profile radially attached to the wheel body. The cantilever structural tooth is the simplest structure in previously published papers. The line tooth radially attached to the wheel body is suitable for the manufacturing process of cutting materials such as CNC machining, and be of better bearing capacity [17] and [18].

The sliding rate of a gear pair, used for describing the relative movement trend of each gear at the meshing point, is a critical impacting factor on the transmission quality [19]. The relative sliding between two tooth surfaces might bring about negative influences such as surface wear and frictional loss, so the allowable value of the sliding rate depends on different working conditions such as load, speed, lubrication condition and so on [20] and [21]. If a good elasto-hydrodynamic-lubrication (EHL) oil film is formed at a certain relative sliding speed, the surface wear will be eliminated and transmission efficiency will be increased [22] and [23], at which circumstance the main failure form of gears is tooth surface fatigue pitting. Therefore, for the gear transmission, the research result on sliding rate is the basis of gear lubrication and failure analysis.

The sliding rate of the LG pair depends on the relative position parameters and the meshing radius of the LG pair. Aiming to decrease the sliding rate and reduce the gear wear, the design process usually follows the position parameter selection criterion in which the sliding rate equals zero at the midpoint of the contact curves [24].

In this paper, with the aim of modifying the sliding rate of the LG pair, a conic helix with variable cone angle was chosen as the driving contact curve. Then, the equation forms of the driving contact curve and the driven contact curve in the respective follow-up coordinate systems were unified. A new type of the line-tooth of LG was subsequently designed, which could be capable of achieving forward-reverse transmission without backlash. There are two contact curves that lie on each side of one line tooth. Two normal convex arc tooth profiles are established in the normal sections of two contact curves at any meshing point to form a line tooth entity.

1 DESIGN METHODS

1.1 Design Formulae of a Pair of Coplanar Axes LGs

The axes of the driving LG and the driven LG are in the same plane, covering the parallel axes and arbitrary angle intersecting axes. The coordinate systems are established, as shown in Fig. 1. The coordinate systems $o_0{-}x_0y_0z_0$ and $o_1{-}x_1y_1z_1$ are the fixed coordinate system and the follow-up coordinate system of a driving LG, respectively. The coordinate systems $o_p{-}x_py_pz_p$ and $o_2{-}x_2y_2z_2$ are the fixed coordinate system and the follow-up coordinate system of a driven LG, respectively. The driving LG rotates around $z_0(z_1)$-axis and the driven LG rotates around $z_2(z_p)$-axis. The shaft angle between $z_0(z_1)$-axis and $z_2(z_p)$-axis is denoted as θ_0, $\theta_0 \in [0,\pi)$. With the aim of avoiding overlap between two shafts of LG pair, define $o_0o_p{=}a$.

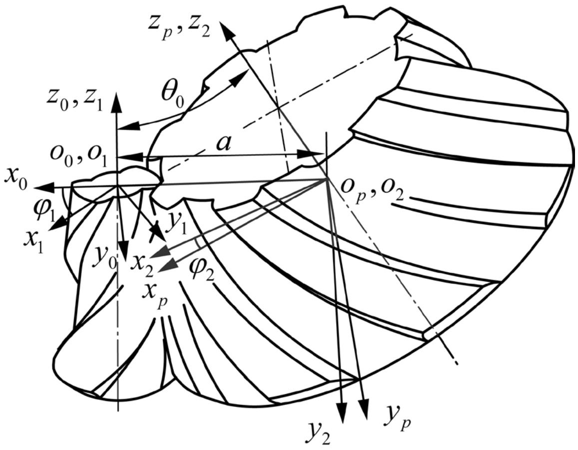

Fig. 1. *The coordinate systems of a pair of coplanar axes LGs*

The transformation matrixes for the coordinate systems in the design process of the coplanar axes LG are as Eqs. (2) to (4).

$$\boldsymbol{M}_{p0}=\begin{bmatrix}\cos\theta_0 & 0 & -\sin\theta_0 & a\cos\theta_0\\ 0 & 1 & 0 & 0\\ \sin\theta_0 & 0 & \cos\theta_0 & a\sin\theta_0\\ 0 & 0 & 0 & 1\end{bmatrix}, \tag{2}$$

$$\boldsymbol{M}_{01}=\begin{bmatrix}\cos t & -\sin t & 0 & 0\\ \sin t & \cos t & 0 & 0\\ 0 & 0 & 1 & 0\\ 0 & 0 & 0 & 1\end{bmatrix}, \tag{3}$$

$$\boldsymbol{M}_{2p}=\begin{bmatrix}\cos\frac{t}{i} & -\sin\frac{t}{i} & 0 & 0\\ \sin\frac{t}{i} & \cos\frac{t}{i} & 0 & 0\\ 0 & 0 & 1 & 0\\ 0 & 0 & 0 & 1\end{bmatrix}, \tag{4}$$

where, t is an independent parameter of the contact curves and i is the transmission ratio.

The equation of a driving contact curve in $o_1-x_1y_1z_1$ is given as Eq. (5).

$$\boldsymbol{R}_1^1=\begin{cases}x_1=-(m_1+n_1t\sin\theta_1)\cos t\\ y_1=(m_1+n_1t\sin\theta_1)\sin t\\ z_1=-n_1t\cos\theta_1\end{cases}, \qquad (5)$$

where, θ_1 is half cone angle, m_1 and n_1 are conical parameters. When θ_1 equals to 0, the driving contact curve is a circular helix. Under the following conditions for the value of the parameter θ_1, $\theta_1 \in (0,\theta_0]$ and $\theta_1 \neq 90°$, the driving contact curve is a common conic helix. When θ_1 equals to 90°, the driving contact curve is a planar Archimedean spiral.

From Eqs. (2) to (5), the equation of a driven contact curve in $o_2-x_2y_2z_2$, conjugated with the given driving contact curve above, is reflected as follows.

$$\boldsymbol{R}_2^2=\boldsymbol{M}_{2p}\cdot\boldsymbol{M}_{p0}\cdot\boldsymbol{M}_{01}\cdot\boldsymbol{R}_1^1$$
$$=\begin{cases}x_2=\left[\left(a-m_1\right)\cos\theta_0+n_1t\sin\left(\theta_0-\theta_1\right)\right]\cos\dfrac{t}{i}\\ y_2=\left[\left(a-m_1\right)\cos\theta_0+n_1t\sin\left(\theta_0-\theta_1\right)\right]\sin\dfrac{t}{i}\\ z_2=-n_1t\cos\left(\theta_0-\theta_1\right)+\left(a-m_1\right)\sin\theta_0\end{cases}. \qquad (6)$$

Similar to the driving contact curve, the driven contact curve may be a circular helix, a conic helix or a planar Archimedean spiral.

Eqs. (5) and (6) with different parameters θ_0 and θ_1 can generally be used to describe a circular helix, a conic helix and a planar Archimedean spiral. Therefore, in geometry, an undifferentiated form of mathematical expressions of the contact curves of an LG pair exists, which can generally be used in the research of the line-tooth entity construction and machining method of the driving LG and the driven LG.

Referring to $\boldsymbol{R}_1^1$, aiming to eliminate the constant $(a-m_1)\sin\theta_0$ in $\boldsymbol{R}_2^2$, the equation of the driven contact curve in a new follow-up coordinate system $o_{2'}-x_{2'}y_{2'}z_{2'}$, which is formed by moving the coordinate system $o_2-x_2y_2z_2$ along z_2-axis by the distance $(a-m_1)\sin\theta_0$, is expressed as Eq. (7).

$$\boldsymbol{R}_2^{2'}=\begin{cases}x_2=\left[\left(a-m_1\right)\cos\theta_0+n_1t\sin\left(\theta_0-\theta_1\right)\right]\cos\dfrac{t}{i}\\ y_2=\left[\left(a-m_1\right)\cos\theta_0+n_1t\sin\left(\theta_0-\theta_1\right)\right]\sin\dfrac{t}{i}\\ z_2=-n_1t\cos\left(\theta_0-\theta_1\right)\end{cases}. \qquad (7)$$

The transformation matrix between two coordinate systems, from $o_{2'}-x_{2'}y_{2'}z_{2'}$ to $o_2-x_2y_2z_2$, is as Eq. (8), which is formed by moving the coordinate system:

$$\boldsymbol{M}_{22'}=\begin{bmatrix}1&0&0&0\\0&1&0&0\\0&0&1&\left(a-m_1\right)\sin\theta_0\\0&0&0&1\end{bmatrix}. \qquad (8)$$

After unifying the coordinate systems $o_1-x_1y_1z_1$ and $o_{2'}-x_{2'}y_{2'}z_{2'}$ into the coordinate system $o_m-x_my_mz_m$, which can generally be used to describe the driving contact curve and the driven contact curve, from Eqs. (5) and (7), the undifferentiated form of the contact curves of an LG pair can be written as Eq. (9).

$$\boldsymbol{R}_{j1'}^m=\begin{cases}x_j=k_j\left(m_j+n_jt_j\sin\theta_j\right)\cos t_j\\ y_j=\left(m_j+n_jt_j\sin\theta_j\right)\sin t_j\\ z_j=-n_jt_j\cos\theta_j\\ \left(j=1,2\right)\end{cases}, \qquad (9)$$

where, $\boldsymbol{R}_{11}^m$ represents a driving contact curve and $\boldsymbol{R}_{21}^m$ represents a driven contact curve. t_j are independent parameters, $t_j \in [t_{js}, t_{je}]$. t_{js} and t_{je} are starting values and ending values for meshing points, respectively. θ_j are half cone angles, m_j and n_j are conical parameters. k_j represents a parameter of the hand of the spiral. When k_j equals 1, the conic helix is left-handed, and when k_j equals –1, it is right-handed.

The equations of a driving contact curve and a driven contact curve are uniquely determined by the parameters θ_j, m_j, n_j, k_j. The parameters of a driving contact curve, a driven contact curve and the relative position parameters should meet the following mathematical conditions:

$$\begin{cases}\dfrac{t_1}{t_2}=\dfrac{n_2}{n_1}=i\\ m_1+m_2\sec\theta_0=a\\ \theta_1+\theta_2=\theta_0\\ -k_1=k_2=1\end{cases}. \qquad (10)$$

A driving contact curve and a driven contact curve of an LG pair are uniquely determined by parameters required, including relative position parameters a and θ_0, transmission ratio i, conical parameters m_1 and n_1, half cone angle θ_1, starting value t_{1s} and ending value t_{1e} for meshing point of a driving contact curve.

The values of parameters t_{1s} and t_{1e} should satisfy the condition of contact ratio **[16]**. For a special condition of that θ_0 equals to 90°, the value of the parameter m_2 can be selected on request.

1.2 Construction of Line Tooth

The motion transmission for an LG pair exists via two contact curves on the driving LG and the driven LG, respectively, which are expressed as Eq. (9). The contact curves lie on the line teeth entity with a spatial cylindrical surface [18]. The driving line teeth and the driven line teeth are uniformly distributed around the cylindrical or conical wheel bodies of the driving LG and the driven LG.

Aiming to realize the non-backlash forward-reverse transmission, the number of contact curves on each line tooth equals two, including the first contact curve $\boldsymbol{R}_{j1}^{m}$ and the second contact curve $\boldsymbol{R}_{j2}^{m}$. That is, the driving contact curves in one line tooth of the driving LG include the first contact curve of the driving LG $\boldsymbol{R}_{11}^{m}$ and the second contact curve of the driving LG $\boldsymbol{R}_{12}^{m}$, and the driven contact curves in one line tooth of the driven LG include the first contact curve of the driven LG $\boldsymbol{R}_{21}^{m}$ and the second contact curve of the driven LG $\boldsymbol{R}_{22}^{m}$. When the driving LG rotates forward, $\boldsymbol{R}_{11}^{m}$ it engages with $\boldsymbol{R}_{21}^{m}$. And when it rotates in reverse, $\boldsymbol{R}_{12}^{m}$ it engages with $\boldsymbol{R}_{22}^{m}$.

$\boldsymbol{R}_{11}^{m}$ and $\boldsymbol{R}_{21}^{m}$ are expressed as Eq. (9). $\boldsymbol{R}_{12}^{m}$ is obtained by rotating $\boldsymbol{R}_{11}^{m}$ an angle of φ_{1FR} around the axis of the driving LG clockwise, and $\boldsymbol{R}_{22}^{m}$ is obtained by rotating $\boldsymbol{R}_{21}^{m}$ an angle of φ_{2FR} around the axis of the driven LG counter-clockwise. Because the line teeth are uniformly distributed in the circumferential direction of the wheel body, $\boldsymbol{R}_{j1ne}^{m}$, the first contact curve that lies on the next line tooth adjacent to the second contact curve $\boldsymbol{R}_{j2}^{m}$, can be obtained by rotating $\boldsymbol{R}_{j1}^{m}$ an angle of $2\pi/N_j$ around the axis of the LG, where N_1 is tooth number of the driving LG, and N_2 is tooth number of the driven LG, as shown in Fig. 2.

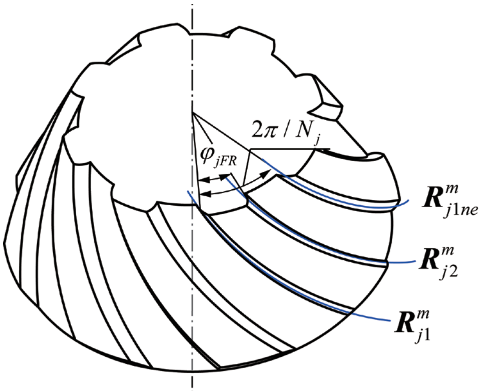

Fig. 2. *The schematic diagram of contact curves*

The transformation matrixes for coordinate systems involved are as Eqs. (11) and (12).

$$\boldsymbol{M}_{j2,j1}^{m} = \begin{bmatrix} \cos\varphi_{jFR} & -k_j \sin\varphi_{jFR} & 0 & 0 \\ k_j \sin\varphi_{jFR} & \cos\varphi_{jFR} & 0 & 0 \\ 0 & 0 & 1 & 0 \\ 0 & 0 & 0 & 1 \end{bmatrix}, \quad (11)$$

$$\boldsymbol{M}_{j1ne,j1}^{m} = \begin{bmatrix} \cos\frac{2\pi}{N_j} & -k_j \sin\frac{2\pi}{N_j} & 0 & 0 \\ k_j \sin\frac{2\pi}{N_j} & \cos\frac{2\pi}{N_j} & 0 & 0 \\ 0 & 0 & 1 & 0 \\ 0 & 0 & 0 & 1 \end{bmatrix}. \quad (12)$$

The values of the parameters φ_{1FR} and φ_{2FR} determine the relative positions of the first contact curve and the second contact curve of the LGs. The second contact curves of the driving LG and the driven LG are also a couple of conjugated curves satisfying the meshing condition, which is expressed as Eq. (13).

$$\boldsymbol{M}_{22'} \cdot \boldsymbol{R}_{22}^{m} = \boldsymbol{M}_{2p} \cdot \boldsymbol{M}_{p0} \cdot \boldsymbol{M}_{01} \cdot \boldsymbol{R}_{12}^{m}. \quad (13)$$

Furthermore, the values of the parameters φ_{1FR} and φ_{2FR} determine the tooth thickness and the space width, which can be defined in the transverse plane, normal plane. and axial section. According to the meshing theory of LG, while the driving LG rotates forward or reverses at the same position, the two meshing points located respectively at the first contact curve or the contact curve of a line tooth lie on the same axial section of the LG. Therefore, the line-tooth thickness and the space width of LG are defined in the axial section, i.e., the line-tooth thickness and the space width are along the direction of a straight generatrix of a suppositional conical surface, a cylindrical surface or a plane, where the contact curves lie on. The line tooth thickness and the space width are two constant values, and they are independent of the position of the meshing point. The line tooth thickness s_j of LG is defined as the distance between two intersection points, one of which is the intersection point of $\boldsymbol{R}_{j1}^{m}$ and any one axial section, the other is the intersection point of $\boldsymbol{R}_{j2}^{m}$ and the axial section mentioned above. The space width e_j is defined as the distance between two intersection points, one of which is the intersection point of $\boldsymbol{R}_{j2}^{m}$ and any one axial section, the other is the intersection point of $\boldsymbol{R}_{j1ne}^{m}$ and the axial section mentioned above, as shown in Fig.3.

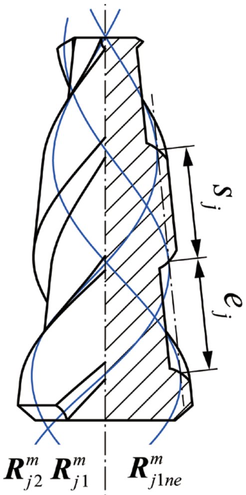

Fig. 3. *The schematic diagram of line tooth thickness and the space width in axial section*

From Eqs. (8), (11) and (12), the parameters s_j and e_j are derived.

$$s_j = n_j \varphi_{jFR}, \quad e_j = n_j (2\pi / N_j - \varphi_{jFR}). \tag{14}$$

An LG pair with non-backlash forward-reverse transmission should satisfy the correct meshing condition, that is, the line-tooth thickness of the driving LG is equal to the space width of the driven LG, and the space width of the driving LG is equal to the line-tooth thickness of the driven LG. The correct meshing condition of an LG pair is as Eq. 15.

$$\begin{cases} s_1 = e_2 \\ s_2 = e_1 \end{cases}. \tag{15}$$

From Eqs. (8), (11) to (15), the second contact curves of the driving LG and the driven LG meeting the correct meshing condition were obtained

$$\boldsymbol{R}_{j2}^{m} = \begin{cases} x_j = k_j m_j' \cos\left(t_j + \dfrac{\pi}{N_j}\right) \\ y_j = m_j' \sin\left(t_j + \dfrac{\pi}{N_j}\right) \\ z_j = -n_j t_j \cos\theta_j \end{cases}, \quad (j = 1, 2), \tag{16}$$

where $m_j' = m_j + n_j t_j \sin\theta_j$.

A line tooth in this paper is composed of three surfaces, including Σ_{j1}^{m}, Σ_{j2}^{m} and Σ_{j3}^{m}. Σ_{j1}^{m} and Σ_{j2}^{m} are two parts of spatial cylindrical surfaces located at each side of the line-tooth. The contact curves $\boldsymbol{R}_{j1}^{m}$ and $\boldsymbol{R}_{j2}^{m}$ lie on Σ_{j1}^{m} and Σ_{j2}^{m}, respectively. The normal tooth profile is located in the normal section of the contact curve at any meshing point. The normal tooth profile is a section of invariant arc with the radius of r, which intersects with the contact curve. While the normal tooth profile moves along the contact curve, which takes a role of a generatrix, the continuous spatial cylindrical tooth surfaces are formed, i.e. the spatial cylindrical tooth surfaces Σ_{j1}^{m} is formed by a section of arc moving along the $\boldsymbol{R}_{j1}^{m}$, which takes a role of a generatrix, and the Σ_{j2}^{m} is formed by a section of arc moving along the $\boldsymbol{R}_{j2}^{m}$ in the same principal. Σ_{j3}^{m} is the upper surface. If θ_j equals to 0, Σ_{j3}^{m} is a cylindrical surface. If θ_j equals to 90°, Σ_{j3}^{m} is a plane. Under following conditions for the value of the parameter θ_1, $\theta_1 \in (0, \theta_0]$, Σ_{j3}^{m} is a conical surface.

Because the contact curves are spatial curves, for the definition of the positions of Σ_{j1}^{m} and Σ_{j2}^{m}, which must satisfy the conditions of none meshing interference [18], the second constraint should be requested. Therefore, the tooth thickness auxiliary curves are defined as the trajectories of arc centres of normal tooth profiles. There are two functions of the tooth thickness auxiliary curves, one of which is to limit the tooth profile constantly perpendicular to a tangent vector of the contact curve, and the other is to keep the arc radius r. The tooth thickness auxiliary curves comprise the first tooth thickness auxiliary curve $\boldsymbol{R}_{j1c}^{m}$ and the second tooth thickness auxiliary curve $\boldsymbol{R}_{j2c}^{m}$, lying between the first contact curve and the second contact curve, and the first (or second) tooth thickness auxiliary curve is shifted $\overrightarrow{\boldsymbol{MM}_1}$ (or $\overrightarrow{\boldsymbol{MM}_2}$) from every point on the first (or second) contact curve, as shown in Fig. 4. The spatial cylindrical tooth surfaces Σ_{j1}^{m} and Σ_{j2}^{m} are formed by the two sections of normal tooth profiles moving along the corresponding contact curves and the tooth thickness auxiliary curves respectively.

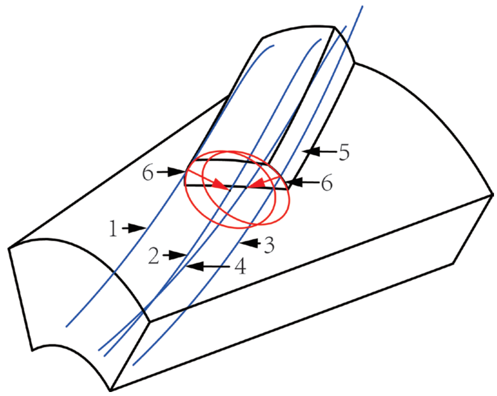

Fig. 4. *The schematic diagram of the construction of the line-tooth*

The directions of $\overrightarrow{\boldsymbol{MM}_1}$ and $\overrightarrow{\boldsymbol{MM}_2}$ are defined to be perpendicular to the tangent vector of the corresponding contact curves, respectively, so that the tooth thickness auxiliary curves can limit the normal tooth profile constantly perpendicular to the tangent vector of the contact curve.

The coordinate system $o_q-x_q y_q z_q$, a fixed coordinate system, is an auxiliary coordinate system that concisely describes the coordinates of any meshing point. The z_q-axis is coincident with the meshing line, the trajectory of a meshing point in the fixed coordinate system, and the x_q-axis and the shaft of LG intersect at a right angle. The transformation matrix from the coordinate system $o_q-x_q y_q z_q$ to the coordinate system $o_m-x_m y_m z_m$ is as Eq. (17).

$$\boldsymbol{M}_{mq}=\begin{bmatrix} -k_j\cos\theta_j\cos t_j & -k_j\sin\theta_j & -k_j\sin\theta_j\cos t_j & k_j m_j\cos t_i \\ -\cos\theta_j\sin t_j & \cos t_j & -\sin\theta_j\sin t_j & m_j\sin t \\ -\sin\theta_j & 0 & \cos\theta_j & 0 \\ 0 & 0 & 0 & 1 \end{bmatrix}. \tag{17}$$

In the coordinate system $o_q-x_q y_q z_q$, $\overrightarrow{\boldsymbol{MM}_1}$ and $\overrightarrow{\boldsymbol{MM}_2}$ are perpendicular to a tangent vector $\boldsymbol{\alpha}$ of the corresponding contact curves at the meshing point M, that is, $\overrightarrow{\boldsymbol{MM}_1}$ and $\overrightarrow{\boldsymbol{MM}_2}$ both lie on the normal plane π of the corresponding contact curves at meshing point M. Fig. 5. shows the directions of $\overrightarrow{\boldsymbol{MM}_1}$ and $\overrightarrow{\boldsymbol{MM}_2}$, starting from the meshing point M on the first contact curve and the second contact curve, respectively.

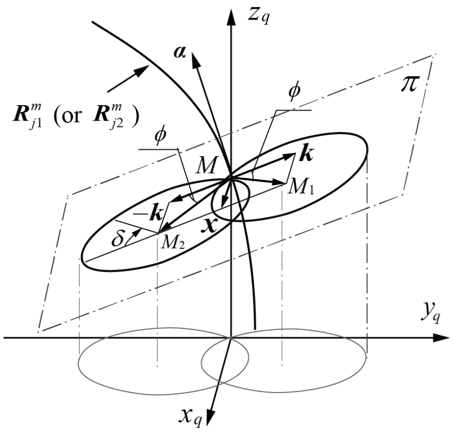

Fig. 5. *The schematic diagram of* $\overrightarrow{\boldsymbol{MM}_1}$ *and* $\overrightarrow{\boldsymbol{MM}_2}$

In the coordinate system $o_q-x_q y_q z_q$, the tangent vector $\boldsymbol{\alpha}$ at the meshing point is expressed as:

$$\boldsymbol{\alpha}=\begin{bmatrix} 0 \\ \dfrac{m_j'}{\sqrt{n_j^2+m_j'^2}} \\ -\dfrac{n_j}{\sqrt{n_j^2+m_j'^2}} \end{bmatrix}. \tag{18}$$

The direction of the vector $\boldsymbol{x}=[1\ 0\ 0]^{\mathrm{T}}$ is utilized to indicate the radially extending of line tooth. The vector $\boldsymbol{k}$ in the normal plane is perpendicular to the vector $\boldsymbol{x}$, which is utilized to indicate the circumferentially extending of line tooth and is expressed as:

$$\boldsymbol{k}=\boldsymbol{x}\times\boldsymbol{\alpha}=\begin{bmatrix} 0 \\ \dfrac{n_j}{\sqrt{n_j^2+m_j'^2}} \\ \dfrac{m_j'}{\sqrt{n_j^2+m_j'^2}} \end{bmatrix}. \tag{19}$$

In the coordinate system $o_q-x_q y_q z_q$, the analytical expressions of $\overrightarrow{\boldsymbol{MM}_1}$ and $\overrightarrow{\boldsymbol{MM}_2}$ can be derived.

$$\overrightarrow{\boldsymbol{MM}_{1(2)}}=r(\boldsymbol{x}\sin\phi\pm\boldsymbol{k}\cos\phi)=r\begin{bmatrix} \sin\phi \\ \pm\dfrac{n_j\cos\phi}{\sqrt{m_j'^2+n_j^2}} \\ \pm\dfrac{m_j'\cos\phi}{\sqrt{m_j'^2+n_j^2}} \end{bmatrix}, \tag{20}$$

where ϕ is a parameter determining the positions of Σ^m_{j1} and Σ^m_{j2}. Usually ϕ is equal to 30°.

The analytical expressions of the tooth surfaces Σ^m_{j1} and Σ^m_{j2} are achieved. δ is a parameter to form the surfaces.

$$\Sigma_{j1(j2)} = r(\boldsymbol{x}\sin\phi \pm \boldsymbol{k}\cos\phi) + r(\boldsymbol{x}\sin\delta \pm \boldsymbol{k}\cos\delta) = r\begin{bmatrix} \sin\phi + \sin\delta \\ \pm\dfrac{n_j(\cos\phi + \cos\delta)}{\sqrt{m_j'^2 + n_j^2}} \\ \pm\dfrac{m_j'(\cos\phi + \cos\delta)}{\sqrt{m_j'^2 + n_j^2}} \end{bmatrix}. \quad (21)$$

Back to the coordinate system $o_m - x_m y_m z_m$, by utilizing the transformation matrix $\boldsymbol{M}_{mq}$, the analytical expressions of $\overrightarrow{\boldsymbol{MM}_1}$ and $\overrightarrow{\boldsymbol{MM}_2}$ are obtained.

$$\overrightarrow{\boldsymbol{MM}_1}^m = -r\sin\phi\begin{bmatrix} k_j\cos\theta_j\cos t_j \\ \cos\theta_j\sin t_j \\ \sin\theta_j \end{bmatrix} + \frac{r\cos\phi}{\sqrt{m_j'^2 + n_j^2}}\begin{bmatrix} -k_j\left(n_j\sin t_j + m_j'\sin\theta_j\cos t_j\right) \\ n_j\cos t_j - m_j'\sin\theta_j\sin t_j \\ m_j'\cos\theta_j \end{bmatrix},$$

$$\overrightarrow{\boldsymbol{MM}_2}^m = -r\sin\phi\begin{bmatrix} k_j\cos\theta_j\cos t_j \\ \cos\theta_j\sin t_j \\ \sin\theta_j \end{bmatrix} - \frac{r\cos\phi}{\sqrt{m_j'^2 + n_j^2}}\begin{bmatrix} -k_j\left(n_j\sin t_j + m_j'\sin\theta_j\cos t_j\right) \\ n_j\cos t_j - m_j'\sin\theta_j\sin t_j \\ m_j'\cos\theta_j \end{bmatrix}. \quad (22)$$

From Eqs. (9), (11) and (22), the first tooth thickness auxiliary curves and the second tooth thickness auxiliary curves were represented as:

$$\boldsymbol{R}_{j1c}^m = \boldsymbol{R}_{j1}^m + \overrightarrow{\boldsymbol{MM}_1}^m,$$
$$\boldsymbol{R}_{j2c}^m = \boldsymbol{R}_{j2}^m + \boldsymbol{M}_{j2j1}^m \cdot \overrightarrow{\boldsymbol{MM}_2}^m, \quad (23)$$

where $\boldsymbol{R}_{11c}^m$ and $\boldsymbol{R}_{12c}^m$ represent the first tooth thickness auxiliary curve and the second tooth thickness auxiliary curve of the driving LG, respectively. $\boldsymbol{R}_{21c}^m$ and $\boldsymbol{R}_{22c}^m$ represent the first tooth thickness auxiliary curve and the second tooth thickness auxiliary curve of the driven LG, respectively.

The analytical expressions of the tooth surfaces Σ_{j1}^m and Σ_{j2}^m in the coordinate system $o_m - x_m y_m z_m$ are also achieved.

$$\Sigma_{j1}^m = \boldsymbol{R}_{j1}^m + \overrightarrow{\boldsymbol{MM}_1}^m + \boldsymbol{r}_{j1},$$
$$\Sigma_{j2}^m = \boldsymbol{R}_{j2}^m + \boldsymbol{M}_{j2j1}^m \cdot (\overrightarrow{\boldsymbol{MM}_2}^m + \boldsymbol{r}_{j2}), \quad (24)$$

where

$$\boldsymbol{r}_{j1} = r\sin\delta\begin{bmatrix} k_j\cos\theta_j\cos t_j \\ \cos\theta_j\sin t_j \\ \sin\theta_j \end{bmatrix} + \frac{r\cos\delta}{\sqrt{m_j'^2 + n_j^2}}\begin{bmatrix} -k_j\left(n_j\sin t_j + m_j'\sin\theta_j\cos t_j\right) \\ n_j\cos t_j - m_j'\sin\theta_j\sin t_j \\ m_j'\cos\theta_j \end{bmatrix},$$

$$\boldsymbol{r}_{j2} = r\sin\delta\begin{bmatrix} k_j\cos\theta_j\cos t_j \\ \cos\theta_j\sin t_j \\ \sin\theta_j \end{bmatrix} - \frac{r\cos\delta}{\sqrt{m_j'^2 + n_j^2}}\begin{bmatrix} -k_j\left(n_j\sin t_j + m_j'\sin\theta_j\cos t_j\right) \\ n_j\cos t_j - m_j'\sin\theta_j\sin t_j \\ m_j'\cos\theta_j \end{bmatrix}. \quad (25)$$

The 'sweep' function in 3D modelling software is usually used to model the line-tooth entity. Firstly, the first contact curve and the first tooth thickness auxiliary curve are plotted by submitting the required parameters into the Eqs. (9) and (16), and a convex arc tooth profile is plotted with a radius of r in a normal plane of the first contact curve. The centre of the arc is located at the first tooth thickness auxiliary curve. Then, the arc tooth profile sweeps along the first contact curve and the first tooth thickness auxiliary curve, taking a role of the trajectory line, by the setting of the tooth profile to be constantly perpendicular to the first contact curve. With the use of 'Swept Blend' to the modelling of line tooth entity in Pro/E, the contact curve should be selected as 'Origin trajectory', along which the tooth profile sweeps, while the corresponding tooth thickness auxiliary curve should be selected as the 'X vector'. Then, 'Perpendicular to the trajectory' should be selected. In another way, with the use of 'Sweep' in Solidworks, the contact curves should be selected as the 'Path', and the corresponding tooth thickness auxiliary curve should be selected as the '1st guide curve'. By selecting of 'Follow path and 1st guide curve', the twist of the intermediate sections is determined by the vector from the path to the first guide curve, so that the tooth profile remains perpendicular to the contact curve. The process above forms a tooth surface containing the first contact curve. Finally, another tooth surface containing the second contact curve is formed by the same method, and the modelling of a line tooth entity is completed.

2 COMPARISON OF SLIDING RATES

The relative sliding between a traditional gear pair might cause surface wear and frictional loss, and then the transmission efficiency and fatigue life of the gears are affected. In general, the sliding rates are one of the tribological parameters and subsequently defined and calculated in theory.

Similar to the traditional gear pair, the sliding rates of the LG pair are defined as the limit value of the ratio of the lengths difference between two relative arcs divided by the length of the given arc [24], they are expressed as Eq. (26).

$$\sigma_1 = 1 - \frac{\sqrt{\left(x'^{(2)}_M\right)^2 + \left(y'^{(2)}_M\right)^2 + \left(z'^{(2)}_M\right)^2}}{\sqrt{\left(x'^{(1)}_M\right)^2 + \left(y'^{(1)}_M\right)^2 + \left(z'^{(1)}_M\right)^2}},$$

$$\sigma_2 = 1 - \frac{\sqrt{\left(x'^{(1)}_M\right)^2 + \left(y'^{(1)}_M\right)^2 + \left(z'^{(1)}_M\right)^2}}{\sqrt{\left(x'^{(2)}_M\right)^2 + \left(y'^{(2)}_M\right)^2 + \left(z'^{(2)}_M\right)^2}}, \tag{26}$$

where σ_1 and σ_2 represent the sliding rates of the driving LG and the driven LG, respectively, $x'^{(j)}_M = \dfrac{dx_j}{dt}$, $y'^{(j)}_M = \dfrac{dy_j}{dt}$, $z'^{(j)}_M = \dfrac{dz_j}{dt}$, $j = 1, 2$.

Taking three couples of LG with vertical cross axes as design examples, the values of various parameters of LG pairs are shown in Table 1. The driving contact curve of the LG pair No. 1 is a circular helix, and the driving contact curves of the LG pair No. 2 and the LG pair No. 3 are conic helixes with a half cone angle of 7°. The heights of the driving LGs are all 16 mm for three examples. The driving contact curves and the driven contact curves can be derived from Eq. (9).

Table 1. *The various parameters of designed the LG pair*

No.	m_1 [mm]	n_1 [mm]	θ_1 [°]	m_2 [mm]	i	θ_0 [°]
1	2.5	4	0	12	8	90
2	1.5	4	7	12	8	90
3	1.8	4	7	12	8	90

The 3D solid models of the LG pairs No. 1 and No. 2 are shown in Fig. 6, with the different shapes of the driving LG.

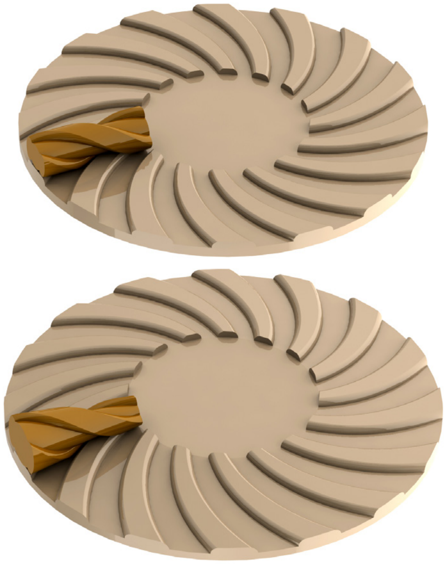

a)

b)

Fig. 6. *3D solid model; a) the LG pair No. 1, b) the LG pair No. 2*

From Eqs. (9) and (26), the sliding rates of contact curves of three LG pairs are obtained and plotted with Wolfram Mathematica, as shown in Fig. 7.

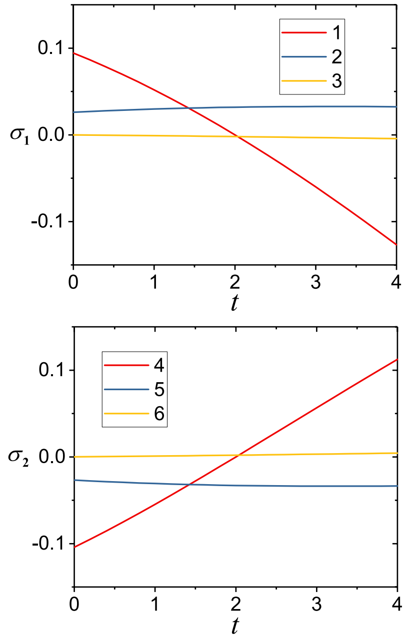

a)

b)

Fig. 7. *Sliding rates of the LG pair No. 1-3; a) σ_1 vs t, b) σ_2 vs t (1-σ_1 of the LG pair No. 1; 2-σ_1 of the LG pair No. 2; 3-σ_1 of the LG pair No. 3; 4-σ_2 of the LG pair No. 1; 5-σ_2 of the LG pair No. 2; 6-σ_2 of the LG pair No. 3)*

From Fig. 7, the sliding rates of the LG pairs, of which the relative position parameters are limited, can be controlled by changing the shape of the driving contact curve. When the driving contact curve is designed by a certain conic helix, the absolute value of sliding rates can be significantly decreased.

3 A KINEMATICS EXPERIMENT

A 3D printing technology, stereolithography appearance (SLA), was adopted to manufacture the samples of the designed LG pair. The surface profile accuracy of the process is 0.025 mm. Fig. 8 shows the prototypes of the manufactured LG pair No. 2; the driving LG is on the left, and the driven LG is on the right.

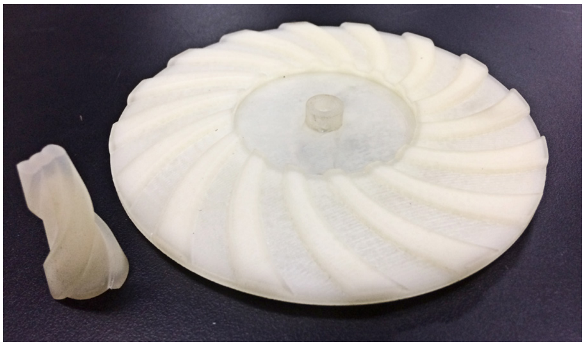

Fig. 8. *The prototypes of the LG pair No. 2*

To measure the transmission ratio of the designed LG pair, a kinematics experiment was conducted by use of a test rig with a 4-DOF positioning table, as shown in Fig. 9.

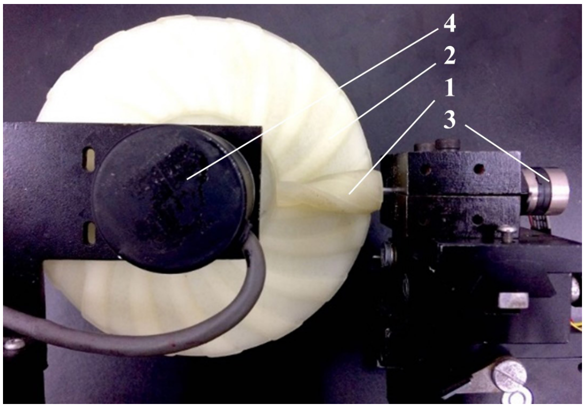

Fig. 9. *The test rig (1-the driving LG;2-the driven LG; 3-a DC motor with the encoder;4-a encoder)*

The driving LG and the driven LG were fixed with encoders and the Decklink SDI to collect their angular rotations in the same time interval. The sampling interval in this experiment was set as 150 ms. Then the instant angular velocity was calculated. The ratio of the instant angular velocity of the driven LG to the driving LG is defined as the instant transmission ratio of the prototype of the designed LGs, as shown in Fig. 10.

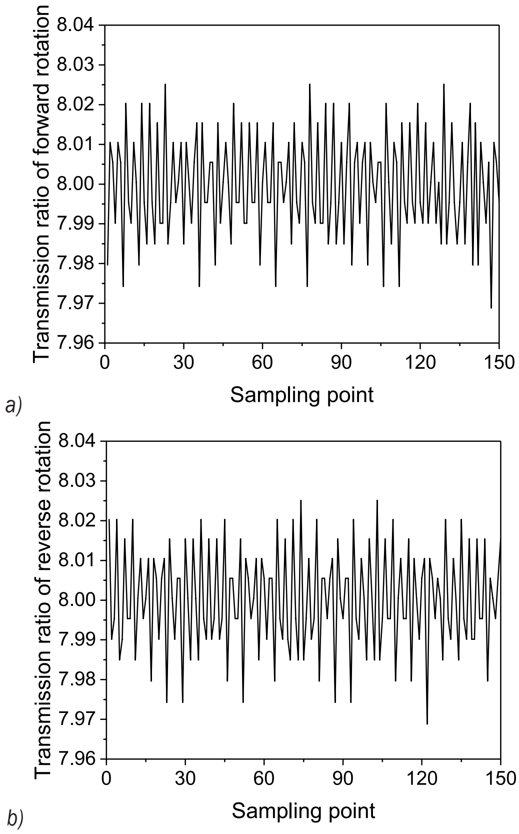

Fig. 10. *The instant transmission ratio; a) under the forward rotation and b) under the reverse rotation*

As shown in Fig. 10, the instant transmission ratios are fluctuating around the theoretical design value of 8, which means the results of the kinematics experiment are consistent with the desired value. The relative error is less than 0.01 %. The maximum instant relative errors under the forward rotation and under the reverse rotation are 0.314 % and 0.389 %, respectively, which may come from the following aspects: manufacturing error of the contact curves, installing error and positioning error, and data errors in collecting and calculating covering original data error, truncation error and round-off error.

4 CONCLUSION

This paper proposed the design methodology of coplanar axes line gear with the controllable sliding rate for non-backlash forward-reverse transmission. The main conclusions include:

(1) The driving contact curve of an LG pair with coplanar axes was extended from a circular helix to a conic helix, and the driven contact curve was derived on the basis of a given driving contact curve. This process provides a new method to control the sliding rates of the contact curves. The design examples show that the LG pair, of which the driving contact curves are conic helixes, possess better sliding rates.

(2) There are two contact curves lying on two sides of a line tooth, and the two couples of contact curves that lie along the driving line tooth and the driven line tooth are two couples of conjugate curves. A line tooth entity, attachment to the wheel body, is formed by a normal arc profile moving along the contact curves and the tooth thickness auxiliary curves. The analytical expressions of spatial cylindrical tooth surfaces are also achieved. The proposed LG pair could be capable of achieving forward-reverse transmission continuously and smoothly without backlash.

However, some issues for the proposed LG pair remain to be studied, covering that selection criterion of the geometric parameters, an experimental measure method of the sliding rates, the failure criteria, bending and contact strength, the efficiency of transmission, etc.

5 ACKNOWLEDGEMENT

The authors gratefully acknowledge the support from National Natural Science Foundation of China (No. 51575191), China Postdoctoral Science Foundation (No. 2017M612652) and Central university basic scientific research service fee (No. 2017B0071).

6 NOMENCLATURE

$\boldsymbol{v}_{12}$ relative velocity at the meshing point between the driving line tooth and the driven line tooth, [m/s]

$\boldsymbol{\beta}$ unit principal normal vector of the driving contact curve at the meshing point,

$o_0-x_0y_0z_0$, $o_1-x_1y_1z_1$ fixed coordinate system and follow-up coordinate system of driving LG,

$o_p-x_py_pz_p$, $o_2-x_2y_2z_2$ fixed coordinate system and follow-up coordinate system of driven LG,

θ_0 shaft angle between driving LG and driven LG, [°]

a distances from point o_0 to o_p, [mm]

t_1, t_2 parameter variable of driving contact curves and driven contact curves,

i transmission ratio,

N_1, N_2 tooth numbers of driving LG and driven LG,

m_1, n_1, m_2, n_2 conical parameters of driving contact curves and driven contact curves, [mm]

θ_1, θ_2 half cone angles of driving contact curves and driven contact curves, [°]

s_1, s_2 line tooth thicknesses of driving LG and driven LG, [mm]

e_1, e_2 space widths of driving LG and driven LG, [mm]

φ_{1FR}, φ_{2FR} phase differences between first contact curve and second contact curve,

$\boldsymbol{\alpha}$ unit tangent vector of the driving contact curve at the meshing point,

$\overrightarrow{\boldsymbol{MM}_1}$, $\overrightarrow{\boldsymbol{MM}_2}$ Contact vector from M to M_1 and M_2,

r arc radius of tooth profile, [mm]

$\boldsymbol{R}_{11}^m$, $\boldsymbol{R}_{12}^m$, $\boldsymbol{R}_{21}^m$, $\boldsymbol{R}_{22}^m$ first contact curve and second contact curve of driving LG and driven LG,

$\boldsymbol{R}_{11c}^m$, $\boldsymbol{R}_{12c}^m$, $\boldsymbol{R}_{21c}^m$, $\boldsymbol{R}_{22c}^m$ first and second tooth thickness auxiliary curves of driving LG and driven LG,

Σ_{11}^m, Σ_{12}^m, Σ_{21}^m, Σ_{22}^m the analytical expressions of tooth surfaces of driving LG and driven LG,

σ_1, σ_2 sliding rates of driving contact curve and driven contact curve.

7 REFERENCES

[1] Litvin, F.L., Fuentes, A. (2004). *Gear Geometry and Applied Theory (2nd ed.)*, Cambridge University Press, New York, **DOI:10.1017/CBO9780511547126**.

[2] Osplack, J.J., Beam, A.S. (1956). *Conical Involute Gearing*. US, US2747424.

[3] Brauer, J. (2002). Analytical geometry of straight conical involute gears. *Mechanism and Machine Theory*, vol. 37, no. 1, p. 127-141, **DOI:10.1016/S0094-114X(01)00062-3**.

[4] Liu, C.C. Tsay, C.B. (2002). Contact characteristics of beveloid gears. *Mechanism & Machine Theory*, vol. 37, no. 4, p. 333-350, **DOI:10.1016/S0094-114X(01)00082-9**.

[5] Staniek, R. (2011). Shaping of face toothing in flat spiroid gears. *Strojniški vestnik - Journal of Mechanical Engineering*, vol. 57, no. 1, p. 47-54, **DOI:10.5545/sv-jme.2010.093**.

[6] Sugimoto, M., Maruyama, N., Nakayama, A., Hitomi, N. (1991). Effect of tooth contact and gear dimensions on transmission errors of loaded hypoid gears. *Journal of Mechanical Design*, vol. 113, no. 2, p. 182-187, **DOI:10.1115/1.2912767**.

[7] Litvin, F.L., Vecchiato, D., Gurovich, E., Fuentes, A., Gonzalez-Perez, I., Hayasaka, K., Yukishima, K. (2005). Computerized developments in design, generation, simulation of meshing, and stress analysis of gear drives. *Meccanica*, vol. 40, no. 3, p. 291-323, **DOI:10.1007/s11012-005-4020-y**.

[8] Tsai, Y.C., Hsu, W.Y. (2008). The study on the design of spiral bevel gear sets with circular-arc contact paths and tooth

profiles. *Mechanism and Machine Theory*, vol. 43, no. 9, p. 1158-1174, **DOI:10.1016/j.mechmachtheory.2007.08.004**.

[9] Alves, J.T., Guingand, M., de Vaujany, J.P. (2013). Designing and manufacturing spiral bevel gears using 5-axis computer numerical control (CNC) milling machines. *Journal of Mechanical Design*, vol. 135, no. 2, p. 024502, **DOI:10.1115/1.4023153**.

[10] Simon, V.V. (2015). Design and manufacture of spiral bevel gears with reduced transmission errors. *Journal of Mechanical Design*, vol. 131, no. 4, p. 041007-041017, **DOI:10.1115/1.3087540**.

[11] Chen, Y.Z. (2014). *Line Gear.* Science Press, Beijing. (in Chinese)

[12] Chen, Y.Z., Xing, G.Q., Peng, X.F. (2007). The space curve mesh equation and its kinematics experiment. *12th IFToMM World Congress*, Besançon.

[13] Chen, Y.Z., Xiang, X.Y., Luo, L. (2009). A corrected equation of space curve meshing. *Mechanism and Machine Theory*, vol. 44, no. 7, p. 1348-1359, **DOI:10.1016/j.mechmachtheory.2008.11.001**.

[14] Ding, J., Chen, Y.Z., Lv, Y.L. (2012). Design of Space-Curve Meshing-Wheels with Unequal Tine Radii. *Strojniški vestnik - Journal of Mechanical Engineering*, vol. 58, no. 11, p. 633-641, **DOI:10.5545/sv-jme.2012.493**.

[15] Chen, Y.Z., Lv, Y.L., Ding, J., Chen, Z. (2013). Fundamental design equations for space curve meshing skew gear mechanism. *Mechanism and Machine Theory*, vol. 70, p. 175-188, **DOI:10.1016/j.mechmachtheory.2013.07.004**.

[16] Chen, Y.Z., Luo, L., Hu, Q. (2009). The contact ratio of a space-curve meshing-wheel transmission mechanism. *Journal of Mechanical Design*, vol. 131, no. 7, p. 074501, **DOI:10.1115/1.3116343**.

[17] Lv, Y.L., Chen, Y.Z., Cui, X.Y. (2015). A contact ratio and interference-proof conditions for a skew line gear mechanism. *Transactions of the Canadian Society for Mechanical Engineering*, vol. 39, no. 3, p. 647-656, **DOI:10.1139/tcsme-2015-0051**.

[18] Chen, Y. Z., Yao, L. (2016). Design formulae for a concave convex arc line gear mechanism. *Mechanical Sciences*, vol. 7 , no. 2, p. 209-218, **DOI:10.5194/ms-7-209-2016**.

[19] Wu, X.T. (2009). *Principle of Gearing.* Jiaotong University Press, Xi'an. (in Chinese)

[20] Li, T., Pan, C., Gao, F., Wang, X. (2012). Research on sliding ratios of conjugate surfaces of two degrees of freedom meshing transmission of spherical gear pair. *Journal of Mechanical Design*, vol. 134 , no. 9, p. 091002, **DOI:10.1115/1.4006322**.

[21] Narayanan, G. (2016). Effect of sliding friction on spline surface failure under misaligned condition in aero engines. *International Journal of Structural Integrity*, vol. 7, no. 5, **DOI:10.1108/IJSI-07-2015-0024**.

[22] Qian, S., Guo, D., Liu, S., Lu, X. (2011). Experimental investigation of lubrication failure of polyalphaolefin oil film at high slide/roll ratios. *Tribology Letters*, vol. 44, no. 2, p. 107-115, **DOI:10.1007/s11249-011-9820-8**.

[23] Ciulli, E., Stadler, K., Draexl, T. (2009). The influence of the slide-to-roll ratio on the friction coefficient and film thickness of EHD point contacts under steady state and transient conditions. *Tribology International*, vol. 42, no. 4, p. 526-534, **DOI:10.1016/j.triboint.2008.04.005**.

[24] Ding, J., Chen, Y. Z., Lv, Y. L., Song, C. (2014). Position-parameter selection criterion for a helix-curve meshing-wheel mechanism based on sliding rates. *Strojniški vestnik - Journal of Mechanical Engineering*, vol. 60, no. 9, p. 561-570, **DOI:10.5545/sv-jme.2013.1574**.

Strojniški vestnik - Journal of Mechanical Engineering 64(2018)6, 373-382

DOI:10.5545/sv-jme.2017.5120
Original Scientific Paper
Received for review: 2017-11-30
Received revised form: 2018-03-18
Accepted for publication: 2018-04-16

Fatigue Design of Ferritic-Pearlitic Nodular Cast Iron Components with Surface Discontinuities

Márton Gróza* – Károly Váradi
Budapest University of Technology and Economics, Department of Machine and Product Design, Hungary

Surface and subsurface discontinuities are one of the most important factors affecting the fatigue life of structural cast components. Their location, shape and size vary from component to component, most of them are completely harmless, but one critical defect can lead to in-service failure. Allowable surface discontinuity size finite element (FE) results can be a practical engineering tool for casting design, process planning, and the quality inspection process. Different methods based on the continuum and fracture mechanics applicable on the multiaxial high-cycle fatigue (HCF) and fatigue limit prediction for components with surface discontinuities are compared with experimental results on ISO1083/JS/500-7 nodular cast iron (NCI). Results also confirm, that the fatigue properties of the analysed material in standards truly represent low-end material strength. A design methodology is presented based on the Defect Stress Gradient approach for the display of an allowable surface discontinuity size FE-result for complex components under proportional loading conditions in HCF.
Keywords: high-cycle fatigue, finite element analysis, fracture mechanics, surface defects, multiaxial fatigue

Highlights

- *Fatigue test results for the ISO1083/JS/500-7 NCI material grade with and without surface discontinuities are compared and analysed.*
- *Different methods are applied to describe the reduction of fatigue strength with the equivalent surface discontinuity size.*
- *Allowable surface discontinuity size FE-results are plotted based on the DSG approach with the consideration of the mean-stress dependent scatter in the fatigue strength.*
- *The proposed method to obtain allowable surface discontinuity size results is directly applicable in industrial applications.*

0 INTRODUCTION

The numerous advantageous characteristics of nodular cast iron (NCI) components, such as their steel-like mechanical properties and economical manufacturability, are linked with a higher level of scatter in material behaviour compared to steels. Engineering materials are classified based on their minimum monotonic tensile properties; therefore, a given standardized NCI grade can contain materials with 100 MPa difference in tensile and fatigue strength. Recommended values for the fatigue strength in standards and design guidelines do not always correspond to the lower-end strength material with the prescribed minimum monotonic properties.

Apart from the large-scale scatter originating from differences in the microstructure and wall-thickness, internal and surface discontinuities also heavily influence the fatigue life of structural cast components. Surface and subsurface discontinuities have the most detrimental effect on the fatigue strength from these factors; their position, size, and morphology vary from component to component. A critical defect can lead to in-service failure, but most of the discontinuities do not affect the expected service life. A fatigue assessment-based quality inspection methodology is, therefore, necessary to balance in-service safety and the economical production of cast components. Allowable surface discontinuity size finite element (FE) result fields are a practical engineering tool during casting design, process planning, and the quality inspection process. The current study employs different methods to obtain the allowable surface discontinuity size as an FE-result field.

Improving the accuracy of the fatigue assessment calculations through the consideration of the non-idealistic properties of components is currently a heavily researched area. Nadot et al. [1] investigated the effect of casting defects of the fatigue limit of NCI material. From the standpoint of the defect-induced fatigue process, each specimen is considered individual during testing. For the assessment of individual fracture events, the "step-by-step" method proposed by Bellows et al. [2] has proven to be essential. Cheng et al. [3] the high frequency cut-off of machined surface topography is defined, which is related to a material parameter a0. Besides, the proposed analytical expressions are applied to predict the stress concentration factors (SCFs derived analytical formulas for the modelling of the surface topography in the fatigue assessment process based on the theory of critical distance. Rotella et al. [4] plotted a defect size map based on FE-calculations for cast A357-T6 under multiaxial loading using the defect stress gradient (DSG) criterion.

*Corr. Author's Address: BME, Department of Machine and Product Design, Műegyetem rkp. 3, Budapest 1111, Hungary groza.marton@gt3.bme.hu

The comparison of experimental and simulation results has shown that the DSG criterion provides a good estimation of the crack initiation sites. Vincent et al. [5] have shown that the defect size that impacts the fatigue limit is largely dependent on the grain size of the material. Schönbauer et al. [6] investigated small artificial surface defects on the torsional and tensile fatigue behaviour of precipitation-hardened chromium-nickel-copper stainless steel. They concluded, that fatigue behaviour is governed by the maximum principal stress even under torsion and emphasized the importance of the crack initiation phase for defects with $\rho \geq 50$ µm notch root radius. Mukherjee et al. [7] analysed the relationship between fatigue and microstructural properties in NCI material with cooling rate calculations, microstructural characterization by 2D SEM and 3D X-ray tomography and fatigue testing on sand and metal moulded samples.

Casting defects can be considered to be notches with complex morphology; most of the advancements in the area of notched fatigue research are, therefore, applicable with some modifications. The effect of notches on the crack initiation life can be approached from the standpoint of fracture mechanics with the analysis of short-crack propagation. Ostash et al. [8] applied a fracture mechanics approach for macrocrack initiation life computation on notched mild-steel and aluminium specimens with promising results. A conventional stress-strain based approach was applied in the work of Gates and Fatemi [9] for multiaxial notched fatigue analysis with the utilization of the theory of critical distances and the Fatemi-Socie critical plane damage parameter. New approaches are currently being developed for a unified description of the total fatigue life; Liu et al. [10] proposed a method based on the theory of damage mechanics to describe damage evolution in a notched specimen.

The current study compares different approaches to simulate the Kitagawa diagram (fatigue strength vs surface discontinuity size) for ISO1083/JS/500-7 NCI material. These methods are used to plot equivalent allowable surface discontinuity size FE-results. Experimental and literature fatigue data are compared to quantify the scatter in the defect-free fatigue properties. Design values of the surface discontinuity size-dependent fatigue strength are derived to ensure safety during the quality inspection process.

1 EXPERIMENTAL RESULTS FOR NCI MATERIAL

As part of a large-scale research program with the aim of improving the fatigue design of NCI components, load-controlled fatigue tests have been conducted on specimens with different microstructures and surface properties. The material chosen for this analysis is a ferritic-pearlitic NCI, designated as ISO1083/JS/500-7 according to the international standard ISO 1083 [11].

1.1 Results with Artificial Surface Defects and Casting Skin

One hundred (100) fatigue test specimens with a rectangular cross-section were created with a complex artificial surface defect introduced by means of a special casting core. Fig. 1 shows the specimen geometry and computed tomography (CT) image from the longitudinal cross-section. The equivalent size of the artificial complex defect is 2110 µm according to the $\sqrt{area}$ parameter from Murakami [12]. A detailed view of the surface defect in the specimens can be seen in Fig. 2. The chemical composition shown in Table 1 is consistent with the expectations to achieve a casting material for the ISO1083/JS/500-7 grade. In Table 1, Sc refers to the degree of saturation, and has been calculated as $Sc = \%C/(4.23 - 0.3 \cdot (\%Si + \%P))$. An evaluation of the obtained microstructural features in accordance to ISO 945-1 [13] is summarized in Table 2. The metallographic inspections were conducted on a cross-section of the clamping area from a tensile specimen. B8×40 (DIN 50125 [14]) tensile specimens have been machined to standard ISO 1083 Y1-shaped test samples with 265 mm length. The tensile tests were carried out at room temperature according to EN ISO 6892-1 [15]. The average values of 12 tensile tests are a proof strength of $R_{p0.2} = 348 \pm 21$ MPa, an ultimate tensile strength of and an elongation at fracture of $R_m = 583 \pm 43$ MPa and an elongation at fracture of $A = 14\ \% \pm 2\ \%$.

Table 1. *Average chemical composition of the test specimens (average of five measurements)*

%C	%Si	%Mn	%P	%S	%Cr	%Cu	%Mg	Sc
3.62	2.33	0.19	0.013	0.005	-	0.36	0.04	1.03

Table 2. *Average metallographic properties of the test specimens (average of five measurements)*

Graphite [%]	Nodules [1/mm²]	Nodularity [%]	Form III [%]	Form IV [%]	Form V [%]	Form VI [%]	Pearlite cont. [%]	Size
10.7±0.14	657±207	88.8±1	0.84±0.15	0.24±0.1	28±2.6	70.92±2.6	46.6±3.8	6

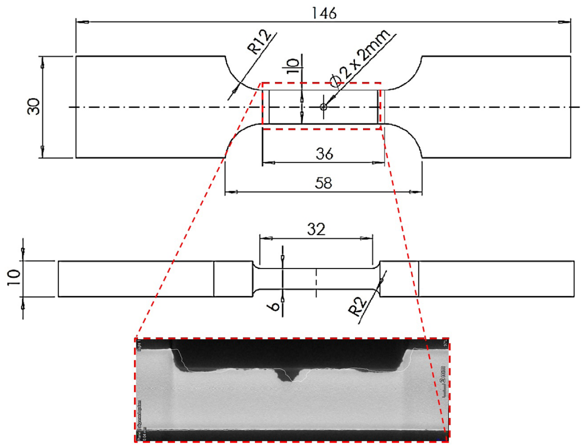

Fig. 1. *Fatigue test specimen with casting skin and complex artificial surface defect, CT image of the cross-section of the gauge length*

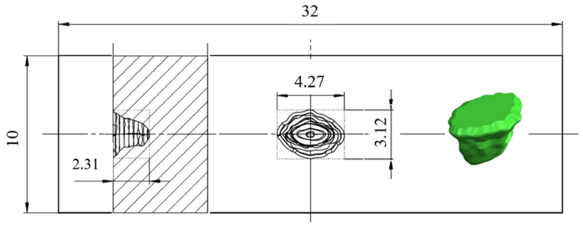

Fig. 2. *Geometry of the testing section of the fatigue test specimen with casting skin and complex artificial surface defect*

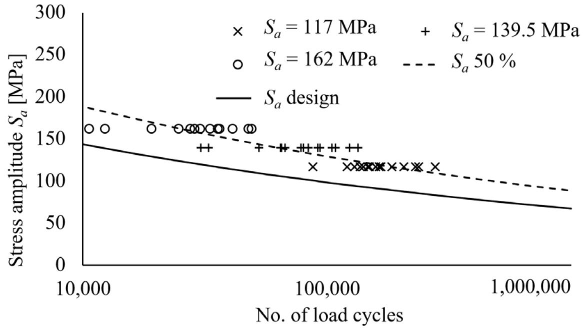

Fig. 3. *Design and 50 % failure probability S-N curves for defective ISO1083/JS/500-7 with the test results for $R_{0.1}$ pulsating tensile load*

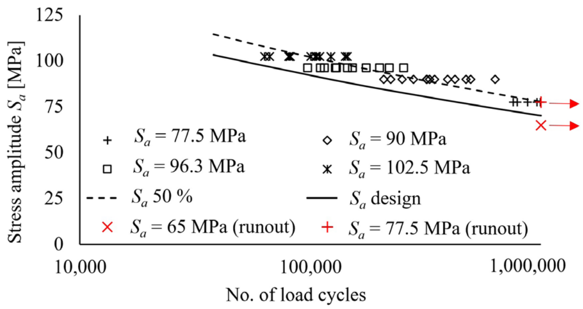

Fig. 4. *Design and 50 % failure probability S-N curves for defective ISO1083/JS/500-7 with the test results for $R_{0.5}$ pulsating tensile load*

Fatigue tests were carried out on a RUMUL MAGNODYN fatigue machine at room temperature at $R_{0.1}$ and $R_{0.5}$ pulsating tension loads with fixed amplitude with a testing frequency of 40 Hz. Cracks initiated exclusively from the large artificial defect.

Fig. 3 and 4 show the fitted and the design (97.5 % failure probability and 95 % significance level considering the lognormal distribution of fatigue life) S-N curves with the experimental data for $R_{0.1}$ and $R_{0.5}$ pulsating tension load.

1.2 Results for Low and High-Strength Material

Fatigue tests were conducted on low- and high-strength ISO1083/JS/500-7 material, to estimate the possible scatter in the high-cycle fatigue properties of smooth specimens. The specimens have been machined from NCI components from the production line, the distinction "low" and "high" strength refers to different batches of the same component. The tensile properties of the studied materials were determined on B8×40 (DIN 50125 [14]) tensile specimens according to the standard EN ISO 6892-1 [15] and are summarized in Table 3.

The geometries of the fatigue test specimens are displayed in Fig. 5. The fatigue tests were carried out on an INSTRON 8874 servo-hydraulic fatigue machine with a fixed-load ratio of R0.05 and a fixed-load maximum with a testing frequency of 30 Hz. In the case of the low-strength material, fatigue testing was carried out at three different stress levels to obtain the full S-N curve.

In the case of the high-strength cast iron, the step-by-step method [2] was applied with 20 MPa steps in the stress maximum to determine the fatigue strength at 10^6 cycles.

Fracture surfaces were analysed, and the initiation sites were located in the near-surface region without the influence of notable subsurface or internal defects. Results are summarized in Table 4.

It is interesting to note that the previous loading steps below the fatigue limit do not have a noticeable impact in the fatigue strength; therefore, the application of the step-by-step approach in the fatigue testing process is justified. Fig. 6 shows the obtained test results with the fitted S-N curve and the S-N curve based on the FKM guideline [16].

Table 3. *Summary of tensile monotonic and fatigue strength at cycles for the ISO1083/JS/500-7 cast iron material at different R-ratios*

Designation	$R_{p0.2}$ [MPa]	R_m [MPa]	A [%]	σ_{R-1} [MPa]	σ_{R0} [MPa]	$\sigma_{R0.05}$ [MPa]	$\sigma_{R0.1}$ [MPa]	$\sigma_{R0.36}$ [MPa]	$\sigma_{R0.5}$ [MPa]
FKM [16]	320	500	7	170	135	-	-	-	-
low-strength	328	491	15	(194)	-	135	-	-	-
high-strength	378	649	9.7	(277)	-	188	-	-	-
Yamabe and Kobayashi [17]	363	555	8	275	-	-	-	-	-
Rabb [18]	338	625	-	260	-	-	160	120	-
artificial defect	348	583	14	(119)	-	-	88	-	78

Table 4. *Fatigue test results for the high-strength ISO1083/JS/500-7 material*

No.	No. of cycles	σ_{max}^{test} [MPa]	$\sigma_{R0.05}^{10^6}$ [MPa]
1	1,000,000	325	184
	1,000,000	345	
	1,000,000	365	
	1,000,000	385	
	153,644	405	
2	1,000,000	385	193
	1,000,000	405	
	80,476	425	
3	855,122	405	190
4	1,000,000	385	185

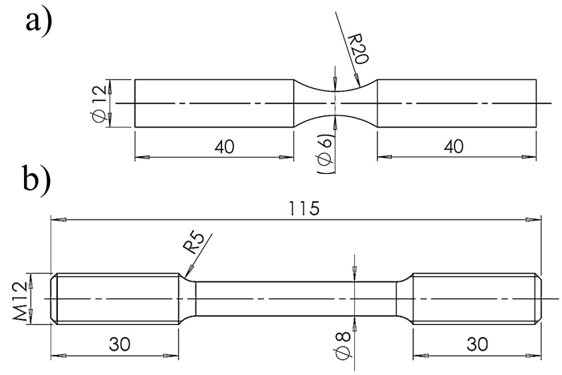

Fig. 5. *Specimen geometry for a) high-strength material and b) low-strength material testing*

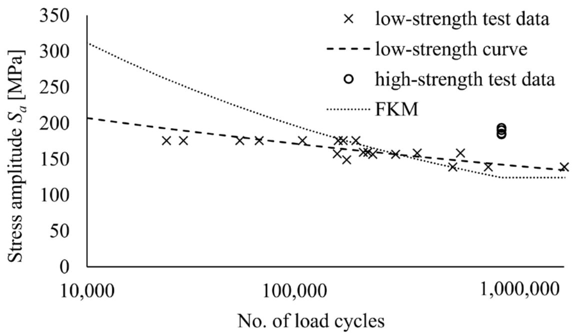

Fig. 6. *Comparison of experimental results and the FKM calculation guideline [16] at $R_{0.05}$ pulsating tensile load for low- and high-strength ISO1083/JS/500-7*

2 FATIGUE LIFE OF ISO1083/JS/500-7 NCI

Table 3 provides a quick view of monotonic tensile strength and tensile fatigue strength at 10^6 cycles of the investigated material. If no tests were conducted at R-1 tension, an estimated value of the fully-reversed fatigue strength obtained by the Goodman approach is shown in brackets for an easier comparison of the different results.

Fig. 7 shows the effect of mean stress on the stress amplitude corresponding to fracture at 10^6 cycles. The modified Goodman approach is used due to its simplicity and slight conservatism for the simulation of the mean stress effect. For the description of the mean test results the mean value of $\sigma_{R-1}^{10^6}$ and the mean value of the yield strength was used to fit the modified Goodman curve.

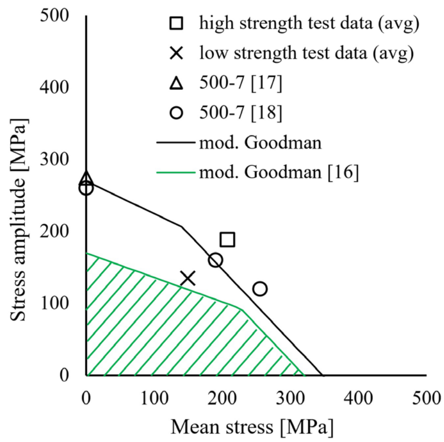

Fig. 7. *Effect of mean stress on the fatigue limit of ISO1083/JS/500-7, experimental results and the modified Goodman curve at 10^6 cycles*

The fatigue data included in the FKM guideline **[16]** proves to be a good estimate of the low-strength ISO1083/JS/500-7 fatigue properties. Based on FKM **[16]** data and the modified Goodman approach, a design curve is proposed for the defect-free material by using the values for $\sigma_{R-1}^{10^6}$ and $R_{p0.2}$ from the guideline.

3 FATIGUE LIFE OF MATERIAL WITH SURFACE DISCONTINUITIES

The current study employs four concurrent approaches to simulate the relationship between equivalent surface discontinuity size and the fatigue limit, which is the Kitagawa curve in other terms.

3.1 The Defect Stress Gradient Method

The DSG methodology from Vincent et al. [19] in previous work [Leopold G, Nadot Y. J ASTM Int 7:2010], to represent the effect of a defect in the fatigue criterion by means of a stress gradient term. This general methodology called Defect Stress Gradient (DSG describes the effect of surface discontinuities on the high-cycle fatigue strength under multiaxial loading conditions. The local hot-spot stress is modified with a defect and material-type dependent stress gradient function. In the current analysis, the approach is applied with the Crossland equivalent stress, characterizing the multiaxial fatigue strength of the defect-free material, which limits the application to proportional loading conditions. The Crossland parameters have been identified on the fatigue limits for three different loading types based on the experimental results of Nadot et al. [1] on defect-free NCI, and are α_{Cr}=1.13 and β_{Cr}=255 MPa. The a_∇ parameter describes the effect of the defect on the multiaxial fatigue strength for spherical surface defects and is $a_\nabla = 209$ µm.

The equivalent DSG stress σ_{DSG} predicts crack initiation at the value β_{Cr}, and is calculated with the equation:

$$\sigma_{DSG} = \sigma_{Cr}^{\max} - a_\nabla \frac{\sigma_{Cr}^{\max} - \sigma_{Cr}^{0}}{\sqrt{area}} \leq \beta_{Cr}, \tag{1}$$

where $\sigma_{Cr}^{\max}$ is the maximum of the Crossland equivalent stress at the tip of the defect, σ_{Cr}^{0} is the stress at the same location without the stress concentration effect of the defect. The Crossland equivalent stress is calculated with the following equation for a representative load cycle:

$$\sigma_{Cr} = \sqrt{J_{2}}_{a} + \alpha_{Cr}\sigma_{h,\max}. \tag{2}$$

With the simplification, that the ratio $\sigma_{Cr}^{\max} / \sigma_{Cr}^{0}$ is equal to the theoretical elastic stress concentration factor for hemispherical surface defects in an infinite body $K_t^{sph} = 2.06$, the allowable hemispherical surface defect size $\sqrt{area}_{all.sph}^{DSG}$ can be expressed according to the following equation:

$$\sqrt{area}_{all.sph}^{DSG} = a_\nabla \frac{\sigma_{Cr}^{0}\left(K_t^{sph} - 1\right)}{K_t^{sph}\sigma_{Cr}^{0} - \beta_{Cr}}. \tag{3}$$

3.2 The Murakami Approach

The Murakami approach [20] provides a good estimate of the fatigue limit for a large number of different defective materials. It has undergone several smaller developments over the years, which has led to robust applicability. The fatigue limit σ_w can be expressed for a given equivalent defect size $\sqrt{area}$ and load ratio R:

$$\sigma_w = F_{loc}\left(H_V + 120\right)\left(\sqrt{area}\right)^{-1/6} \cdot \left[\frac{(1-R)}{2}\right]^{\alpha}, \tag{4}$$

where F_{loc} is the location factor and is 1.43 for a surface defect; α is a material parameter and is given as $0.371 + H_V \cdot 10^{-4}$ for NCI material.

The calculation process can be used to express the allowable equivalent defect size $\sqrt{area}_{all.sc}^{Murakami}$ with short crack considerations:

$$\sqrt{area}_{all.sc}^{Murakami} = \left(\frac{F_{loc}\left(H_V + 120\right)\left[\frac{(1-R)}{2}\right]^{\alpha}}{\sigma_{I.eff}^{amp}}\right)^{6}. \tag{5}$$

H_V=200 hardness was considered for the investigated NCI material as the main input parameter of the Murakami approach.

A differentiation is given for $\sqrt{area} \geq 1000$ µm, where the equivalent crack is considered to be microstructurally long. In this regime, the threshold stress intensity factor (SIF) range for crack propagation is a constant value, estimated as:

$$\Delta K_{th}^{lc} = 3.3 \cdot 10^{-3} \cdot (H_V + 120) \cdot \sqrt{1000}^{\frac{1}{3}} \cdot \left[\frac{(1-R)}{2}\right]^{\alpha}. \tag{6}$$

This leads to the following equation for the equivalent defect size $\sqrt{area}_{all.lc}^{Murakami}$ with long crack considerations:

$$\sqrt{area}_{all.lc}^{Murakami} = \frac{1}{\pi}\left(\frac{\Delta K_{th}^{lc}}{Y \Delta\sigma_{I.eff}}\right)^{2}. \tag{7}$$

3.3 Fatigue Limit Prediction with Linear Elastic Fracture Mechanics

Considering complete equivalence between surface defects and cracks of equivalent size, linear elastic fracture mechanics (LEFM) can be applied to model the state of the crack propagation threshold, in other terms the fatigue limit. The NASGRO crack growth model by Forman and Mettu [21] describes the phenomenon of crack closure with a crack-opening function from Newman [22].

The NASGRO model for the NCI material of interest has been calibrated on the experimental results of Björkblad [23]. The threshold stress intensity range in the NASGRO model is calculated as follows:

$$\Delta K_{th} = \Delta K_0 \sqrt{\frac{a}{a+a_0}} \left[\frac{1-f}{(1-A_0)(1-R)} \right], \tag{8}$$

where $a=\sqrt{area}$ is the crack length, $Y=2/\pi$ is the shape factor at the bottom of a hemispherical surface crack embedded in an infinite body under tension. The material parameters considered in the calculations are summarized in Table 5. The allowable equivalent defect size $\sqrt{area}_{all}^{LEFM}$ according to the LEFM approach is given by:

$$\sqrt{area}_{all}^{LEFM} = \frac{1}{\pi} \left(\frac{\Delta K_{th}}{Y \Delta\sigma_{I.eff}} \right)^2. \tag{9}$$

Table 5. *Material properties for the NASGRO model for ISO1083/JS/500-7, based on experimental data from* [23]

Symbol	Value	Unit
a_0	0.038	mm
α	2.5	-
S_{max} / σ_0	0.3	-
ΔK_0	7.5	$\text{MPa}\sqrt{\text{m}}$
C_{th+}	1	-

3.4 Fatigue Limit Prediction with The Effective Threshold

The equivalence of surface defects and cracks with the same size considered in the LEFM approach is, however, not fully correct. Long fatigue cracks have plastic wake along the crack path, whereas a crack initiated from a defect is a short crack with different parameters to consider in a crack propagation analysis. From a theoretical standpoint, cracks initiated from defects should be modelled with the equivalent size of the defect with the application of the threshold for microstructural crack initiation $\Delta K_{th.eff}$. The effective threshold SIF range is independent of the load ratio. The equivalent allowable defect size can be estimated with the following equation:

$$\sqrt{area}_{all}^{\Delta K_{th.eff}} = \frac{1}{\pi} \left(\frac{\Delta K_{th.eff}}{Y \Delta\sigma_{I.eff}} \right)^2, \tag{10}$$

where $\Delta K_{th.eff} = 3.75\ \text{MPa}\sqrt{\text{m}}$ based on the experimental results of Nadot et al. [24].

3.5 Comparison with Experimental Results

Figs. 8 to 10 show the comparison between the simulated curves with the different methods and the experimental results. The results obtained on specimens with complex artificial defects are displayed with the mean fatigue strength at cycles with a scatter band of three times the standard deviation. Some of the experimental data used for comparison originate from the work of Nadot et al. [1].

The fracture mechanics method based on the effective threshold SIF range ($\Delta K_{th.eff}$) leads to highly conservative results compared to specimens cycled until complete fracture. This approach models the start of microcrack propagation, hence it neglects parts of both the crack initiation and propagation phases. The fracture mechanics method utilizing the threshold SIF range (ΔK_{th}) can lead to non-conservative results in cases of small defects, but overall describes the Kitagawa relationship well at different load ratios. This approach considers complete equivalence between surface defects and fatigue cracks, which can be a non-conservative assumption since cracks initiating from defects do not have the same closure levels as fully formed fatigue cracks of the same size do. The method of Murakami has a good general description of the Kitagawa-curve for ferritic-pearlitic NCI. This approach, however, should be applied carefully, since the utilized H_V–$\Delta K_{th.eff}$ correlation does not necessarily stand for the high-strength ferritic NCI grades. The DSG approach also models the multiaxial fatigue behavior of the defect-free and defective material in the HCF range as well, and therefore more general than the other analysed methods do.

The curves recommended for design have been derived from the curves obtained with the DSG approach with the application of a safety factor estimated from the scatter of the defect-free results for this material grade. The mean stress-dependent safety factor is essentially the distance of the mean experimental and design curves on the Haigh diagram in Fig. 7. Its value is 1.64 for R_{-1}, 1.58 for $R_{0.1}$, and $R_{0.5}$ due to the smaller level of scatter in strength under higher mean stresses.

4 ALLOWABLE DISCONTINUITY SIZE MAPS

The derived formulas for the allowable surface discontinuity size can be used to plot corresponding FE-results for a general complex case. Within the DSG approach the Crossland equivalent stress is employed to describe multiaxial loading effects. For the Murakami and the fracture mechanics-based approaches, the maximum principal stress range can be used to describe multiaxial stress states, since that corresponds to the crack opening mode in fracture mechanics. It has to be noted, that these criteria are only applicable to proportional loading conditions.

A simple analysis example is employed to demonstrate the allowable discontinuity size FE-results obtainable by the methods introduced in Chapter 3. Fig. 11 shows the analysis setup for a rectangular 3D body under pure bending. The R0 cyclic load was set up with the aim of inducing bending stresses leading to first yield according to the standard proof strength of 320 MPa at the maximum load. E=169 GPa and υ=0.275 were applied to set up the linear elastic material model for the FE-solution.

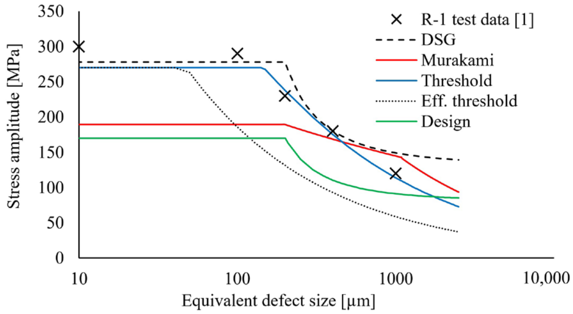

Fig. 8. *Kitagawa curves for R_{-1} tension-compression for NCI with artificial surface defects, with additional experimental results from* **[1]**

The simulations were conducted with ANSYS Academic Research 17.2 software.

Fig. 12 shows the allowable discontinuity size maps obtained by the different approaches. The

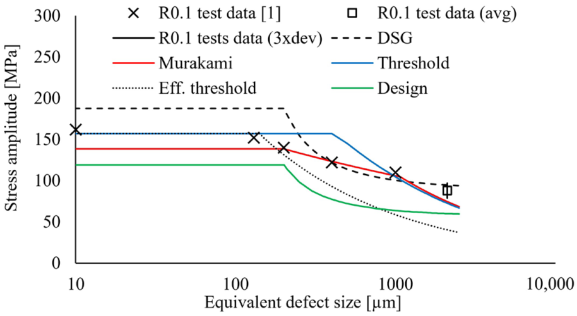

Fig. 9. *Kitagawa curves for $R_{0.1}$ tension for NCI with artificial surface defects, with additional experimental results from* **[1]**

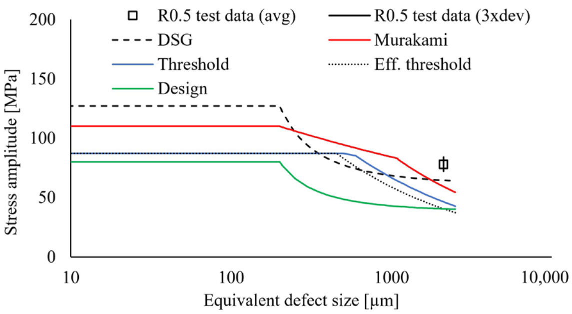

Fig. 10. *Kitagawa curves for NCI under $R_{0.5}$ tension loading with artificial surface defects*

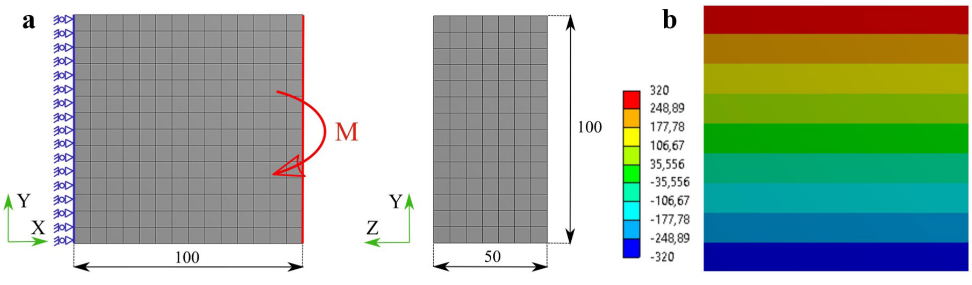

Fig. 11. *a) FEA model setup and b) the normal stress [MPa] result field at the maximal load*

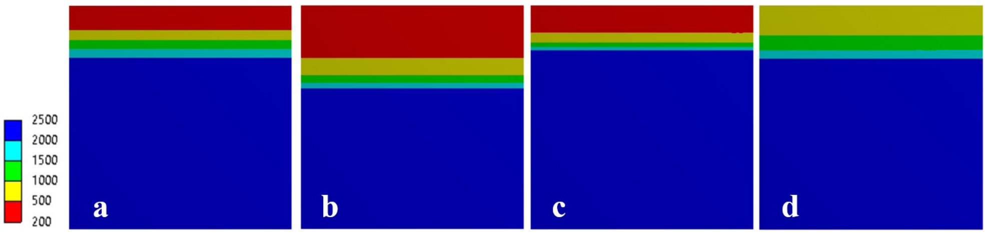

Fig. 12. *Allowable discontinuity size FE-result fields with a) Murakami's, b) effective threshold, c) DSG and d) LEFM approaches*

differences of the compared approaches follow the trend discussed in Chapter 3.5. Fig. 13 displays the design values of the allowable surface discontinuity size derived from the results obtained with the DSG approach with the application of the mean stress-dependent safety factor. Illustrations of the corresponding discontinuity sizes are linked with the different colour bands to provide some level of physical connection. From the illustration of the proposed methodology, it can be concluded that even large surface defects can be tolerable from the standpoint of safe in-service life, if their position on the component is carefully monitored. In the current case displayed on Fig. 13, 1 mm to 1.5 mm surface defects can be allowed on more than two thirds of the component surface, which is marked by blue on the defect size map. (The legend indicates 1.5 mm to 2 mm for this colour band, but the distribution inside one band is unknown. For this reason, the allowed defect size range is shifted to a lower class.) The area-ratio of the different colour bands is governed by the nature of the Kitagawa diagram, which shows a decreasing sensitivity (especially the DSG approach) to the increase of the defect size in the investigated range. The critical area, where no discontinuities are allowed, must be generally quite narrow, otherwise the component would not even comply with the traditional fatigue assessment.

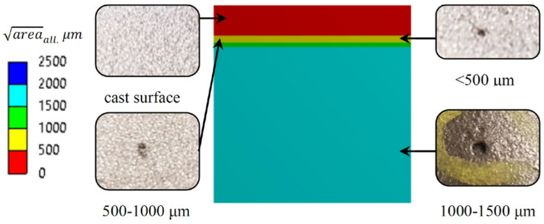

Fig. 13. *Allowable discontinuity size FE-result field for design with the DSG approach*

5 CONCLUSIONS

Fatigue tests have been conducted to analyse the scatter of fatigue properties for the ISO1083/JS/500-7 NCI material grade. A 40 % difference in the fatigue strength ($\sigma_{R0.05}^{10^6}$) is possible between polished samples machined from 500-7 NCI components. The step-by-step [2] approach has proven to give good results for the analysed material; the loading history below the fatigue limit had a negligible effect on the fatigue strength at load cycles. Different methods applicable to the assessment of surface discontinuities have been compared in the current paper.

Allowable surface defect size maps have been plotted for a simple analysis example: for the comparison of the methods in their planned field of application. Surface discontinuities of 1000 μm can reduce the fatigue strength of NCI by a factor of 2.5. (hemispherical defects in cylindrical test specimens under R_{-1} tension-compression [1]).

The fracture mechanics method based on the effective threshold SIF range ($\Delta K_{th.eff}$) leads to highly conservative results compared to specimens cycled till complete fracture.

The fracture mechanics method utilizing the threshold SIF range (ΔK_{th}) can lead to non-conservative results in case of small defects, but overall describes the Kitagawa relationship well at different load ratios.

The method of Murakami has a good general description of the Kitagawa-curve for ferritic-pearlitic NCI. This approach however should be applied carefully, since the utilized H_V–ΔK_{th} correlation does not necessarily stand for the high-strength ferritic NCI grades.

The DSG approach also models the multiaxial fatigue behaviour of the defect free and defective material in the HCF range and is, therefore, more general than the other analysed methods.

The fatigue properties recommended by the FKM Guideline [16] are in good agreement with the tested low-strength ISO1083/JS/500-7 material; they truly represent the lower end mechanical properties for this grade.

6 ACKNOWLEDGEMENTS

The recent study was realized within the Knorr-Bremse Scholarship Program supported by the Knorr-Bremse Rail Systems Budapest.

7 NOMENCLATURES

a_∇	material parameter in the DSG criterion, [μm]
a_0	material constant depending on the microstructure, [mm]
A_0	component of the crack-opening function by Newman, [-]
$\sqrt{area}$	equivalent defect size from Murakami, [MPa]
C_{th+}	fitting parameter describing the R-dependence of ΔK_{th}, [-]
E	modulus of elasticity, [GPa]
f	crack-opening function by Newman, [-]
F_{loc}	location factor, [MPa]
H_V	Vickers hardness, [MPa]

$\sqrt{J_{2\,a}}$ amplitude of the square root of the second invariant of the deviatoric stress tensor in a load cycle, [MPa]
R fatigue load ratio, [-]
$R_{p0.2}$ monotonic proof strength at 0.2 % elongation, [MPa]
R_m ultimate tensile strength, [MPa]
$S_{\max}/\sigma_0$ ratio of the maximum applied stress to the flow stress in the NASGRO model, [-]
α plane stress/plain strain constraint, [-]
α_{Cr} material parameter in the Crossland criterion, [-]
β_{Cr} material parameter in the Crossland criterion, [MPa]
ΔK_0 the value of ΔK_{th} at R_0, [MPa√m]
ΔK_{th} crack propagation threshold stress intensity factor range, [MPa√m]
$\Delta K_{th.eff}$ effective value of the threshold stress intensity factor, [MPa√m]
σ_{max}^{test} applied cyclic stress max., [MPa]
$\sigma_a^{10^6}$ fatigue strength in stress amplitude at 10^6 cycles, [MPa]
$\sigma_{RX}^{10^6}$ fatigue strength in stress amplitude at 10^6 cycles and load ratio "X", [MPa]
σ_{Cr} Crossland equivalent stress, [MPa]
$\sigma_{h,\max}$ max. of the hydrostatic stress in a load cycle, [MPa]
σ_w fatigue limit for a given load-ratio, [MPa]
$\sigma_{I.eff}^{amp}$ the effective maximum principal stress amplitude, [MPa]
$\Delta\sigma_{I.eff}$ the effective maximum principal stress range, [MPa]
υ Poisson's ratio, [-]

8 REFERENCES

[1] Nadot, Y., Mendez, J., Ranganathan, N., (2004). Influence of casting defects on the fatigue limit of nodular cast iron. *International Journal of Fatigue*, vol. 26, no. 3, p. 311-319, **DOI:10.1016/S0142-1123(03)00141-5**.

[2] Bellows, R.S., Muju, S., and Nicholas, T. (1999). Validation of the step test method for generating haigh diagrams for Ti – 6Al – 4V. *International Journal of Fatigue*, vol. 21, no. 7, p. 687-697, **DOI:10.1016/S0142-1123(99)00032-8**.

[3] Cheng, Z., Liao, R., Lu, W., Wang, D. (2017). Fatigue notch factors prediction of rough specimen by the theory of critical distance. *International Journal of Fatigue*, vol. 104, p. 195-205, **DOI:10.1016/j.ijfatigue.2017.07.004**.

[4] Rotella, A., Nadot, Y., Augustin, R., Piellard, M., L'Heritier, S. (2017). Defect size map for cast A357-T6 component under multiaxial fatigue loading using the defect stress gradient (DSG) criterion. *Engineering Fracture Mechanics*, vol. 174, p. 227-242, **DOI:10.1016/j.engfracmech.2016.12.008**.

[5] Vincent, M., Nadot, Y., Nadot-Martin, C., Dragon, A. (2016). Interaction between a surface defect and grain size under high cycle fatigue loading: Experimental approach for Armco iron. *International Journal of Fatigue*, vol. 87, p. 81-90, **DOI:10.1016/j.ijfatigue.2016.01.013**.

[6] Schönbauer, B.., Yanase, K., Endo, M. (2017). Influences of small defects on torsional fatigue limit of 17-4PH stainless steel. *International Journal of Fatigue*, vol. 100, part 2, p. 540-548, **DOI:10.1016/j.ijfatigue.2016.12.021**.

[7] Mukherjee, K., Fæster, S., Hansen, N., Dahl, A.B., Gundlach, C., Frandsen, J.O., Sturlason, A. (2017). Graphite nodules in fatigue-tested cast iron characterized in 2D and 3D. *Materials Characterization*, vol. 129, p. 169-178, **DOI:10.1016/j.matchar.2017.04.024**.

[8] Ostash, O.P., Chepil, R.V., Vira, V.V. (2017). On the assessment of fatigue life of notched structural components. *International Journal of Fatigue*, vol. 105, p. 305-311, **DOI:10.1016/j.ijfatigue.2017.09.007**.

[9] Gates, N., Fatemi, A. (2016). Notch deformation and stress gradient effects in multiaxial fatigue. *Theoretical and Applied Fracture Mechanics*, vol. 84, p. 3-25, **DOI:10.1016/j.tafmec.2016.02.005**.

[10] Liu, J., Zhang, R., Wei, Y., Lang, Sh. (2017). A new method for estimating fatigue life of notched specimen. *Theoretical and Applied Fracture Mechanics*, **DOI:10.1016/j.tafmec.2017.07.017**.

[11] ISO 1083:2004(E). *Spheroidal Graphite Cast Irons — Classification*. International Organization for Standardization, Geneva, p. 31.

[12] Murakami, Y. (2002). *Metal Fatigue: Effects of Small Defects and Nonmetallic Inclusions*, Elsevier Science, Oxford.

[13] ISO 945-1:2017. *Microstructure of Cast Irons — Part 1: Graphite Classification by Visual Analysis*, International Organization for Standardization, Geneva.

[14] DIN 50125:2016-12. T*esting of metallic materials - Tensile test pieces*, DIN, Berlin.

[15] ISO 6892-1:2016. *Metallic Materials - Tensile Testing - Part 1: Method of Test at Room Temperature*, International Organization for Standardization, Geneva.

[16] FKM (2012). *Analytical Strength Assesment of Components*, VDMA Verlag, Frankfurt am Main.

[17] Yamabe, J., Kobayashi, M. (2006). Influence of casting surfaces on fatigue strength of ductile cast iron. *Fatigue & Fracture of Engineering Materials & Structures*, vol. 29, no. 6, p. 403-415, **DOI:10.1111/j.1460-2695.2006.01017.x**.

[18] Rabb, B.R. (2004). Influence of Occasional Underloads on Fatigue. *European Congress on Computational Methods in Applied Science and Engineering*, Jyväskylä, p. 229-250.

[19] Vincent, M., Nadot-Martin, C., Nadot, Y., Dragon, A. (2014). Fatigue from defect under multiaxial loading: defect stress gradient (DSG) approach using ellipsoidal equivalent inclusion method. *International Journal of Fatigue*, vol. 59, p. 176-187, **DOI:10.1016/j.ijfatigue.2013.08.027**.

[20] Murakami, Y. (2002). *Mechanism of Fatigue in the Absence of Defects and Inclusions. Metal Fatigue: Effects of Small Defects and Nonmetallic Inclusions*. Elsevier Science Oxford, **DOI:10.1016/B978-008044064-4/50001-3**.

[21] Forman, G.R., Mettu, S.R. (1990). Behavior of surface and corner cracks subjected to tensile and bending loads in Ti-6A1-4V Alloy, *NASA Technical Memorandum*, NASA, Houston.

[22] Newman, J.C. Jr. (1984). A crack opening stress equation for fatigue crack growth. *International Journal of Fracture*, vol. 24, no. 4, p. R131-R135, **DOI:10.1007/BF00020751**.

[23] Björkblad, A. (2005). Conventional vs. closure free crack growth in nodular iron. Samuelsson, J., Marquis, G. (eds.). *Competent Design by Castings Conference: Improvements in a Nordic Project*, p. 273-286.

[24] Nadot, Y., Mendez, J., Ranganathan, N., Beranger, A.S. (1999). Fatigue life assessment of nodular cast iron containing casting defects. *Fatigue & Fracture of Engineering Materials & Structures*, vol. 22, no. 4, p. 289-300, **DOI:10.1046/j.1460-2695.1999.00162.x**.

Strojniški vestnik - Journal of Mechanical Engineering 64(2018)6, 383-392

DOI:10.5545/sv-jme.2017.5123
Original Scientific Paper
Received for review: 2017-12-01
Received revised form: 2018-03-29
Accepted for publication: 2018-04-26

Pneumatic Muscle Actuated Wrist Rehabilitation Equipment Based on the Fin Ray Principle

Ioana Petre – Andrea Deaconescu – Flavius Sârbu – Tudor Deaconescu*
Transylvania University of Brasov, Romania

Rehabilitation of the hand entails the deployment of equipment that, by motion, accelerates the regaining of its specific functions and allow the swift social reintegration of patients at a minimum cost. In this context, the paper presents and discusses a pneumatic muscle actuated piece of equipment that allows the simultaneous rehabilitation of the radiocarpal, metacarpophalangeal and interphalangeal joints. The main novelty of this equipment consists in the solution selected for the support and mobilization of the hand; the construction put forward is based on a couple of bar mechanisms that form a Fin Ray type structure, specific to fish fins. The paper presents the constructive solution, the structure of the actuation system and the experimental results that highlight both the benefits and disadvantages of the proposed equipment. Of particular interest is the compliance of the system that contributes to its adaptability to the particular pain threshold of the patient.
Keywords: compliance, fin ray effect, pneumatic muscles, wrist rehabilitation equipment

Highlights
- *New bio-inspired wrist rehabilitation equipment is proposed.*
- *A fin ray type structure is designed to support and mobilize the palm.*
- *The structural diagram of the rehabilitation equipment, its construction, and its pneumatic control diagram are presented.*
- *Attaining the angular motion limits of the hand joints and the variation of the rehabilitation equipment compliance are both demonstrated.*

0 INTRODUCTION

The wrist is an extremely complex joint, and its integrity is essential for everyday activity. The basic skeleton of the palm and the fingers includes 27 bones, eight of which (the carpal bones) form the most complex joint of the human body – the wrist. The actual hand consists of the five metacarpal bones followed by the 14 phalanges of the fingers.

While the wrist ensures a wide range of motions in flexion, extension, circumduction, radial and ulnar deviation, its complexity renders it vulnerable to a series of affections likely to limit its functionality. Lesions of the wrist can be the cause of problems in the long term, ranging from articular stiffness, pain, numbness to partial or total disability.

Rehabilitation by mobilization of the wrist has to commence as soon as physically possible, and the risk of relapse has been diminished significantly. The mobilization of the joints aims at correcting the retractions of the soft tissue, improvement of blood circulation, recovery of the gripping function, increase of muscle force and strength.

Wrist rehabilitation can be achieved by a procedure known as continuous passive motion that entails setting the injured joint into motion by mechanized means, without straining the patient's muscles. This is possible by means of specially designed equipment, capable of applying the optimum rehabilitation motions to the wrist.

As its primary control parameters, passive mobilization has the applied force, the stroke, the velocity, acceleration, duration and frequency of the displacement; all these quantities need to be adapted to the patient's clinical state and the set target. This means that equipment for passive mobilization has to allow the adjustment between certain limits of all the mentioned parameters.

Equipment based on continuous passive motion currently available on the marketplace provides in addition to mobilizing the damaged joint also an assessment of muscle performance, thus allowing patient state monitoring during the entire period of recovery.

Of the various manoeuvres possible as part of the mobilization exercises, slow progressive motion at varying amplitudes is most often applied. The force applied by the physical therapist at the maximum possible amplitude is typically dosed depending on the onset of pain, but also according to the therapist's experience with patients displaying either very high or very low pain thresholds.

The necessity of rehabilitation of the human body joints by mobilization was documented as early as nearly 5000 years ago. Chinese documents, 4700 years old, held information about therapeutic postures and motions aimed at pain relief [1]. It was

*Corr. Author's Address: Transilvania University, 29 Eroilor Bd., Brasov, Romania, tdeacon@unitbv.ro

in ancient Greece where the fundamentals of kinetic therapy were truly laid by Aristoteles, considered its founder. Later it was Hippocrates who noticed that motion contributes to regaining muscle force, while immobilization leads to atrophy.

The utilization of wrist rehabilitation equipment has been a usual practice for centuries. One of the oldest achievements are the mechanical devices of Zander based on the pulley and weight mechanism built in 1857 [2]. In 1919, the Otto Bock Company put forward a series of rehabilitation devices designed for all joints of the upper and lower limbs [3]. At present several manufacturers of such equipment are present on the marketplace, like Kinetek, producer of Kinetec Maestra Hand & Wrist CPM [4], Remington Medical marketing the WaveFlex Hand [5] or Kinex with its Kinex Hand [6].

Of interest in the recovery of the wrist is also the system with three degrees of freedom that can be attached to the MIT-MANUS robot [7]. The limits of motion of this equipment are flexion/extension 60°/60°, abduction/adduction 30°/45°, pronation/supination 70°/70°.

Paper [8] presents a novel lightweight hand exoskeleton robot, which is called an advanced service robots (ASR) glove. The study shows that the proposed system can flex and extend fingers in their range of motion and grasp objects efficiently.

The vast majority of rehabilitation equipment for continuous passive motion available on the marketplace at present is actuated by electric motors [9]. An analysis of the actuation systems of wrist rehabilitation equipment has revealed that about 72 % are electrically driven, 20 % pneumatically, 5 % hydraulically, and the remaining 3 % is covered by other energy sources [10].

At present, given the diversification, miniaturization and significant improvement of pneumatic components, the deployment of compressed air increasingly becomes a solution to be considered. Thus, in recent years. pneumatically actuated wrist rehabilitation equipment has been the object of several patents, a number of which are presented in [11] to [13]. Another example of pneumatically driven rehabilitation equipment is the parallel manipulator suitable for the complex motion of the human wrist joint [14].

A study of wrist rehabilitation equipment currently available on the marketplace has revealed that mobilization is achieved separately for each joint. It could also be observed that most equipment is actuated electrically, and pneumatic drives are neglected. Consequently, the authors of this paper put forward innovative equipment that mobilizes the wrist and finger joints at the same time, the actuation being ensured by a pneumatic muscle. Another novel aspect of the proposed solution is the bio-inspired construction of the palm support, based on the fin-ray effect, specific to fish fins. The benefit of the solution put forward consists in the fact that the complex motion performed by each of the hand segments, even though not all are affected, helps to improve their muscle and articular tone. Thus, in addition to the prophylaxis of joint pain achieved by the proposed equipment, it also helps to maintain and/or increase the muscle excitability of the healthy segments.

The first part of the paper presents the biomechanics of the hand and fingers, highlighting the limits of the motions that have to be reached by the rehabilitation equipment. Furthermore, the actuation motor is presented, with a focus on a specific property of pneumatic muscles known as compliance. The second part describes the construction of the rehabilitation equipment and its actuation, followed by the third part in which the experimental results are presented. The paper concludes with a section of conclusions.

1 DESIGN REQUIREMENTS

The development of rehabilitation equipment for the hand joints entails a thorough knowledge of the motions of the hand, of the forces and couples developed by it. It is further essential to identify the limits of these motions so that the new equipment can achieve them. With respect to this, the anatomic principles of the motions carried out by the joints of the hand are presented further on.

1.1 Biomechanics of the Joints of the Hand

The possible motions of the joints of the hand are incredibly numerous and complex. A rehabilitation device capable of conducting all these motions would require extremely complicated kinematics and would be economically inefficient. For this reason, rehabilitation equipment available on the marketplace at present is typically designed for a single joint, for either the wrist or the finger joints. The proposed rehabilitation system discussed in this paper achieves mobilization by the continuous passive motion of the radiocarpal joint and at the same time of the metacarpophalangeal and interphalangeal joints. The proposed equipment can reproduce in the case of all mentioned joints the motions of flexion-extension (Fig. 1).

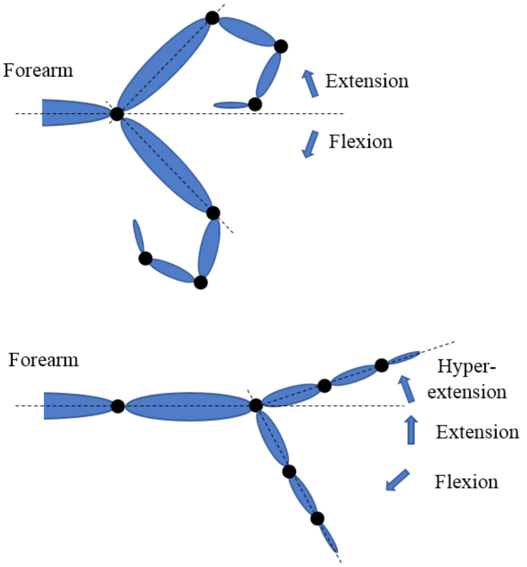

Fig. 1. *Flexion/extension of the wrist and joints of the fingers*

The flexion of the wrist or the palmar flexion is obtained by rotating the palm in the volar direction. Zero position is obtained when the forearm is in flexion at 90º and in pronation. In this case, the maximum rotation angle is of 80º. The extension of the wrist or dorsiflexion is obtained by rotating the palm in a dorsal direction, the maximum rotation angle being of 70º.

In the case of the fingers, zero position is considered for the extended palm and fingers. For the metacarpophalangeal joints, the angle of flexion increases from finger II to finger V from 90º to 100º. The extension of the fingers varies from one individual to another and ranges from 0º to 90º, the latter value describing hyperextension of the fingers.

Proximal flexion is the movement of the middle phalanx towards the inner palm, towards the proximal phalanx, until the limit of the motion is reached. The amplitude of this motion is of 100º to 120º. This flexion has small values for fingers I and II and greater ones for fingers IV and V.

Distal flexion is the motion of the distal phalanx towards the inner palm, towards the middle phalanx. To obtain the maximum value, the proximal joint has to be in flexion. The maximum flexion value of this joint does not exceed 90º.

The extension is possible only in the distal joints, its maximum amplitude being of 20º, and is encountered only in certain individuals. A larger extension angle causes the so-called hyperextension.

Fig. 2 illustrates the main joints of the hands, of interest for the present study.

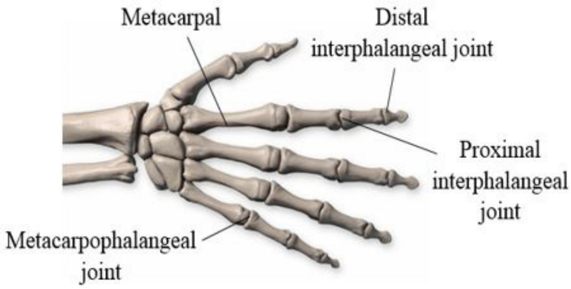

Fig. 2. *Joints of hand*

1.2 Requirements of the Novel Rehabilitation Equipment

The study conducted on hand rehabilitation equipment available on the marketplace has revealed specific characteristics of motions carried out by these, the values of which are given in Table 1.

Table 1. *Limits of the motions carried out by rehabilitation equipment of the wrist and fingers*

Joint		Motion	Rotation angle [º]	Rotation speed [º/min]
Wrist		Flexion	0 to 80	30 to 180
		Extension	0 to 70	
Joints of the fingers	Metacarpo-phalangeal	Flexion	0 to 90	55 to 440
		Extension	0 to 90	
	Proximal	Flexion	0 to 120	
	Distal	Flexion	0 to 90	
		Extension	0 to 90	

In addition to the possibility of conducting the recovery motions within the limits resulting from studying the biomechanics of the joints of the hand, such rehabilitation equipment needs to satisfy requirements including:

- compact construction and reduced weight such as to render the equipment portable to the patient (in the rehabilitation clinic or even at the patient's home). The portability of the entire rehabilitation system is assured by its construction, including the actual equipment (of dimensions 500 mm × 300 mm × 250 mm and approximately 3 kg mass) and the compressor (of dimensions 310 mm × 150 mm × 370 mm and 2.5 kg mass);
- reduced activation time, entailing only the duration of placing the equipment on a table and connecting it to the electrical source;
- utilization for its construction of robust, easy-maintenance components, typically manufactured from aluminium;
- easy control and user-friendly interface. This facility requires only minimum operation

proficiency of the user, given the easy command of the rehabilitation motions;
- adaptive behaviour to the pain threshold of the person undergoing rehabilitation treatment.

The latter requirement is achieved by using so-called adjustable compliance actuators (ACAs) for driving the equipment. A motor of this kind is selected given its benefits, such as its capacity of minimizing mechanical shocks, safe interaction with people or the ability to store and release energy in/from its passive-type elastic elements.

The utilization of adjustable compliance motors can ensure the adaptability of the rehabilitation equipment to a given concrete working situation determined by the patient's pain threshold, which in some cases may be different than initially envisaged. If the recovery motion is opposed by a force generated, for example, by the increased rigidity of the joint to be rehabilitated, and implicitly by the pain felt by the patient, the pneumatic muscle will absorb (due to air compressibility) the induced shock, without forcing the movement.

2 CONSTRUCTION OF THE REHABILITATION EQUIPMENT

2.1 Constructive Principle

Starting from the observation that maximum flexion of the wrist is obtained when flexion of the fingers is simultaneously induced, and the maximum extension of the wrist is achieved with the fingers being extended, the idea underlying the development of the novel rehabilitation equipment was bio-inspired, based on the Fin Ray effect, specific to fish fins. A pneumatic muscle was used as the motion generator element.

Fish can move with the help of their fins, which ensure stability and propulsion. Similarities were observed between the movement of the palm and the fingers and the movement of fish fins, as the flexion-extension of the palm is similar to the oscillatory movement of the tail fin of fish (Fig. 3). In both cases, the bone structure is set into motion by antagonistic pairs of muscles located on each side of the skeleton.

There are, nevertheless, differences between the movements of the palm and of the fishtail that need consideration when designing the construction of the palm rehabilitation equipment. One of these is the fact that the fishtails move symmetrically in relation to its relaxed resting position, while in the case of the palm and of the fingers the angles of flexion and extension, respectively, have different values; therefore, the movements of the fingers are not symmetrical in relation to the resting position. Another difference is connected to the movement amplitude of the fingers that is greater than that of the fishtail tip [15].

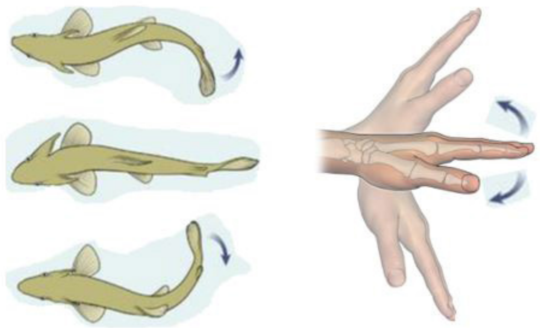

Fig. 3. *Movements of the fishtail and of the palm*

Fish fins are elastic structures built around thin bone fibres forming an assembly that generates the Fin Ray effect. A mechanical Fin Ray effect-generating structure is obtained by several series-linked bar mechanisms. For the mechanism to operate similarly to a fin, the component mechanisms need to be arranged in a pyramid structure.

These considerations underpinned the conceived rehabilitation equipment. Fig. 4 shows its structure next to that of a hand [16].

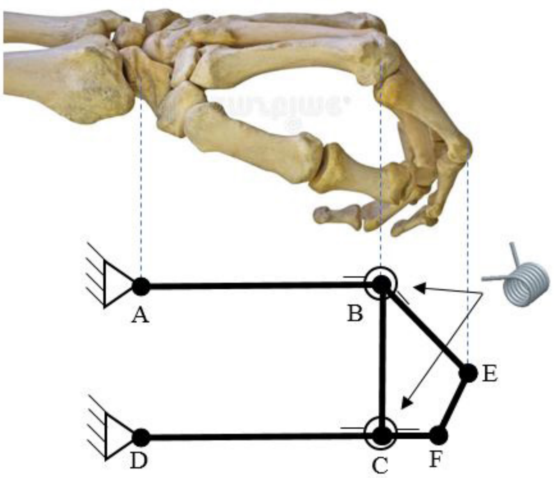

Fig. 4. *Structural diagram of the developed equipment*

The assembly designed to support and mobilize the palm consists of two series-linked bar mechanisms forming a fin ray-type structure. The length of lever AB is given by the distance between the wrist and the metacarpophalangeal joints, while distance BE represents the length between the metacarpophalangeal and the proximal joints. Each of joints B and C that link the two bar mechanisms includes a torsion spring with a 270° angle between its arms; the role of these springs is to cancel a degree of mobility of the entire assembly. For this system, the maximum flexion of the palm is obtained for extended fingers, and maximum palm extension is achieved when flexion of the fingers is induced. Fig. 5 shows the positions of the hand on the mechanism for the maximum flexion and maximum extension of the wrist, respectively.

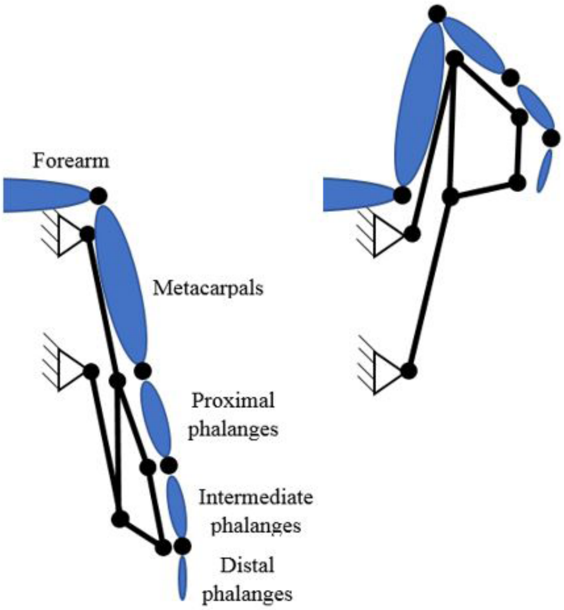

Fig. 5. *Limit positions of the mechanism*

The first bar mechanism (ABCD) ensures the rotation of the palm. The counter-clockwise rotation of lever AB causes the extension of the palm, namely its lifting. At the same time, the second bar mechanism (BCFE) responsible for the movement of the finger joints will rotate clockwise. Thus, the counter-clockwise rotation of the palm will cause it to make a fist, while the clockwise rotation will open it. It can be noticed that this equipment provides (as an innovation) the simultaneous motion of the palm and finger joints, ensuring mobilization of several muscle sets at the same time.

The degree of mobility of this mechanism, not considering the two torsion springs, is given by Eq. (1):

$$M = \varkappa^{e} \cdot n - \sum_{i=1}^{k} (\varkappa^{e} - f^{e}) = 3 \cdot 6 - 8 \cdot (3-1) = 2, \quad (1)$$

where $\varkappa^e$ is the dimension of the actual kinematic space, n the number of mobile elements, k the number of couples, f^e the dimension of the space of relative velocities for couple k.

Introducing the two springs linking element AB to BE and DC to CF, respectively, cancels a degree of mobility of the mechanism, as the movement of element BE becomes dependent on the movement of element AB. For bar mechanism BCFE to function correctly, the torsion springs mounted in couples B and C have to be twisted, thus tensioned over the entire working interval of this mechanism.

The equipment for the rehabilitation of the hand joints includes two Fin Ray type mechanisms positioned in parallel and linked rigidly one to another, in order to create the necessary width for the positioning of the hand. The rehabilitation equipment is set into motion by joint A, by means of a pinion-rack mechanism with a pneumatic muscle acting as a linear motor that drives the rack to conduct a linear reciprocating motion. The pneumatic muscle is fed compressed air at its fixed end, while its mobile end is linked to the rack. Fig. 6 shows a photographic image if this rehabilitation equipment.

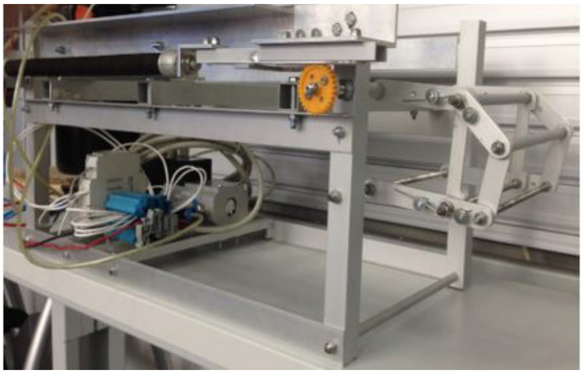

Fig. 6. *Construction of the rehabilitation equipment*

The pneumatic muscle contracts upon being fed compressed air and thus provides the required motor force. In this respect, in order to achieve the whole angle required for rotating the wrist in flexion/extension, the inferior position of the mechanism is ensured by the muscle in relaxed state (not charged with compressed air), while its superior position can be obtained by the contraction of the muscle (at maximum feed pressure).

A kinematic analysis of the rehabilitation equipment was achieved by means of the Mechanism modules of Pro/Engineer software. This analysis yielded the theoretical limits of the movements achievable by the rehabilitation equipment, featured in Table 2.

It needs to be pointed out that the proposed rehabilitation equipment ensures the achievement of the movement limits required for the flexion and extension of the hand joints. Obtaining the different values of the flexion/extension angles is achieved by controlling the stroke of the pneumatic muscles, i.e. by feeding it compressed air at various pressures.

Table 2. *Limits of the movements achievable by the rehabilitation system*

	Wrist [°]		Metacarpo-phalangeal joints [°]	
	Flexion	Extension	Flexion	Extension
Literature	80	70	90 to 100	0 to 0
Equipment	80	70	90	9.67

2.2 Actuation of the Rehabilitation Equipment

The dimensions of the pneumatic muscle utilized for the construction of the rehabilitation equipment were obtained upon conducting kinematic and dynamic calculations that yielded the magnitude of the required strokes and forces. Following these calculations, a DMSP-10-300N pneumatic muscle made by Festo was selected, ensuring a maximum displacement of 60 mm and the development of a required minimum force of 35 N.

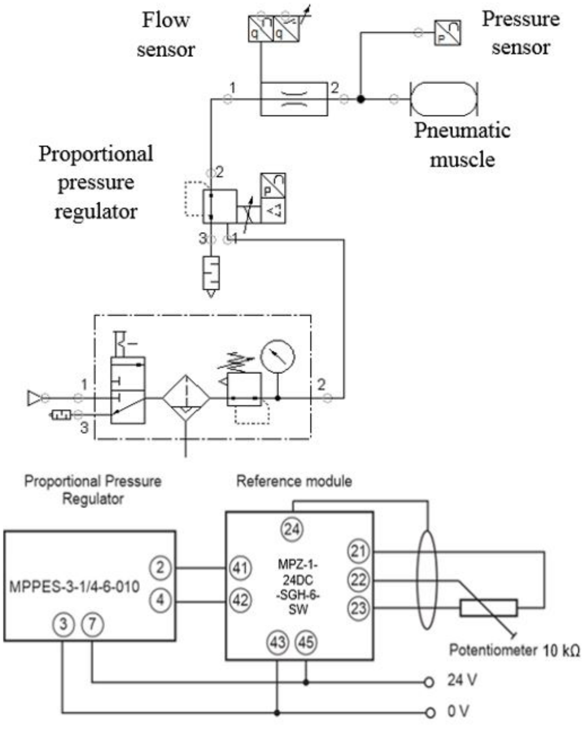

Fig. 7. *Control of the rehabilitation equipment by means of a proportional pressure regulator*

Fig. 7 shows the pneumatic actuation diagram of the rehabilitation equipment.

The compressed air reaches the pneumatic muscle by means of a proportional pressure regulator (MPPES-3-1/4-6-010), controlled by a reference module MPZ-1-24DC-SGH-6-SW (all made by Festo, Germany). By means of rotational potentiometers, the reference module can generate up to six different values of the reference voltage, which are transmitted in the form of signals to the proportional regulator. If none of these reference values is used, the signal transmitted to the pressure regulator is a voltage adjustable via an external potentiometer. The continuous adjustment of the air pressure allows for modifying the compliance of the entire system.

3 EXPERIMENTAL RESULTS

The first category of measurements was aimed at establishing a correlation between the values of the extension and flexion angles of the wrist achievable by the double bar mechanism and the feed pressure of the pneumatic muscle. For this, an E6A2-CS5C Omron rotary encoder was mounted on the axis of joint A. The horizontal line through joint A is considered the basis for measuring the angle of rotation. The angles for that support AB is above the horizontal axis are considered positive values (extension), while the negative values correspond to the position of support AB beneath the horizontal (flexion) (Fig. 8).

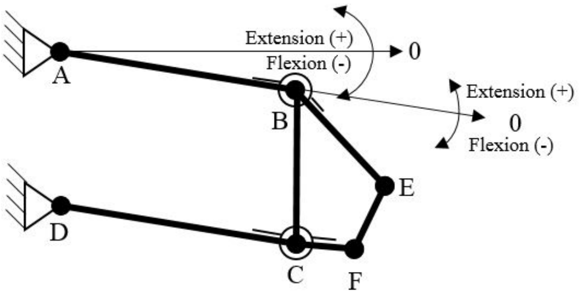

Fig. 8. *Convention of signs for the flexion and extension angles*

The measured data points were obtained by continuously charging the pneumatic muscle with air at a pressure increasing from 0 bar to 6 bar. Upon reaching this level, the rotation angle was also measured for reducing the pressure from 6 bar to 0 bar. Table 3 features the measured values, and Fig. 9 shows the corresponding graph.

The obtained experimental results revealed certain deviations of the limit angle magnitudes from those obtained theoretically (the data in Table 2).

Thus, in the case of maximum flexion the deviation is of 1.8° at the beginning of muscle contraction, while in the case of maximum extension the deviation is of 2.7°. These deviations are explained by the effect of the two torsion springs that prevent reaching the ends of the stroke. In the absence of these springs, the mechanism achieves the limits found in the theoretical study. Another conclusion concerns the occurrence of hysteresis, caused mainly by the pneumatic muscle but also by the torsion springs.

Table 3. *Variation of the flexion/extension angles versus the feeding pressure of the pneumatic muscle*

Pressure [bar]	0	1	2	3	4	5	6
Rotation angle [°]	–78.2	–64.7	–49.8	–25.0	7.1	35.0	67.3
Pressure [bar]	6	5	4	3	2	1	0
Rotation angle [°]	67.3	57.2	45.7	21.3	–18.0	–49.0	–74.8

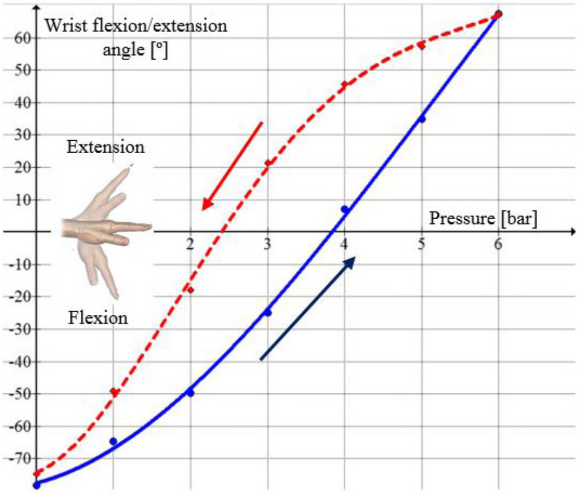

Fig. 9. *The flexion/extension angle of the wrist versus pressure*

The main constructive element of Festo pneumatic muscles is a flexible tube made from chloroprene covered by a sealed envelope made from inelastic aramid fibres displayed in diamond patterns forming a 3D-mesh. The hysteresis of the pneumatic muscles is caused by the deformation of the flexible tube, but also by the internal friction between each aramid fibre and the elastic material enveloping it. The hysteresis of the pneumatic muscles increases the non-linearity of the rehabilitation equipment and consequently the complexity of the required control system.

Further experimental research was aimed at establishing the link between the magnitude of the flexion/extension angle of the metacarpophalangeal joints (the angle between the extension of lever AB and BE) and the feed pressure of the pneumatic muscle. This angle was measured with a second rotary encoder, similar to the first one, placed in the axis of joint B. In this case the basis considered for the measurement was the axis of lever AB; the extension angles were considered positive and the flexion angles negative. The obtained results (Table 4 and Fig. 10) reveal the real maximum limits of the flexion and extension angles achievable on this equipment (maximum flexion of -87.6º and maximum extension of 8.3º).

Table 4. *Variation of the flexion/extension angles of the metacarpophalangeal joints versus the feed pressure of the pneumatic muscle*

Pressure [bar]	0	1	2	3	4	5	6
Rotation angle [°]	8.3	-13.7	-26.6	-39.4	-50.9	-68	-87.6
Pressure [bar]	6	5	4	3	2	1	0
Rotation angle [°]	-87.6	-78.5	-68.2	-47.9	-30.2	-16	7.1

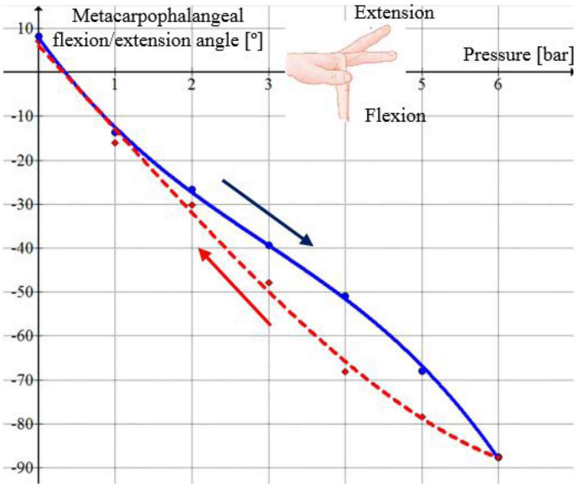

Fig. 10. *The flexion/extension angle of the metacarpophalangeal joint versus pressure*

The deviations in relation to the theoretical values shown in Table 2 are determined by the presence of the torsion springs, namely the same causes that prevented the attaining of the theoretical limits of the wrist rotation angle. In this case, the occurrence of hysteresis can also be noticed, caused by the behaviour of the pneumatic muscle.

Another set of experiments was aimed at proving the compliance of the rehabilitation equipment. When the dependency between the force generated by a motor and the displacement caused by it is of a non-linear type, the stiffness of the actuator and implicitly its compliance are variable. This is the case of the pneumatic muscle that actuates the rehabilitation equipment.

In order to determine the compliance of the rehabilitation equipment, the forces must be measured, developed by the pneumatic muscles in order to attain the various angular positions of the palm support. Measurements were conducted by means of a force sensor supplied by Festo, with the following characteristics: measuring range: 0 kN to 1 kN; supply voltage: 24 V DC; output voltage: 0 V to 10 V. The data provided by the sensor were processed by means of dedicated software FluidLab®-P V1.0, developed for the collection and processing of pneumatic system data.

Considering a maximum force of 15 N given by the weight of the hand and of the mechanical elements of the mechanism that need to be rotated, and knowing the dimensions of the components of the actuation mechanism, the variation of the force required for the actuation of the mechanism is described by Eq. (2):

$$F = G \cdot \frac{l}{r} \cdot \cos\alpha = 15 \cdot \frac{35}{15} \cdot \cos\alpha = 35 \cdot \cos\alpha, \qquad (2)$$

where the notations are: G is weight of the mobile assembly, l distance from joint A to the application point of force G, r radius of the pinion pitch circle and α the flexion/extension angle of the wrist. Fig. 11 shows the graph corresponding to this equation.

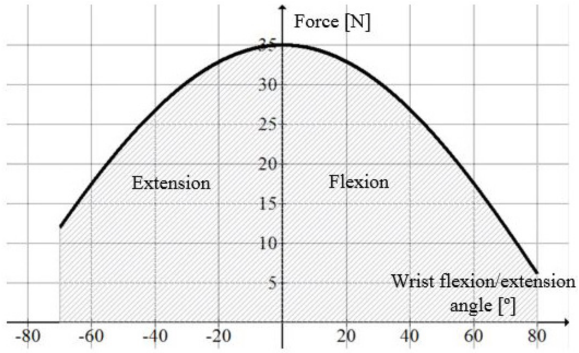

Fig. 11. *Dependency of the required force to be generated by the pneumatic muscle vs the flexion/extension angle of the wrist*

From Eq. (2) and Fig. 11 result the necessary values of the strokes and forces to be developed by the pneumatic muscle to ensure various angular positions of the palm support (Table 5).

Table 6 features the measurement results of the forces developed by the pneumatic muscle, and Fig. 12 shows a comparison of the necessary and the achieved forces of the rehabilitation equipment.

Table 5. *Required force of the pneumatic muscle*

α [°]	80	50	20	-10	-40	-70
Stroke s [mm]	0	5	10	15	20	25
F [N]	6.1	22.5	32.89	34.46	26.82	11.99

Table 6. *The force developed by the pneumatic muscle*

Pressure [bar]	0	1	2	3	4	5	6
Stroke of the rack [mm]	0	4.1	8.3	12.5	16.6	20.8	25
Force developed by the muscle [N]	0	26.9	64.8	106.3	147.5	185.8	219.9

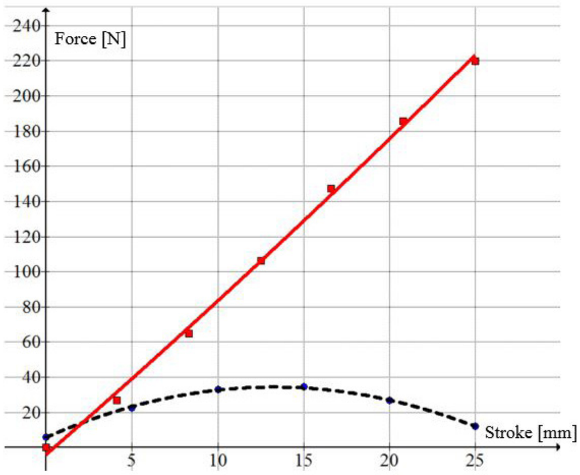

Fig. 12. *Dependency of the force developed by the pneumatic muscle on its stroke*

From the graph, it can be observed that at the beginning of the lifting motion of the hand (counter-clockwise rotation), the force developed by the muscle is smaller than required. This entails a delay of the motion until sufficient air pressure is reached such as to overcome this inconvenience. Nevertheless, this time lag of the rotation in relation to the starting time of feeding the pneumatic muscle with compressed air does not influence the efficiency of the rehabilitation exercise.

The regression function corresponding to the curve that describes the evolution of the force developed by the pneumatic muscle is:

$$F = 0.0233 \cdot s^2 + 8.5 \cdot s - 3.969. \qquad (3)$$

The correlation coefficient attached to this equation is of 0.998, which indicates that the proposed function describes the studied phenomenon with excellent precision.

The stiffness of the analysed system (k) is calculated by Eq. (4), and its inverse, compliance (C), by Eq. (5):

$$k = -\frac{dF}{ds} = -0.0466 \cdot s - 8.5, \tag{4}$$

$$C = k^{-1} = \frac{1}{-0.0466 \cdot s - 8.5}, \tag{5}$$

where s denotes the magnitude of the axial contraction of the pneumatic muscle as it is fed compressed air.

Figs. 13 and 14 show the variation of the rehabilitation equipment stiffness and its compliance, respectively, as the pneumatic muscle shortens axially upon being fed compressed air.

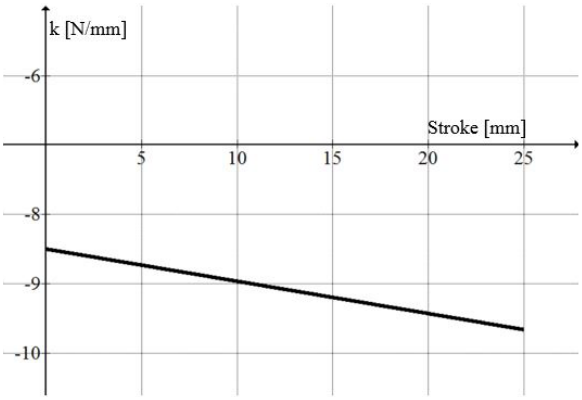

Fig. 13. *Stiffness of the rehabilitation equipment*

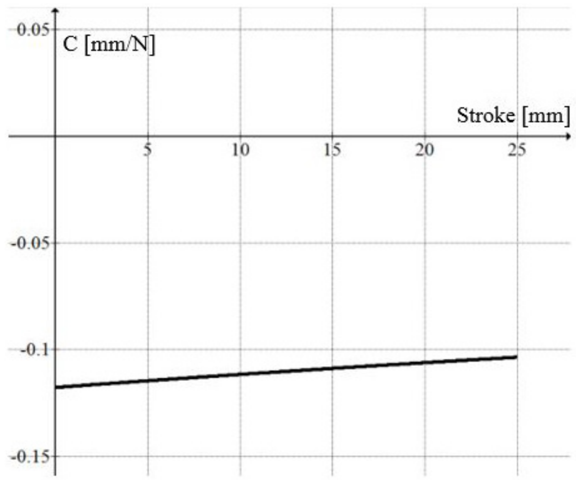

Fig. 14. *Compliance of the rehabilitation equipment*

The rehabilitation equipment proposed in this paper is characterized as visible in Figs. 13 and 14 by linearly decreasing stiffness and increasing compliance, as the stroke of the pneumatic muscle advances and the pressure grows. Consequences of such evolution of stiffness and compliance are a greater response time of the system to load variations, and evidently lesser precision, an aspect however of no significance to the efficiency of the rehabilitation exercises of the joints of the hand. On the other handin cases of rehabilitation exercises of the joints of the hand according to their degree of mobility, a compliant system like the one presented in this paper provides the benefit of adaptive behaviour to the concrete situation, allowing mobilization without causing pain to the patient.

4 CONCLUSIONS

This paper presents a piece of pneumatic muscle actuated wrist rehabilitation equipment. Its novelty consists in the assembly developed for supporting and mobilizing the hand, based on two bar mechanisms that form a fin ray-type structure, specific to fish fins. A further innovative element is the utilization of a pneumatic muscle as the actuation motor of the proposed system.

The conducted theoretical and experimental research has shown that the rehabilitation equipment ensures flexion and extension of the radiocarpal, metacarpophalangeal and interphalangeal joints that attain the angular limits of a healthy hand.

Mobilization by means of a pneumatic muscle benefits from the compliance of the rehabilitation equipment, which contributes to the adaptability of the studied system to the individual concrete pain threshold of the patient. The disadvantage of using pneumatic muscles as actuators is the occurrence of hysteresis that diminishes the positioning accuracy of the mechanical assembly designed for the mobilization of the joints. Taking into consideration, however, that, in the case of rehabilitation of the hand joints, patient comfort takes precedence over positioning precision, the proposed and discussed equipment appears as a viable alternative to rehabilitation equipment available on the marketplace at present.

Upon completion of the research related to the prototype, the authors of the paper intend to move to clinical tests in view of improving the actuation system of the equipment.

5 REFERENCES

[1] Sbenghe, T. (2008). *Kinesiology - Movement Science*. Medical Publishing House, Bucharest.

[2] Moțet, D. (2010). *Physical Therapy Encyclopedia. vol. 2,* Semne Publishing House, Bucharest.

[3] Otto bock Group (2017). *from http://www.ottobock.com/en/*, accessed on 2017-08-15.

[4] Maestra (2017). Kinetec, from *http://kinetec.fr/en/kinetec-selection/cpm-continuous-passive-motion/attelle-kinetec-maestra-detail.html*, accessed on 2017-08-15.

[5] Waveflex Hand CPM (2017). Remington Medical, *from http://www.remingtonmedical.com/product/detail/A1*, accessed on 2017-08-15.

[6] Kinex Hand (2017). Kinex CPM Devices, *from https://www.kinexmedical.com/cpm-devices*, accessed on 2017-08-15.

[7] Krebs, H.I., Volpe, B.T., Williams, D., Celestino, J., Charles, S.K., Lynch, D., Hogan, N. (2007). Robot-aided neurorehabilitation: a robot for wrist rehabilitation. *IEEE Transactions on Neural Systems and Rehabilitation Engineering*, vol. 15, no. 3, p. 327-335, **DOI:10.1109/TNSRE.2007.903899**.

[8] Hadi, A., Alipour, K., Kazeminasab, S., Elahinia, M. (2017). ASR glove: A wearable glove for hand assistance and rehabilitation using shape memory alloys. *Journal of Intelligent Material Systems and Structures*, vol. 29, no. 8, p. 1575-1585, **DOI:10.1177/1045389X17742729**.

[9] Maciejasz, P., Eschweiler, J., Gerlach-Hahn, K., Jansen-Troy, A., Leonhardt, S. (2014). A survey on robotic devices for upper limb rehabilitation. *Journal of NeuroEngineering and Rehabilitation*, vol. 11, no.3, p. 1-29, **DOI:10.1186/1743-0003-11-3**.

[10] Gopura, R.A.R.C., Bandara, D.S.V., Kiguchi, K., Mann, G.K.I. (2016). Developments in hardware systems of active upper-limb exoskeleton robots: A review. *Robotics and Autonomous Systems*, vol. 75, p. 203-220, **DOI:10.1016/j.robot.2015.10.001**.

[11] Dongming, Y., Binrui, W., Yinglian, J. (2011). *Pneumatic Muscle Flexible Elbow Joint Device with Buffer Spring and Flexible Shaft Sleeve*. Patent CN202071080, China Institute of Metrology, Beijing.

[12] Canjun, Y., Jiafan, Z., Jie, Z., Ying, C. (2007). *Flexible Exoskeleton Elbow Joint Based on Pneumatic Power*. Patent CN200984250, China Institute of Metrology, Beijing..

[13] Zhang, J., Liu, Y., Jia, Y., Shen, Z. (2012). *Device for Hand Rehabilitation*. Patent WO2012120393, World Intellectual Property Organization, Geneva.

[14] Takaiwa, M., Noritsugu, T. (2005). Development of wrist rehabilitation equipment using pneumatic parallel manipulator. *Proceedings of IEEE International Conference on Robotics and Automation*, p. 2302-2307, **DOI:10.1109/ROBOT.2005.1570456**.

[15] Deaconescu, T., Deaconescu, A. (2016). Applications of pneumatic muscles developed within the Festo national fluid actuation and automation training centre in Braşov. *Recent Review*, vol. 17, no. 4(50), p. 540-547.

[16] Filip, O., Deaconescu, T. (2017). Mathematical modelling of a Fin Ray type mechanism, used in the case of the wrist rehabilitation equipment. *The 4th International Conference on Computing and Solutions in Manufacturing Engineering*, vol. 94, **DOI:10.1051/matecconf/20179401006**.

Strojniški vestnik - Journal of Mechanical Engineering 64(2018)6, 393-400

DOI:10.5545/sv-jme.2017.5189
Original Scientific Paper
Received for review: 2017-12-30
Received revised form: 2018-02-19
Accepted for publication: 2018-04-16

New Hybrid System of Machine Learning and Statistical Pattern Recognition for a 3D Visibility Network

Matej Babič[1,*] – Karolj Skala[2] – Dookhitram Kumar[3] – Roman Šturm[4]
[1] Jožef Stefan Institute, Ljubljana, Slovenia
[2] Ruđer Bošković Institute, Croatia
[3] University of Technology, Mauritius
[4] University of Ljubljana, Faculty of Mechanical Engineering, Slovenia

*Intelligent systems are an excellent tool to use for solving complex problems in the field of industrial applications. We use the mathematical method of fractal geometry and network theory when laser-hardening techniques are applied. The microstructure of the robot-laser-hardened specimens is very complex; however, we can present it by using a 3D visibility network. We convert the scanning electron microscope (SEM) images of the microstructure to a 3D graph and calculate the density of the visibility network of these 3D networks. We have analyzed the topographical properties of the hardened specimens by using the algorithm for the construction of a visibility network in a 3D space. We develop a new hybrid system of machine learning for predicting carbide content of the hardened specimens by using multiple regression, neural networks, and a genetic algorithm. We find the statistical significance of the relationship between attributes of the hardened specimens, the topological properties of visibility graphs, and carbide content of the hardened specimens.*_

Keywords: fractal geometry, hybrid system, laser hardened specimens, visibility network, statistical pattern recognition

Highlights
- *We have calculated the statistical properties of the data of the parameters of the hardened specimens.*
- *We have described the carbide content of the hardened specimens using the topological properties.*
- *We have presented a new intelligent hybrid system model to predict the carbide content of the hardened specimens.*
- *Our new method has many applications in pattern recognition, computer graphics, computational geometry, and so on.*

0 INTRODUCTION

Robot laser hardening [RLH] [1] is a heat treatment similar to inductive or conventional flame hardening. We can analyze the microstructures of RLH specimens using 3D visibility networks (graphs). A visibility network [2] is a graph of visible areas, which presents a set of nodes and obstacles in the Euclidean plane or space. Fractal geometry [3] was developed by Mandelbrot, who built the Mandelbrot set $y=z^2+c$ with the help of a computer. He provided a new approach in the scientific discipline as he set out and designed a new way of thinking about structures and shapes. The Hurst parameter H [4] is the correlation between random steps X_1 and X_2, which is followed by the time-to-time difference Δt. Hurst parameter occurs in many areas of applied mathematics, including fractals and chaos theory, and is used in many fields ranging from biophysics to network computers. The parameter was originally developed in hydrology. However, modern techniques to estimate the Hurst parameter H come from fractal mathematics. The fractal dimension has been used to measure the roughness of sea coasts. The relationship between the fractal dimension D and the Hurst parameter H is given by the equation $D=2-H$ for 2D objects and $D=3-H$ for 3D objects. We developed a new method to estimate the Hurst parameter H of a 3D object. In this paper, we introduce a new hybrid intelligent system to predict the carbide content of RLH specimens from the topological property of the density of the visibility network and fractal dimension.

1 PREPARATION OF MATERIAL SPECIMENS

The study was done on the standard tool steel labeled as DIN 1.7225 [5]. The tool steel was surface hardened by laser at different speeds and different powers. We use a robot laser cell RV60-40 (Reis Robotics Company). The maximum power of the robot-laser cell is 3000 W. We hardened specimens with an output power of 1500 W. Therefore, we modified the speed parameter $v \in [2, 5]$ mm/s and the temperature parameter $T \in [800, 2000]$ °C. Each sample was prepared by etching and polishing (IMT, Institute of Metals and Technology Ljubljana, Slovenia) for a microscope evaluation (IJS, Jozef Stefan Institute). Fig. 1 was made by field emission scanning electron microscopy, JMS-7600F, JEOL. We wanted to know whether the microstructure of the RLH fractal patterns found a structure from which the Hurst parameter H could be estimated. Fig. 2 presents a 3D graph of the

*Corr. Author's Address: Jožef Stefan Institute, Ljubljana, Slovenia, , babicster@gmail.com

microstructure of the RLH specimen. It is converted from Fig. 1 by using Fig. 1 color depth.

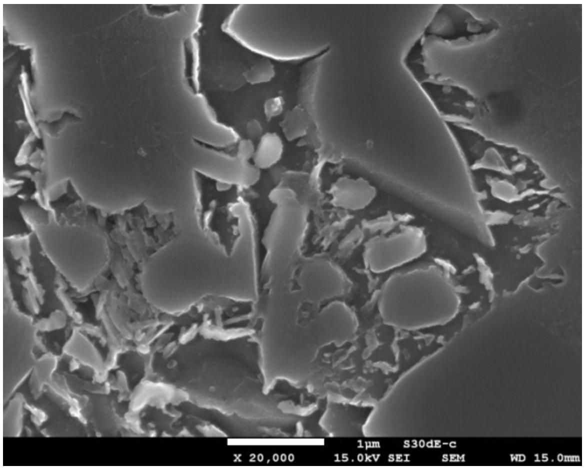

Fig. 1. *SEM picture of microstructure of the RLH specimen*

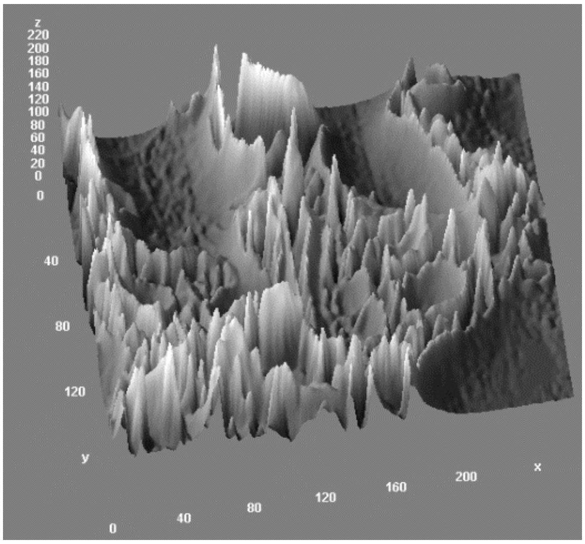

Fig. 2. *3D graph of microstructure of the RLH specimen*

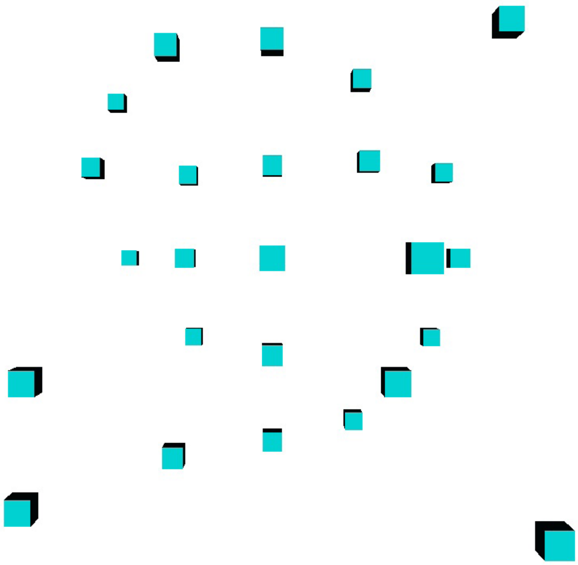

Fig. 3. *Vertices in a 3D graph*

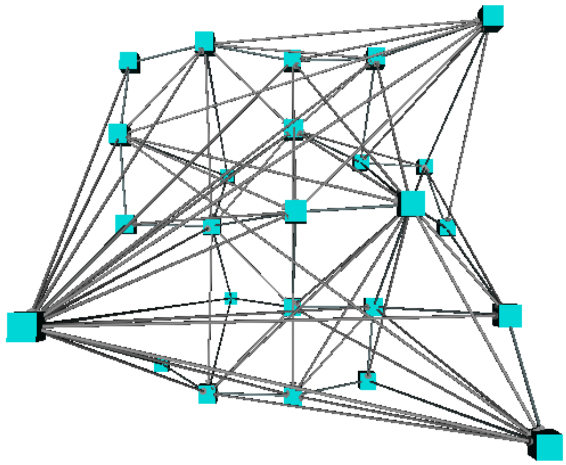

Fig. 4. Visibility network of vertices in a 3D graph

2 DESCRIPTION OF METHOD

We used fractal geometry and a visibility network to determine the complex microstructure of the RLH specimens.

Fig. 3 presents the random vertices of the 3D graph. For better visual presentation, we use 5×5 vertices of the 3D graph. 3D graph presents microstructure of the RLH specimens.

Babič et al. [6] present a solution for constructing a visibility network in a 3D space. Fig. 4 presents the results of the problem of constructing a visibility network in a 3D space. We use the statistical topological property of the density of the visibility network for pattern recognition from SEM images of the RLH specimens. The density q was calculated for each visibility network by Eq. (1):

$$q = \frac{2m}{n \times (n-1)}, \tag{1}$$

where m is the number of edges, n is the number of vertices in the visibility network.

We present a method of estimating the Hurst exponent H for 3D objects [7]. First, we use the program ImageJ to find all the coordinates (x, y, z) of the SEM picture. Secondly, we estimate the Hurst exponent H by using the z-coordinates, which present a long continuous graph (Fig. 5). Also, all points

(x_i, y_0, z_i) present a space component on a 2D graph for all points (x_i, z_i). All points (x_i, y_1, z_i) present a second space component on a 2D graph for all points (x_i, z_i). We made a space component for all y_i, $\forall i$. Then we combined all these space components into one space component. For this long space component, we can estimate the Hurst exponent H. We use the fractal dimension for pattern recognition from SEM images.

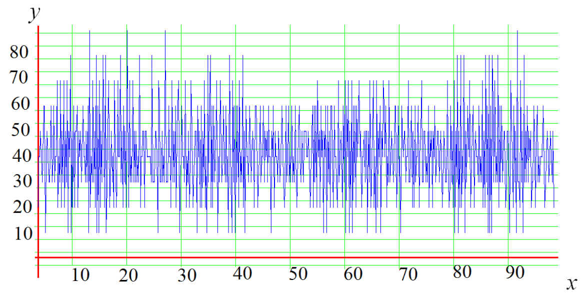

Fig. 5. *Long continuous graph*

We use the method of a visibility network and fractal geometry for statistical pattern recognition. To model the results, we use intelligent system methods, that is, multiple regression, neural network (NN), and genetic programming (GP).

NNs [8] have the ability to solve a variety of problems. The sophistication of NNs is primarily due to their ability to imitate the principle of the functioning of the biological brain, which means that they solve problems similarly to humans. We used the Neuralyst program to create a model with NNs. Neuralyst is a software tool used within Excel. It has the ability to model NNs. We used a multi-tasking neural system with backpropagation and no back links. We had the option of setting different attributes. Table 1 presents the attributes of the NNS.

Table 1. *Attributes of the NN*

Learning speed [-]	0.6
Inertial coefficient [-]	0.5
Test mass tolerance [-]	0.02
Tolerance of the learning set [-]	0.03
Number of layers [-]	4

Fig. 6 presents a general multi-layer NN system.

Table 2. *Attributes of the GP*

Size of the population of organisms	500
Maximum number of generations	100
Reproduction probability	0.4
Crossover probability	0.6
Maximum permissible depth in the creation of the population	6
Maximum permissible depth after the operation of crossover of two organisms	10
Smallest permissible depth of organisms in generating new organisms	2
Tournament size used for selection of organisms	7

Genetic programming [9] is similar to genetic algorithms and differs only in terms of the presentation method. Individual component in genetic algorithms is presented by a sequence of numbers, and the individual component in genetic programming is presented by a computer program. GP automatic writing of programs according to the nature of natural selection (evolution). At the beginning, we have some randomly written programs, which represent the initial

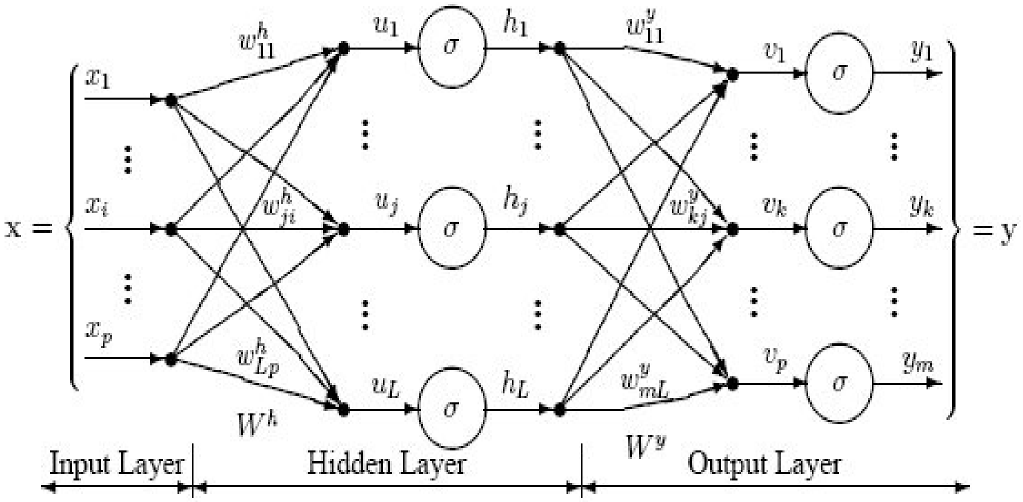

Fig. 6. *General multi-layer NN system*

population. Then by crossing and selection, we get the next generation. Table 2 presents the attributes of the genetic programming.

We used the genetic operations of reproduction and crossover. Fig. 7 presents an example of an organism in genetic programming.

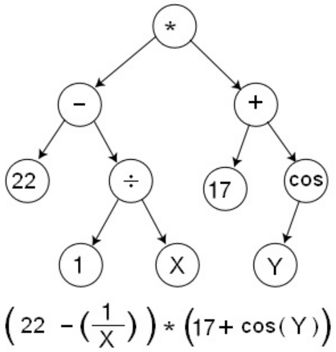

Fig. 7. *Organism in GP*

Multiple regression (MR) **[10]** is designed to investigate linear causes the relationship between a single dependent variable and one or more independent variables. With it, we determine the statistical feature in the power of connection and we predict the values of the dependent variable. The impact of each of the independent variables is estimated to be independent of the interactions between independent variables.

Hybrid evolutionary computation **[11]** is a generic, flexible, robust, and versatile method for solving complex global optimization problems and could be used in practical applications. We present a new intelligent hybrid systems model in Fig. 8. Data information is presented in Table 3.

Table. 3. *Attributes of the hardened specimens*

S	x_1	x_2	x_3	x_4	x_5	x_6	Y
S1	1000	2	1.91	2.30	0.191	85	39
S2	1000	3	1.96	2.26	0.224	85	45
S3	1000	4	1.95	2.26	0.210	85	43
S4	1000	5	1.94	2.34	0.235	85	41
S5	1400	2	1.92	2.22	0.246	85	36
S6	1400	3	1.98	2.39	0.228	85	49
S7	1400	4	1.95	2.25	0.201	85	45
S8	1400	5	1.98	2.29	0.215	85	48
S9	1000	2	1.97	2.18	0.247	39	46
S10	1000	3	1.86	2.18	0.232	45	32
S11	1000	4	1.98	2.41	0.219	43	45
S12	1000	5	1.94	2.21	0.241	41	42
S13	1400	2	1.98	2.26	0.225	36	28
S14	1400	3	1.58	2.27	0.238	49	19
S15	1400	4	1.97	2.43	0.208	45	41
S16	1400	5	1.81	2.29	0.197	48	38
S17	800	0	1.97	2.23	0.289	85	47
S18	1400	0	1.98	2.24	0.277	85	52
S19	2000	0	1.97	2.26	0.245	85	50
S20	950	0	1.96	2.28	0.217	85	66
S21	850	0	1.95	2.32	0.212	85	80
S22	0	0	1.91	2.30	0.195	85	39

3 RESULTS AND DISCUSSION

The attributes of the hardened specimens influence on the carbide content (Table 3). The specimens are labeled as S1 to S22. Attribute x_1 represents the temperature [°C] and x_2 represents the speed of RLH [mm/s]. Attributes x_3, x_4, and x_5 represent the keys for pattern recognition. Parameter x_3 represents the complexity in 2D, x_4 represents the complexity in 3D, x_5 represents the density of the visibility networks in a 3D space, and x_6 represents the carbides in specimens. The last attribute Y is the measured surface carbide

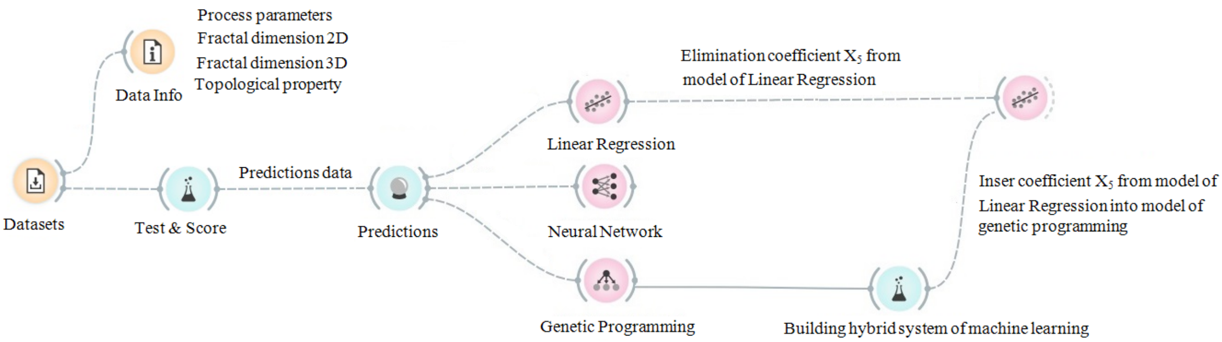

Fig. 8. *Intelligent system model and new hybrid intelligent system*

content of the RLH specimens. Specimen S22 presents the material before the RLH process. In Table 4, we denote measurement (M) data (D) by MD, prediction data obtained by MR, prediction data obtained by neural network (NN), prediction data obtained by GP, and prediction data obtained by the hybrid system by *H*. Specimen S14 has a minimal carbide content after hardening, that is, 19 %. Table 4 present the statistical properties of the experimental and predicted patterns. Table 5 present topological properties of 3D visibility network. The measured and predicted carbide content of the RLH specimens is presented in the Fig. 9. The MR model is presented by Eq. (1), GP model is presented by Eq. (2), and hybrid model is presented by Eq. (3). We calculated precision of the GP model, NN and of the MR model by calculating average of absolute difference between measured and predicted data divided by measured data. The GP model has 85.57 % precision, the NN has 90.57 % precision, MR has 80.87 % precision and hybrid system has 62.98 % precision.

Table 5 presents the topological properties of the 3D visibility network. Measured and predicted parts of carbides of the LHR specimens depend on attributes x_1, x_2, x_3, x_4, x_5 and x_6 are presented in Fig. 9. We use the statistical topological property of the visibility networks to describe the carbide content in the microstructures. Image analysis of the SEM images of the RLH specimens is an interesting approach. With MR, GP and NN, we predict the carbide content in the microstructures. Finally, we present a new hybrid system of intelligent systems. For measured and predicted parts of carbides of the LHR specimens data, we calculated Kendall correlation coefficient. The best results for prediction give us NN, because the Kendall correlation coefficient (0.021) is most close to experimental data (0.131). Table 3 presents the topological properties of the 3D visibility network and attributes of RLH specimens. In this way, we can see how the attributes of speed and temperature influence the topological structures of visibility graphs in 3D space. Table 6 presents the statistical properties of the topological properties of the extreme number, number of edges, and triadic census type 16 to 300 of the 3D visibility network for RLH specimens. Firstly, we calculated the basic statistical properties of the mean, standard deviation, standard error, median, geometric mean, and harmonic mean of the topological properties of visibility graphs in 3D space of RLH specimens. We found significant positive relationships between the kurtosis, Fisher's $G2$, the coefficient of variation, the coefficient of dispersion,

Table. 4. *Measured and predicted data*

S	*MD*	*MR*	*NN*	*GP*	*H*
S1	39	55.28	38.98	38.7	34.77
S2	45	50.93	44.53	45.0	37.32
S3	43	47.84	42.25	45.0	40.61
S4	41	45.89	42.27	41.4	44.78
S5	36	42.41	36.98	40.8	44.18
S6	49	49.69	48.32	44.3	43.32
S7	45	40.97	44.86	46.7	46.45
S8	48	40.00	48.06	44.6	48.86
S9	46	42.74	45.97	46.2	40.85
S10	32	35.98	32.08	18.8	47.98
S11	45	48.01	44.98	40.0	44.99
S12	42	33.04	42.26	42.0	55.08
S13	28	39.91	46.48	27.7	47.05
S14	19	19.88	18.99	22.8	67.35
S15	41	42.15	41.54	45.2	51.32
S16	38	27.23	37.08	38.0	60.50
S17	47	59.78	47.86	47.4	30.50
S18	52	50.58	50.11	49.7	39.58
S19	50	42.10	51.01	50.1	48.54
S20	66	62.98	66.65	47.5	28.93
S21	80	65.82	79.25	46.4	27.35
S22	39	79.59	84.60	84.9	58.25

Table. 5. *Topological properties of 3D visibility network*

S	Extreme number	Number of edges	Triadic census type 16 to 300
S1	120823	3500351	4865624
S2	125787	3308776	4191425
S3	123943	3335861	4267175
S4	124833	3355735	4353872
S5	124626	3314397	4212248
S6	131540	3190001	3796016
S7	126962	3311163	4196282
S8	130799	3173601	3741603
S9	123393	3355056	4256560
S10	126395	3386391	4483986
S11	124296	3315948	4207031
S12	123829	3355735	4353872
S13	128143	3451450	4862060
S14	122500	3685175	5877473
S15	120818	3338595	4199754
S16	116812	3733624	5848517
S17	133031	3178192	3774789
S18	130974	3182544	3819193
S19	131043	3170121	3746658
S20	95090	4151533	7284078
S21	106916	5653616	1764141
S22	86871	5735036	1466536

Model of multiple regression:

$$Y = -99.0509 - 0.0178 \times x_1 - 3.25717 \times x_2 + 46.65489 \times x_3 + 38.06208 \times x_4 - 63.3748 \times x_5 + 0.165097 \times x_6. \tag{2}$$

Model of genetic programming

$$\begin{aligned} Y = {} & 0.129654 \times (-x_6 - x_2^2 - \frac{x^2 + x_2^2 + x_6}{-x_2 + x_2 \times \left(-x_2 + x_2^2\right)} + \frac{x_6}{x_2 \times \left(-x_3 + \dfrac{x_6}{-x_3 + x_2^2}\right)} \\ & + \frac{1}{x_4} \times \left(\frac{x_6^2}{x_2 - x_1 + x_2^2 \times \left(x_2 + x_2 \times x_3\right) + x_6 - \dfrac{x_2 \times x_6 \times \left(x_6 + \dfrac{x_6}{x_3}\right)}{x_2 - x_1} - \dfrac{(x_3 \times (x_2 + x_3) + x_5) \times (x_3 + 2 \times x_3 \times (x_2 + x_3) + x_6))}{x_2 + x_1 - x_2^2}} \right) \\ & + \frac{1}{x_4} \times \left(\frac{x_6}{7.71283 + 2 \times x_2 - x_6 + \dfrac{x_6}{x_2^2 - x_3} + \dfrac{(x_2 + x_3 + x_6) \times \left(x_6 + \dfrac{x_6}{x_3}\right)}{x_2 - x_1}} \right) + \frac{x_2 \times x_3 + x_6}{x_4}. \end{aligned} \tag{3}$$

Hybrid model

$$\begin{aligned} & Y^2 + Y\left(A + B\right) + AB - C = 0, \\ & A = 0.129654 \left(-x_6 - x_2^2 + \frac{x_2 + x_2^2 + x_6}{-x_2 + x_2 \times \left(-x_2 + x_2^2\right)} + \frac{x_6}{x_2 \left(-x_3 + \dfrac{x_6}{-x_3 + x_2^2}\right)} \right), \\ & B = 99.0509 + 0.0178 x_1 + 3.25717 x_2 - 46.65489 x_3 + 63.3748 x_5 - 0.165097 x_6, \\ & C = x_2 x_3 + x_6 + \\ & \frac{x_6^2}{x_2 - x_1 + x_2^2\left(x_2 + x_2 x_3\right) + x_6 - \dfrac{x_6}{x_2^2 - x_3} + \dfrac{\left(x_3\left(x_2 + x_3\right) + x_6\right)\left(x_3 + 2x_3 \times \left(x_2 + x_3\right) + x_6\right)\right)}{x_2 + x_1 - x_2^2} - \dfrac{x_2 x_6 \left(x_6 + \dfrac{x_6}{x_3}\right)}{x_2 - x_1}} \\ & + \frac{x_6}{7.71283 + 2x_2 - x_6 + \dfrac{x_6}{x_2^2 - x_3} + \dfrac{\left(x_3 x_2 + x_6\right)\left(x_6 + \dfrac{x_6}{x_3}\right)}{x_2 - x_1}}. \end{aligned} \tag{4}$$

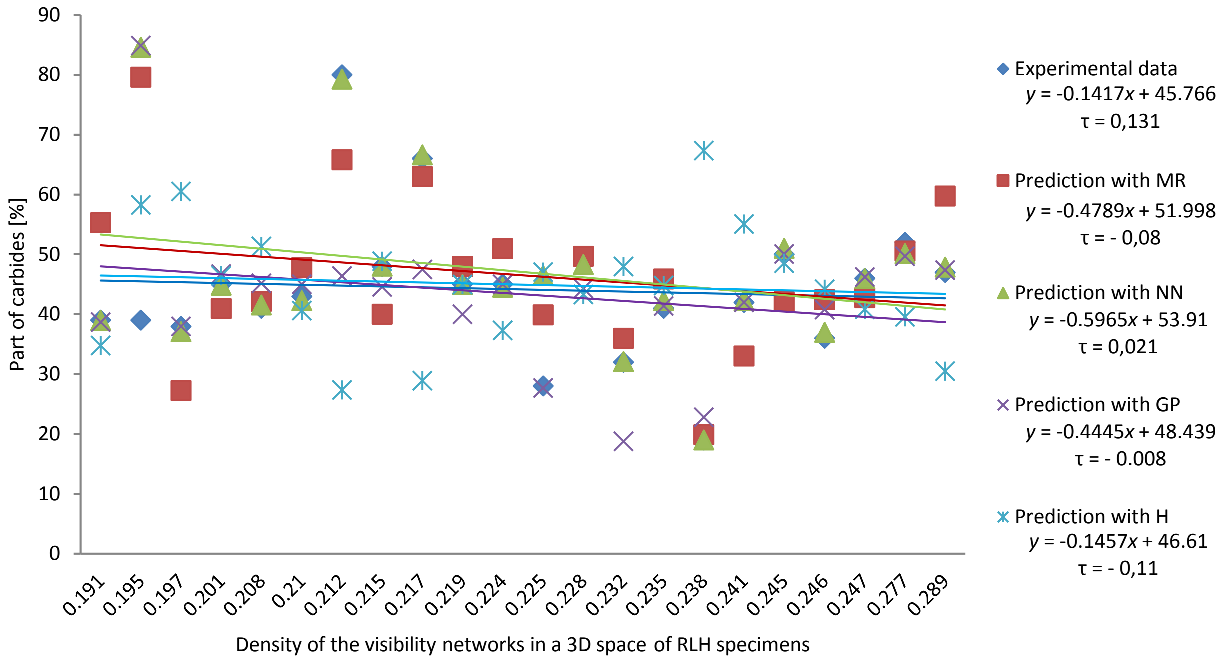

Fig. 9. *Measured and predicted carbide content of the LHR specimens depend on attributes x_1, x_2, x_3, x_4, x_5 and x_6*

and the topological properties of visibility graphs in 3D space of RLH specimens.

Table. 6. *Statistical properties of topological properties of 3D visibility network*

SP	Extreme number	Number of edges	Triadic census type 16 to 300
Mean	121792	3599223	4253132
Standard deviation	11531.35	714391.3	1201353
Standard error	2458.49	152308.8	256129.4
Median	124461	3346826	4209640
Geometric mean	121194	3546497	4055020
Harmonic mean	120509	3505535	3790200
Kurtosis	5.90	7.454659	4.719475
Fisher's *G2*	4.03	5.993685	2.517122
Coefficient of variation	0.094	0.1984849	0.2824632
Coefficient of dispersion	0.05	0.1024648	0.1701942

4 CONCLUSIONS

The paper presents a new method of constructing visibility networks in a 3D space, a new method of describing the complexity of 3D space, and a new hyper-hybrid system of machine learning for the use in mechanical engineering to predict the topographical properties of materials. The paper presents a method of using visibility graphs in 3D space and fractal geometry to analyze the complexity of RLH specimens. Analyzing the complexity of RLH surfaces is a very hard problem. This new method has many applications in pattern recognition, computer graphics, computational geometry, and so on. The main findings are:

1. We use the method of network theory and fractal geometry to analyse the microstructure.
2. For prediction of the carbide content of hardened specimens, we use intelligent system methods, namely a neural network, multiple regression, and a genetic algorithm. The best results for prediction give us neural network.
3. We present the new hybrid spiral sequences.
4. The paper introduces a new method of machine learning in metallurgy.
5. We find the statistical significance of the relationship between attributes of the hardened specimens and the experimental and predicted pattern data.
6. The paper compares three methods, namely multiple regression, neural network and genetic programming, with a hybrid system of intelligent systems.

5 REFERENCES

[1] Petrovič, S., D., Šturm, R. (2014). Fine-structured morphology of a silicon steel sheet after laser surface alloying of Sb powder. *Strojniški vestnik – Journal of Mechanical Engineering*, vol. 60, no. 1, p. 5-11, **DOI:10.5545/sv-jme.2013.1347**.

[2] Ghosh, S.K. (1997). On recognizing and characterizing visibility graphs of simple polygons. *Discrete & Computational Geometry*, vol. 17, no. 2, p. 143-162, **DOI:10.1007/BF02770871. ISSN 0179-5376**.

[3] Mandelbrot, B.B. (1983). *The Fractal Geometry of Nature*. W.H. Freeman & Co., San Francisco, **DOI:10.1119/1.13295**.

[4] Stoev, S., Pipiras, V., Taqqu, M.S. (2002). Estimation of the self-similarity parameter in linear fractional stable motion. *Signal Processing*, vol. 82, no. 12, p. 1873-1901, **DOI:10.1016/S0165-1684(02)00317-1**.

[5] Alta steel (2017). from *http://www.altaspecialsteel.com/DIN-1-7225-AISI-4140-38.html*, accessed on 2017-12-30.

[6] Babič, M., Hluchy, L., Krammer, P., Matovič, B., Kumar, R., Kovač, P. (2017). New method for constructing a visibility graph-network in 3D space and new hybrid system of modeling. *Journal of Computing and Informatics*, vol. 36, no. 5, p. 1107-1126, **DOI:10.4149/cai.2017.5.1107**.

[7] Babič, M., Kokol, P., Guid, N., Panjan, P. (2014). A new method for estimating the Hurst exponent H for 3D objects. *Materials and Technology*, vol. 48, no. 2, p. 203-208.

[8] Graves, A., Schmidhuber, J. (2009). Offline Handwriting Recognition with Multidimensional Recurrent Neural Networks, in Bengio, Y., Schuurmans, D.,; Lafferty, J., Williams, C.K.I., Culotta, A. (eds.). *Advances in Neural Information Processing Systems,* vol. 22, p. 545-552.

[9] Koza, J.R. (1992). *Genetic Programming: On the Programming of Computers by Means of Natural Selection*, MIT Press.

[10] Armstrong, J.S. (2012). Illusions in regression analysis. *International Journal of Forecasting*, vol. 28, no. 3, p. 689-694, **DOI:10.1016/j.ijforecast.2012.02.001**.

[11] Ravi, V., Naveen, N., Pandey, M. (2013). Hybrid classification and regression models via particle swarm optimization auto associative neural network based nonlinear PCA. *International Journal of Hybrid Intelligent Systems*, vol. 10, p. 137-149, **DOI:10.3233/HIS-130173**.

Strojniški vestnik - Journal of Mechanical Engineering 64(2018)6, 401-411

DOI:10.5545/sv-jme.2017.5085
Original Scientific Paper
Received for review: 2017-11-14
Received revised form: 2018-02-01
Accepted for publication: 2018-02-14

A Parametric Thermal Analysis of Triangular Fins for Improved Heat Transfer in Forced Convection

Saroj Yadav – Krishna Murari Pandey*
National Institute of Technology Silchar, India

Thermal management systems in electronic devices require a reduction in size due to improve the overall performance of the system. The aim is to improve the heat transfer with reduction in weight of the system. Fins are the extended surfaces that ease the heat transfer process by increasing the wetted surface area. The thermal diffusion in a fin is always affected by parameters like the size, the shape, the material, the relative arrangement, orientation and position of the fins, the working fluid and its velocity, etc. Moreover, an extended surface may affect the pressure gradient in the flow domain. In this article, a three dimensional (3D) system of aluminium fin system has been numerically modelled. Simulations are done for conjugate heat transfer problem with fins of triangular shape. The thermal analysis is performed for various input parameters viz., arrangements, orientation and the number of fins. The effect of these parameters are analysed based on Nusselt number, convective heat transfer coefficient, coefficient of friction and coefficient of pressure.

Keywords: conjugate heat transfer, extended surfaces, finite element method, heat transfer co-efficient, Nusselt number, triangular fins

Highlights

- *The extended surface improves the heat transfer rate in any system by improving the thermal interaction between the solid surface and the fluid.*
- *Heat transfer rate in a fin is always affected by the size, the shape, the material, the relative arrangement, the orientation and position of the fins, the working fluid and its velocity, etc.*
- *Presence of an extended surface affects the pressure gradient in the flow domain.*
- *Variation of Nusselt number, frictional coefficient, pressure coefficient and heat transfer co-efficient are affected by the arrangement, orientation and the number of fins.*

0 INTRODUCTION

Any system is under working condition generates heat. Sometimes, the amount of heat that it generates reaches the threshold limit of the system. Therefore, in order to avoid the damaging of the components of the system due to burning or overheating, it is very important to remove the heat in an effective way. Thus, heat transfer in enhanced rate is one of the important topics of thermal engineering. Enhancing the heat transfer rate with the controlled system dimension in the equipment like electronics, heat exchangers, aeronautical, internal combustion engine, etc. have always been a challenging task. To conquer this, researchers are continuously giving their effort in designing or reconstructing a new device with high thermal performance. These devices are intended for cost-effective and energy efficient transfer of heat in the compact areas without any thermodynamic loss. In this concern, an array of fins is one of the possible ways to increase the heat transfer rate from the base surfaces. This method can increase the heat transfer area that comes in contact with the fluid. Fin geometries and fin arrays can create turbulence in the fluid flowing, this further increase the heat transfer coefficient (h) between systems and surrounding and thus improve the performance. However, it gives rise to the pressure drop, which is a critical condition in most high performance applications. Consequently, it can be said that an optimized fin geometry and fin array combination is a conciliation of performance, pressure drop, weight, and size.

The fin materials usually have a high thermal conductivity, thus it conducts the heat from the wall in high rate. Mostly, fins are used to enhance convective heat transfer by creating the temperature difference between the object and the environment. This in turn increases the convection heat transfer coefficient. Pin fin heat sinks are one of the competent heat exchanging devices used in many electric cooling appliances including central processing unit (CPU), transformer and thyristor. Thus most of the high thermal performance application based fins are made of copper or aluminium. Aluminium is always a preferred material for fins used in electronic system for cooling applications, due to its higher thermal conductivity and light weight.

Researcher proposed many techniques through experimental, analytical and numerical analysis for the performance augmentation of extended surfaces, specifically pin fin heat exchanger. Pin-fin arrays induced turbulence in the flow field which further

*Corr. Author's Address: National Institute of Technology Silchar, Department of Mechanical Engineering, Silchar, Assam, India, kmpandey2001@yahoo.com

helpful in enhancement of heat transfer. Axtmann et al. [1] focused their studies on thermally inactive pin-fins and presented the heat transfer results in terms of Nusselt number (Nu) and also discussed about other individualities like pressure drop and thermal performance parameter of investigated configurations. Şara [2], experimentally investigated the heat transfer, pressure and performing individualities for the array of staggered square pin fins attached on a flat surface in a rectangular duct and compared it with those for the inline arrangement. Jeng and Tzeng [3] also explore the heat transfer and the pressure drop in square pin-fins with variable inter-fin pitches for understandings of pin-fin arrays and systematic experiments has been performed, consequently the optimal inter-fin pitches are provided. Metzger et al. [4] presented variation in stream wise heat transfer, overall array heat transfer, and overall flow friction behavior for large aspect ratio ducts, that contained uniformly spaced staggered arrays of circular pin fins. Agarwal et al. [5] explored the effectiveness of pin fins for heat transfer in a channel cooled by air and agitated by a translational oscillating plate. Park et al. [6] designed a staggered pin-fin radial heat sink. The system was optimized for cooling of light-emitting diode (LED) device. They developed a numerical model to simulate various pin-fin array heat sinks. The results were verified experimentally. Huang et al. [7] estimated the optimal diameters for perforated pin fin array based on the desired temperature difference between base plate averaged temperature and ambient temperature and system pressure drop. The heat transfer and friction factor characteristics of the perforated rectangular fins were determined by Sahin and Demir [8]. The performances of three dimensional (3D) conjugate thermo-fluid analysis of micro pin-fins were presented by Abdoli et al. [9]. They considered a conventional circular shape, a hydrofoil shape, a modified hydrofoil shape and a symmetric convex lens shape of a fin. Joo and Kim [10] presented an analytical comparison of the thermal performances of optimized plate-fin and optimized pin-fin heat sinks under fixed volume condition. McNeil et al. [11] measured the heat-transfer coefficient and pressure drop measurements for a heat sink comprising micro pin–fins.

In the following, a study has been performed on triangular fins with different geometrical parameters. The solver and the developed model are validated with the experimental data and with empirical relations available in the literature. Further, the variation of Nu, h, coefficient of friction (C_f) and coefficient of pressure (C_p) are studied by varying the arrangement, orientation and the number of fins.

1 FORMULATIONS AND GEOMETRY

Thermal analyses of extended surfaces of different shapes are performed in this article.

1.1 Experimental Set-Up

Experiments are carried out to understand the performance of a set of aluminium pipe bundle arranged in a staggered manner. Fig. 1a shows the experimental set-up used in the current study. The set-up consists of a vertical square duct with an axial flow fan placed just below the outlet temperature sensor. Air enters the duct from the bottom and leaves it from the top. The staggered arrangement of the pin fin system with the base plate as shown in Fig. 1b. The fins with the base plate are connected with the heater unit to supply heat from the bottom of the plate (Fig. 1b). The removable set-up (Fig. 1b) of fins with heating unit is placed inside the duct in the test section. The placement of the fins in the test section provides normal direction of flow to the incoming fluid (Fig. 1a). Fixed temperature sensors are provided

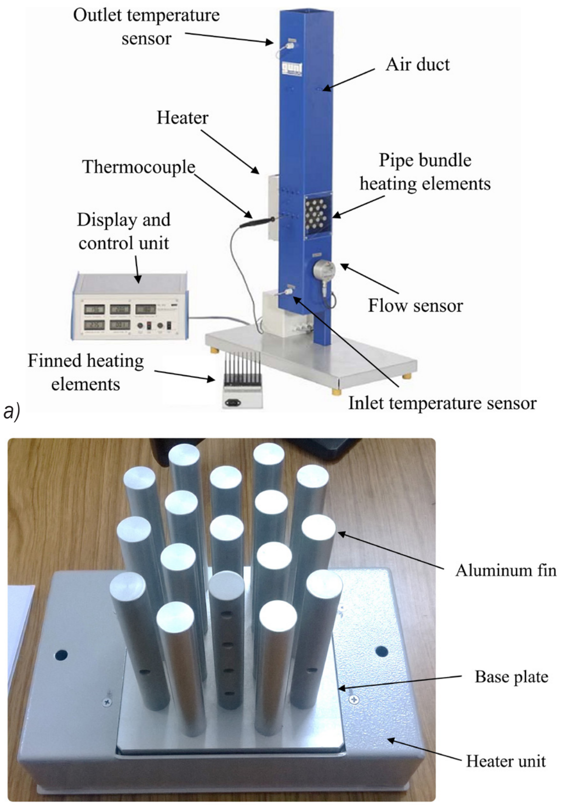

Fig. 1. *The experimental setup of a) heat convection apparatus, and b) pipe bundle heating element*

at the inlet and the outlet of the duct to measure the temperatures of incoming and outgoing air, respectively. A portable thermocouple is also provided to measure the temperature at different locations of the fins. The display and control unit helps in controlling the speed of the fan and the amount of supplied heat to the heating unit.

1.2 Computational Model

Consideration is given to a 3D numerical model of aluminum pipe bundle placed in an air duct of dimension $L \times H \times L$ (Fig. 2a). The fins of diameter D and height l, arranged in a staggered formation are placed over a base plate of dimension $L_b \times L_b \times H_b$ (Fig. 2b). The arrangement is located inside the air duct at a distance $(H - L_b)/2$ from the inlet. With a longitudinal and transverse pitch of S_L and S_T, the system is analyzed for a forced convection scenario. The considered numerical model is validated prior to the analysis of different cases. Air is driven inside the duct at an isothermal room temperature T_f and velocity V in the positive y direction. Numerically, the outlet is considered to be at atmospheric pressure (P_o) and at outflow condition $\left(\hat{n} \cdot \nabla T = 0\right)$. The walls of the air duct are at no slip conditions $\left(\left|\vec{V}\right| = 0\right)$ and at an isothermal room temperature T_f (Fig. 2a). The base plate of the fin system is supplied with a total uniform heat of Q_s.

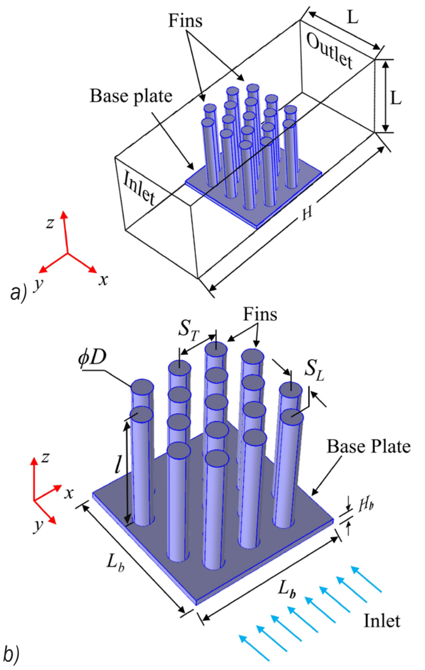

Fig. 2. *Schematic diagram of the a) computational domain, and b) fin geometry*

1.3 Governing Equations

Thermal behavior of any system is determined by the participated modes of heat transfer, and the thermo physical properties of the system.

1.3.1 Experimental Analysis

In this study, the experimental analysis has been performed considering the force convection over the fin surfaces. The system is analysed based on the performance parameters like h and averaged Nu. The facility helps in measurement of various thermo physical properties of the system like system dimensions, the velocity and the temperature at various points. These quantities forms the basis for calculation of h and Nu in the system. For the current system (Fig. 1a), at various inlet flow velocities, with known values of temperature at inlet, outlet and over the fins, the h is calculated from the thermal energy balance. In ideal scenario, neglecting any heat loss from the back of the heater and from the duct walls (Fig. 1a), the rate of heat convection from the surface of the fin will be equal to the rate of heat carried by the incoming air. Mathematically, it can be expressed as,

$$hA_{fin}\left(T_{fin} - T_{in}\right) = \dot{m}c_p\left(T_{out} - T_{in}\right), \tag{1}$$

where the A_{fin} is the wetted surface area of the fin, the T_{fin} is the average surface temperature and $\dot{m}\left(= \rho A_{duct} V\right)$ is the mass flow rate inside the duct. Considering diameter D of the fin as the characteristic length, the average Nu is calculated using hL/k_f.

1.3.2 Uncertainty in Experimental Data

Every experiment needs analysis of uncertainty in the measured quantities. The uncertainty in the dependent derived quantities are due to various errors that appear in the measured quantities. In the present case, the uncertainty in the measurement of h and Nu are calculated using root mean square combination Eq. (2). In general, for any quantity λ, it is expressed as

$$E_\lambda = \sqrt{\sum_{i=1}^{N}\left(\frac{\partial \lambda}{\partial x_i} E_i\right)^2}, \tag{2}$$

where E_i is the uncertainty in the generic variable x_i. In the calculations of uncertainty of h, the generic variables are various areas, A_{duct} and A_{fin}, velocity V, and temperatures T_{in}, T_{out} and T_{fin}. Similarly, for Nu, it will be h and D.

1.3.3 Numerical Analysis

The numerical study of the fin geometry requires combination of multiple physics of heat transfer and fluid flow to capture variation of temperature, velocity and pressure field in the domain (Fig. 2a). Considering forced convection over the present system, the conjugate heat transfer energy equation is expressed as,

$$\rho c_p\left(\frac{\partial T}{\partial t}+\vec{V}\cdot\nabla T\right)=\nabla\cdot\left(k\nabla T\right), \tag{3}$$

where ρ, c_p and k are the density, the specific heat and thermal conductivity of the materials of the system. The ∇ is the gradient operator. In the above equation, the first and the second terms are the rate of accumulation of thermal energy and the rate of transfer of thermal energy due to bulk motion of the fluid, respectively. The term on the right hand side corresponds to the rate of thermal diffusion in the material.

With the known value of thermal properties, evaluation of temperature field of the system from Eq. (3) requires the knowledge of the velocity field. Therefore, apart from the energy equation, the governing equations of the considered system (Fig. 1a) also include steady form of continuity and momentum equations, given by

$$\nabla\cdot\left(\rho\vec{V}\right)=0, \tag{4}$$

$$\vec{V}\cdot\nabla\vec{V}=-\frac{1}{\rho}\nabla p+\nu\,\nabla^2\vec{V}. \tag{5}$$

The governing equation Eqs. (3) to (5) has been solved numerically using finite element method (FEM). The discretization is performed using COMSOL multiphysics, a commercially available FEM solver. Simultaneous solution of Eqs. (3) to (5), using the mentioned boundary conditions yields the velocity and the temperature profiles in the computational domain. The average Nu and h in such cases are calculated using

$$\mathrm{Nu}=\frac{Q_S D}{k_f A\left(T_w-T_f\right)}=\frac{hD}{k_f}, \tag{6}$$

where A and T_w are the area of the base plate ($L_b \times L_b$) and the average surface temperature of the fin walls, respectively.

The skin friction and the pressure coefficients are two non-dimensional quantities that gives an overview how the flow is interacted with the contact surface. Mathematically,

$$C_f=\frac{2\tau_w}{\rho V^2}, \tag{7}$$

$$C_p=\frac{2\Delta P}{\rho V^2}, \tag{8}$$

where τ_w and ΔP are local wall shear stress [N/m^2] and pressure difference [N/m^2] respectively.

1.3.4 Empirical Relations

Fluid flow across a heated cylindrical pin fin is a common problem in various engineering applications. One such work has been carried out by Khan et al. [12]. The authors in this work have discussed on cylindrical pin fin heat sink with application in electronic thermal management system. Khan et al. [12] have proposed mathematical relationships h for fin with various physical parameters of fin geometry. For any pipe bundle arrangement, with an approaching fluid velocity of $U=\left|\vec{V}\right|$ the Reynolds number (Re) for the flow is defined as

$$\mathrm{Re}_D=\frac{\nu U_{\max}}{D}, \tag{9}$$

where ν is the kinematic viscosity of the flowing fluid and $U_{\max}$ is the maximum fluid velocity around the fins. As proposed by Khan et al. [12], the $U_{\max}$ is obtained from the empirical relation given by

$$U_{\max}=\max\left(\frac{S_T}{S_T-D}U,\ \frac{S_T}{2\left(S_D-D\right)}U\right), \tag{10}$$

where $S_D=\sqrt{S_L^2+\left(S_T/2\right)^2}$ is the diagonal pitch in the present case. Using these physical parameters of the system, the average Nu for the staggered arrangement fins is expressed in terms of Re and Prandtl number (Pr) as

$$\mathrm{Nu}=\frac{hD}{k_f}=C_1\,\mathrm{Re}_D^{1/2}\,\mathrm{Pr}^{1/3}, \tag{11}$$

where $C_1=\dfrac{0.61 S_T^{0.091} S_L^{0.053}}{1-2e^{-1.09 S_L}}$ [12].

For a cylindrical pin fin geometry, considering the results obtained from the experiments, the numerical model is validated. The set of results are also compared with the values of Nu and h obtained from the above mentioned empirical relations [12].

2 RESULTS AND DISCUSSION

The considered numerical model has been developed based on the available experimental set-up (Fig. 2). In order to compare the results of numerical solver with experiment, the boundary conditions are carefully chosen to simulate the realistic scenario of experiments. Consideration is given to 17 number of Aluminum k=237 W/(m·K), ρ=2700 kg/m³, C_p=900 J/(kg·K), cylindrical pin fins (D=15 mm, l=105 mm) placed over a base plate of dimension ($L_b \times L_b \times H_b$) 118 mm × 118 mm × 5 mm. The fins are arranged in 3 rows of 3 fins and 2 rows of 4 fins (Fig. 2b). The arrangement is placed inside square duct of dimension ($L \times H \times L$) 120 mm × 120 mm × 628 mm (Fig. 2a). In the numerical model, the height (H) of the square duct is kept as 628 mm instead of 1000 mm of the actual experimental set-up. The consideration has been made in order to reduce the size of the computational domain and to nullify the effect of the outlet conditions. During the experiment, the fin geometry along with the base plate is subjected to a total heat of 115 W, normal to the bottom of the base plate. The experiments are performed at five different ambient conditions. The results are noted down at steady state condition of the system. In order to check the repeatability of the measurement systems, four readings are recorded corresponding to a single setting of the process parameters. Uncertainty in the estimation of Nu and h are also shown while comparing with numerical and empirical results.

The Nu is a parameter that depicts the strength of the convection heat transfer rate compared to the conductive heat transfer rate. The performance parameters (Nu and h) in the considered system are calculated using the experimental data (Eq. (1)), empirical relations Eqs. (9) to (11) and computationally (Eq. 6). The empirical relationships proposed by Khan et al. [12] are applicable for a staggered arrangement of cylindrical pin fin, which are independent of the boundary conditions. With longitudinal and transverse pitch of (S_L) 20 mm and (S_T) 30 mm, respectively the Nu and h are calculated using the given relations (Eqs. (9) to (11)). The Re and Pr are the flow dependent parameters that can be calculated using the maximum velocity U_{max} and other fluid properties. For all the above study, the Nu and h is calculated based on the diameter D of the fins.

With tetrahedral grid to discretize the computational domain, the grid dependency tests were performed for different sizes of the grid. Using a grid having 15,84,685 numbers of elements, the governing equations were solved for a steady-state condition. Five cases are taken into considerations for various inlet velocities of air viz., 1.1 m/s, 1.3 m/s, 1.5 m/s, 1.8 m/s and 2.0 m/s. Table 1 shows comparative values of average Nu and h for different cases of inlet velocities. A comparative plot of the same is also presented in Fig. 3.

Having validated the numerical solver, the fins of triangular shape are considered for study. The fins are modeled in such a way that the volume of the system is always maintained constant (229 mm³). For the study of effect of number of fins, in order to maintain uniformity in the modeling, the heights to base ratio of the fins are always kept same for all the cases, i.e., 2.5.

Table 1. *Comparison of empirical and numerically obtained* Nu *and* h *for various conditions of Inlet velocity and temperature*

V	Nu			h [W/(m²·K)]			% Error in estimation of Numerical Nu with		% Error in estimation of Numerical h with	
	Experimental Results	Empirical Results [12]	Numerical Results	Experimental Results	Empirical Results [12]	Numerical Results	Experimental Results	Empirical Results [12]	Experimental Results	Empirical Results [12]
1.1	27.9	29.0	26.8	48.8	50.7	45.9	4.1	8.2	6.3	10.5
1.3	30.4	31.5	32.7	53.1	55.1	56.1	7.2	3.8	5.3	1.8
1.5	33.0	33.8	34.4	57.6	59.1	58.9	4.1	1.7	2.2	0.3
1.8	38.6	37.1	36.2	67.5	64.8	62.0	6.6	2.5	8.8	4.5
2.0	42.2	40.0	42.3	73.7	70.0	72.4	0.2	5.4	1.8	3.4

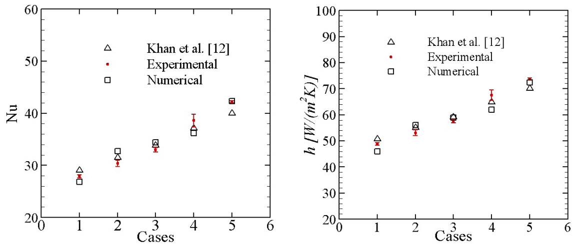

a) b)

Fig. 3. *Comparison of numerical, experimental and empirical values of: a)* Nu *and b)* h

2.1 Inline vs. Staggered Arrangement

The relative position of the fins plays an important role in the heat transfer process. In this study, the thermal analysis is performed on a 2-2 inline and 2-1-2 staggered arrangement of fins as described in (Fig. 4). The base (b) and the altitude (a) of the fin are selected in a way to accommodate the fin-base plate assembly in a space of 13 × 13 mm². For the inline arrangement of the fins, the base (b) and the altitude (a) is taken as 4.9857 mm and 10 mm, respectively.

As the number of fins in the considered staggered arrangement is more than that of the inline arrangement, the base and altitude of the fins in this case will reduce to 3.989 mm and 10 mm to maintain a total volume of 229 mm^3. The thicknesses of the fins are also maintained at a constant value of 0.6 mm, throughout the study. The set of fins are placed over a baseplate of 1 mm thickness with the trailing edge located at y = 0. The system is supplied with a total uniform heat (Q_s) of 2 W from the base of the base plate. A unidirectional flow of air is imposed as the inlet condition with velocity of 0.5 m/s. Fig. 5a and b show the results obtained from the numerical simulations. The stream line of velocity plot in a horizontal section (z = 6 mm) shows the flow over the considered extended surfaces. In the staggered arrangement, the interaction between the solid and air is observed to be more compared to the inline arrangement. It is due to the placement of the fifth fin between two rows in the staggered arrangement. The contours in the Fig. 5 shows variation of temperature at the horizontal middle plane (z = 6 mm) of the rectangular domain.

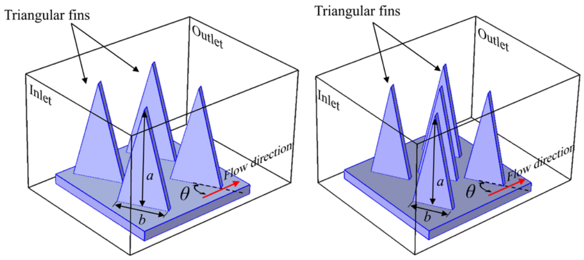

a) b)

Fig. 4. *Schematic diagram of a) inline, and b) staggered arrangement of triangular fins*

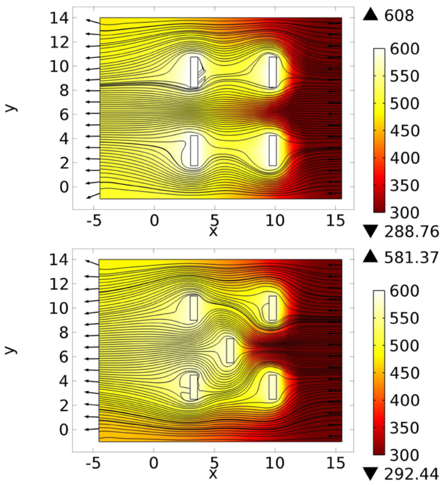

a)

b)

Fig. 5. *Velocity streamline, direction and surface temperature [K] variation in: a) inline, and b) staggered arrangement of fins in a plane at z = 6 mm*

Following the formulations in the previous section, the values of h and the Nu is calculated for the considered inline and staggered arrangement. For the staggered arrangement of triangular fins, h is observed to be 44.14 W/(m^2·K), which is 22 % higher than the value in case of inline arrangement, i.e., 34.46 W/(m^2·K). The observed increment in h is due to a better interaction at the fluid-solid interface. The increased number of fins in this case also helped in increasing the total wetted surface area of the fin by 2.56 %, which in turn enhances the heat transfer rate. Hence, there is an increment in the Nu too. The Nu value increases from 1.18 to 1.46 in case of staggered arrangement compared to inline arrangement.

The presence of the fins inside the rectangular duct induces a circulation in the flow. The same is realized from the variation of y-component of velocity (Fig. 6), immediately after the flow passes over the fins (at x = 0). The clockwise and the counterclockwise vortices formed due to the fin structure shows more prominent presence near the left and the right wall of the duct, respectively, for both arrangements. Therefore, the air near these boundaries have almost equal thermal interaction and heat dissipation near the walls as that of the core (Fig. 6). With an improved rate of heat transfer in staggered arrangement in triangular fins, next the study has been extended to understand the flow losses with the help of C_f and C_p. Upon comparison, it has been found that the inline arrangement of fins yield a higher value of C_f and C_p than the staggered arrangement of the fins. A staggered arrangement of the fins with equivalent inline arrangement, having same material volume show C_f = 0.0678 and C_p = 9.325. On the other hand, the same quantities for inline arrangement have been obtained as 0.08716 and 9.67, respectively. Although the dimensions of the fins in both the arrangements are opted in a way to maintain a uniform volume, however, the wetted surface area obtained for both the cases are found different. In the inline arrangement of the fin system, four fins along with the base plate are having total approximate wetted surface area of 398 mm^2. On the other hand, the system of fins in the staggered arrangement consists of 361 mm^2. The reduced wetted surface area in the staggered arrangement leads to lesser frictional losses in the flow system. Therefore, in comparison to inline arrangement, the staggered arrangement of the fins yields 22 % and 3 % reduction in the value of C_f and C_p, respectively. Therefore, a staggered arrangement always results in higher value of heat transfer rate with minimum flow losses, over the inline arrangement.

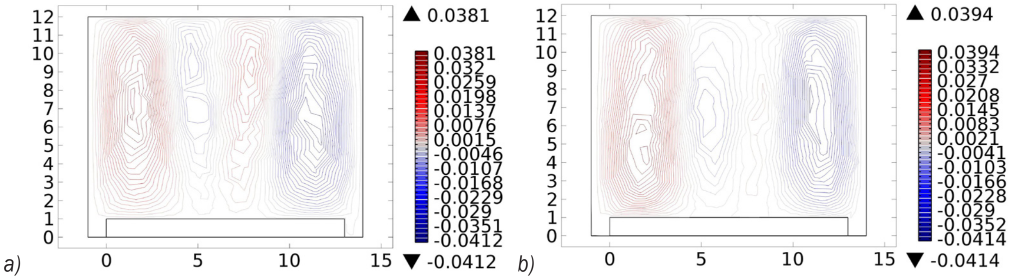

Fig. 6. *Contour profile of y-component of velocity (v, [m/s]) in a) inline, and b) staggered arrangement of fins in a plane at x = 0*

2.2 Relative Orientation of the Fins

Presence of an extended surface contributes in the pressure drop along the flow direction. In this regard, the orientation of the surfaces plays a major role. The current study focuses on the study of relative orientation of the fins with flow direction on heat transfer and fluid flow. Considering five variation of angles viz., 0°, 30°, 45°, 60° and 90°, thermal analysis is made on triangular fins under same thermal load and boundary conditions.

Fig. 7 shows the surface temperature contour and the velocity streamlines at z = 6 mm for all the considered cases. In case of triangular fins with θ = 0°, the temperature contour shows a better distribution of temperature of air throughout the computational domain. However, due to angular orientation of the fins the flow is diverted towards one of the boundary which is parallel to the horizontal axis. Therefore, in case 30°, 45° and 60°, the temperature contour and the streamlines are observed to deviate towards the flow direction. In case with θ = 90°, for the fluid moving normal to the triangular face of the fins, the fluid particles reaches a stagnation condition and imposes pressure on the fin wall (Fig. 8). The situation is less prominent as one move from 90° through 0°.

Therefore, due to symmetric flow of air, in case of θ = 0°, with better thermal interaction, a better heat transfer phenomenon is observed. The same may be realized from the calculation of Nu and h. Fig. 9 shows a comparative bar diagram of all the above cases. For the fins with triangular faces parallel to the flow direction, the Nu and h is observed to be 1.45 and 42.9 W/(m^2·K), respectively. The case with θ = 45°, yields the maximum h with 44.22 W/(m^2·K). However, due to almost equal strength of convection to diffusion, the systems with θ = 45° and 60° yields almost equal value of average Nu.

The relative orientation of the fin with respect to the incoming flow direction is also having effect on the flow losses. The effect of change of angle θ is

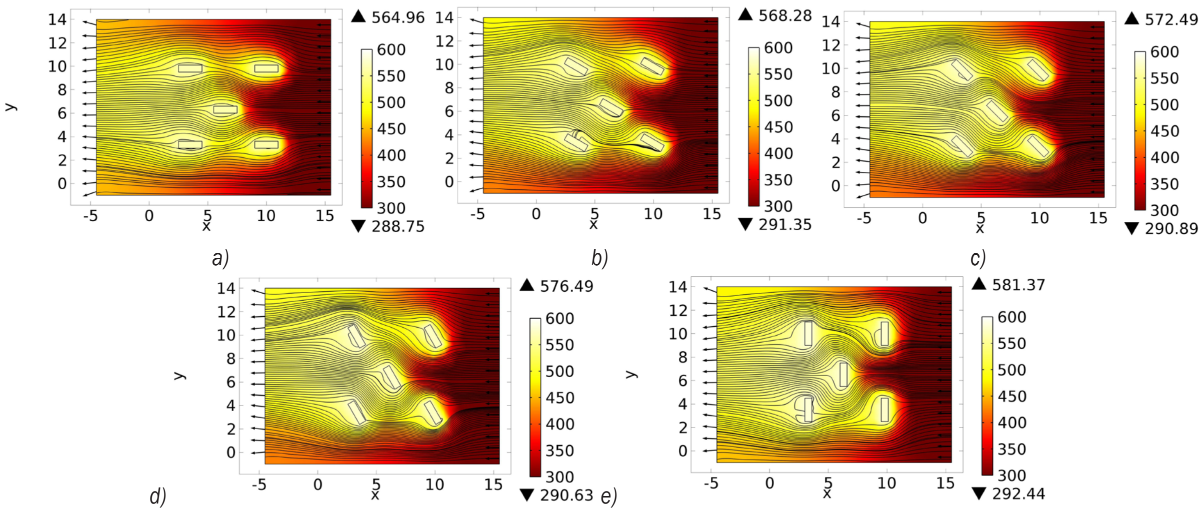

Fig. 7. *Velocity streamline, direction and surface temperature [K] variation in staggered arrangement of fins at z = 6 mm, with θ = a) 0°, b) 30°, c) 45°, d) 60°, e) 90°*

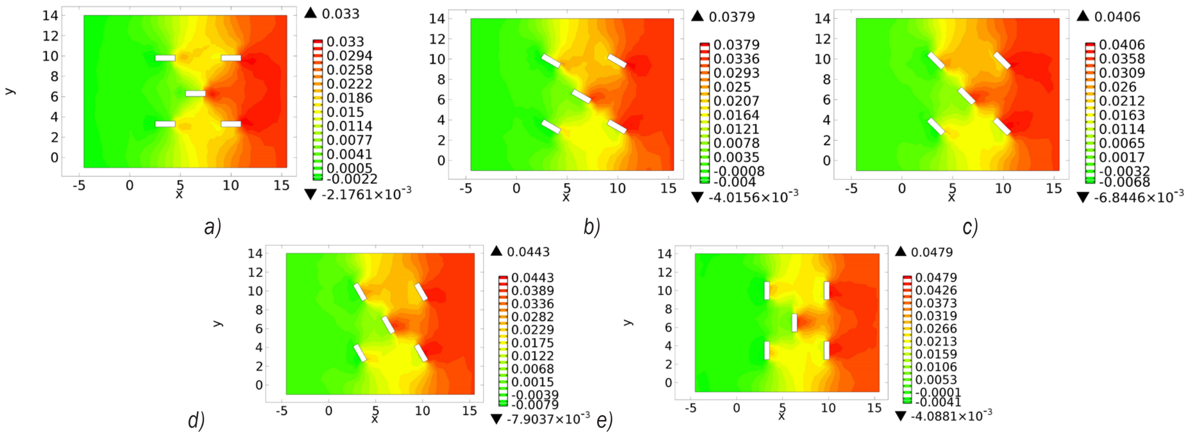

Fig. 8. Contour profile of pressure (Pa) in staggered arrangement of fins at z = 6 mm with θ = a) 0°; b) 30°; c) 45°; d) 60°; and e) 90°

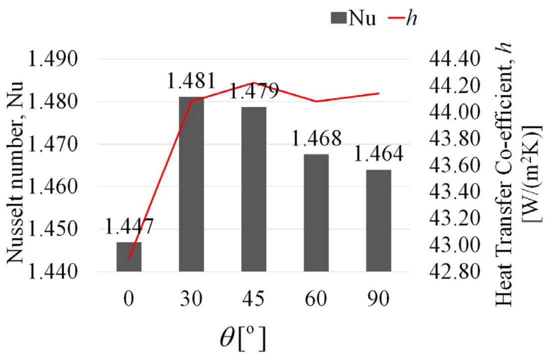

Fig. 9. *Variation of* Nu *and* h *for values of angle θ of triangular fins arranged in 2-1-2 staggered arrangement*

observed in the variation of C_f and C_p. Fig. 10 show the effect of θ on C_f and C_p for staggered arrangement of triangular fins with 2-1-2 configuration. A change in the angle of attack of the flow on the triangular fin leads to change in the formation of circulation zones downstream of the fin assembly. Fig. 11 represents the contours of y-component of velocity in yz-plane immediately after the fin assembly, at x = 0. It has been found that the section of the flow show two different orientation of the circular motion. The velocity v in positive y direction is marked in red and the one with blue color is observed to be in the negative y-direction. Upon comparison, it has been found that a staggered arrangement of triangular pin fin oriented in 0° and 90° yield two distinct vortices (Figs. 11a and e). However, the maximum velocity of the circulation zone is observed more in case of 90° (0.0391 m/s), compared to 0° (0.0314 m/s). A fin with 0° orientation, leads to lesser resistance in the flow compared to 90°. Therefore, the case with θ = 0° yield a minimum and lesser value of C_f and C_p compared to θ = 90° (Fig. 10). Now, when observing the cases with 0° < θ < 90°, it has been found that the orientation of the fins leads to formation of four distinct vortices, making it to behave like a vortex generator. A fin at θ = 60° yields vortices with maximum strength of the core (0.0449 m/s and –0.0408 m/s). This leads to maximum values of C_f and C_p for θ = 60°. It has been found that a fin placed at 30°, 45°, 60°, and 90° produces 25

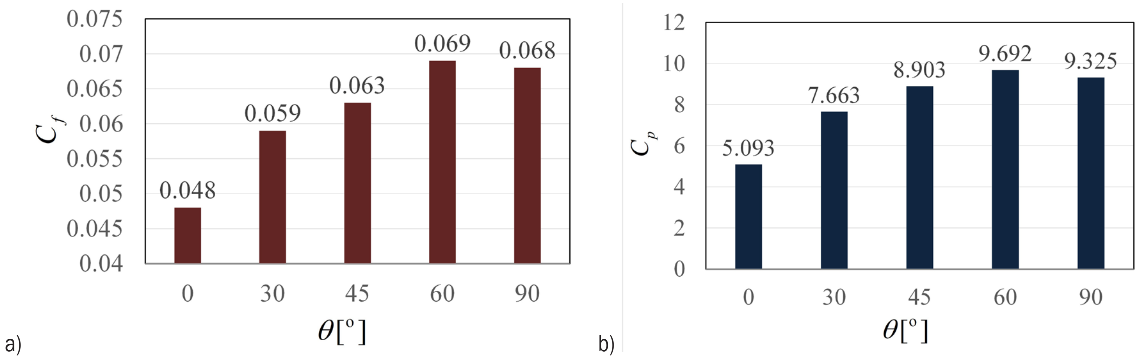

Fig. 10. *Variation of a)* C_f *and b)* C_p *in staggered arrangement of fins with θ = 0°, 30°, 45°, 60°, and 90°*

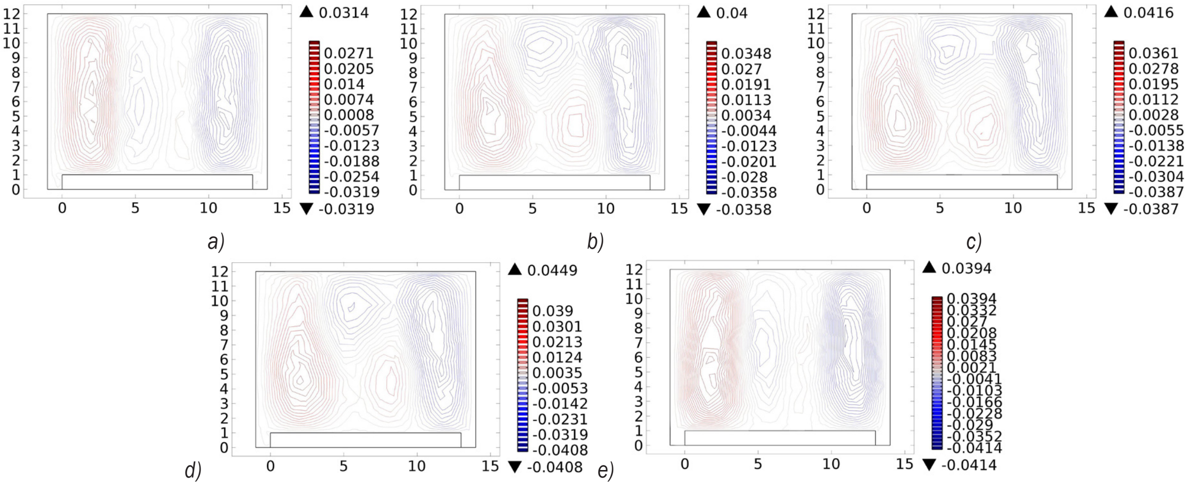

Fig. 11. *Contour profile of y-component of velocity v [m/s] in staggered arrangement of fins in a plane at x = 0, with θ = a), 0°, b) 30°, c) 45°, d) 60°, e) 90°*

%, 32.5 %, 44.8 % and 42.7 %, respectively, more frictional losses in the flow compared to the case with 0°. On the other hand, the same set of fins at different angles produces 50.4 %, 74.8 %, 90.3 % and 83 % more pressure losses in the domain compared to the fin system parallel to the flow, i.e., 0°.

2.3 Number of Fins

With the understanding of heat transfer process in different arrangements of the fins, next the study has been extended to observe the effect of number of fins in the system. Four different cases with staggered arrangement of fins are considered with 2-1-2 (5 fins), 3-2-3 (8 fins), 4-3-4 (11 fins) and 5-4-5 (14 fins) staggered arrangement. The fins are place at angle θ = 0° with the flow direction. A schematic diagram of the same is shown in Fig. 12. To maintain uniformity, the volume of all the fins and the aspect ratio (altitude: base) of individual fin is maintained the same as the earlier cases i.e. 2.5. Table 2 shows the results obtained from the numerical analysis for same boundary and thermal load conditions. It has been observed that as the numbers of fins are increased, the wetted surface area of the fins also increases, although the volume is remaining constant. However, the characteristic length of the fins decreases with increase in the number of fins. This affects the value of Nu and h. As the number of fins increases the Nu and the h decreases.

Fig. 13 show variation of C_f and C_p for various configurations. As the number of fins increases, the wetted surface area of the domain increases. The increment in the surface area leads to more amount of shear stress experienced by the fin system. Hence, as the number of fins increases, the value of C_f also increases (Fig. 13a). However, the variation of C_p depicts a different scenario. As one moves from staggered 2-1-2 configuration to 3-2-3 configurations, the wetted surface area increases along with differential pressure. However, the relative rate of increment of pressure drop is found more than the increment in the wetted surface area in case of 2-1-

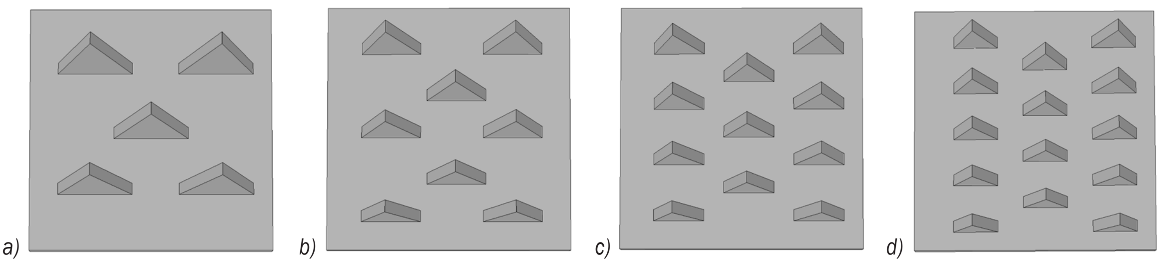

Fig. 12. *Schematic diagram of staggered arrangement of fins placed parallel to the flow direction with; a) 2-1-2; b) 3-2-3; c) 4-3-4; d) 5-4-5 configuration*

2 configuration compared to 3-2-3 configurations. Hence, an increment in C_p is observed. As one move from 3-2-3 to 4-3-4 configuration, the ratio of pressure drop with respect to dynamic pressure is found to reduce and hence, the value of C_p decreases further.

Table 2. *Comparison of values of Nu and h for various numbers of fins placed parallel to the flow direction with staggered arrangements*

Cases	Number of fins	Nu	h [W/(m²·K)]	Wetted surface area [mm²]	Characteristic length [mm]
2-1-2	5	1.48	44.22	469.66	1.95
3-2-3	8	1.87	59.24	482.69	1.90
4-3-4	11	1.26	41.97	493.45	1.85
5-4-5	14	1.11	39.06	502.73	1.82

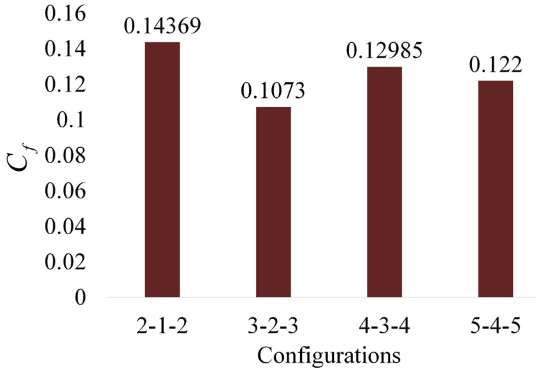

a)

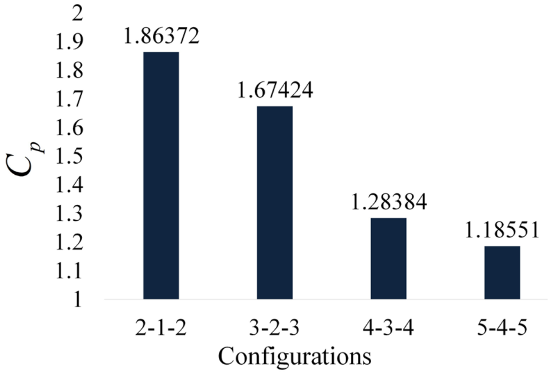

b)

Fig. 13. *Variation of a) C_f; and b) C_p in staggered arrangement of fins of various configuration*

3 CONCLUSIONS

The present work reported thermal analysis of triangular shaped fins for different parametric conditions. The problem is analyzed numerically using an FEM solver. The numerical model, boundary conditions and the solver is validated for cylindrical fins of staggered arrangement using the experimental data and empirical relationship proposed by Khan et al. [12]. The comparison shows an acceptable agreement. Further, the analysis is done on triangular shaped fins for a fixed value of inlet Re. A comparison of the inline and staggered arrangement is shown and is observed that the staggered arrangement gives a better heat transfer rate from a solid surface to the fluid. Fins with staggered arrangement and placed parallel to the incoming flow is found to yield an enhanced value of Nu and h. It has also been observed, as the number of fins increases the heat transfer rate deteriorate due to reduced value of characteristic length of the fins geometries. A change in configuration of the fin system affects the losses in the flow domain. A staggered arrangement as considered in the current study yield a lower value of C_p and C_f. Fins placed parallel to the flow direction are more streamlined and found to have minimum pressure loss and frictional loss. Therefore, a triangular fin system with staggered arrangement placed parallel to the flow direction may be preferred from effective thermal and flow behavior point of view. In the present study, the effect of increment of number of fins is found to affect the heat transfer and the fluid flow physics. However, it is difficult to predict the effect of number of fins on C_p and C_f, for staggered arrangement of fin system.

4 NOMENCLATURES

A	area, [m²]
c_p	specific heat, [J/(kg·K)]
C_p	coefficient of friction, [-]
C_f	coefficient of pressure, [-]
C_1	arbitrary constant, [-]
D	diameter, [mm] or [m]
H	height, [mm] or [m]
h	heat transfer coefficient, [W/(m²·K)]
k	thermal conductivity, [W/(m·K)]
l, L	length, [mm] or [m]
$\hat{n}$	unit normal vector, [-]
Nu	average Nusselt number, [-]
p	pressure, [Pa] or [N/m²]
P_o	atmospheric pressure, [Pa]
Pr	Prandtl number, [-]
Q_s	heat supplied, [W]
Re	Reynolds number, [-]
S	pitch, [mm] or [m]
t	time, [s]
T	temperature, [K]
$\vec{u}_y$	y- component of velocity, [m/s]
U, $\vec{V}$	total velocity, [m/s]
x, y, z	co-ordinate axes, [-]

Greek Symbols

ν dynamic viscosity, [N·s/m²]

ρ density, [kg/m³]

θ inclination in degree, [°]

Subscripts

b base plate

D diameter or diagonal

f fluid

L longitudinal

max maximum

T transverse

w wall

5 REFERENCES

[1] Axtmann, M., Poser, R., von Wolferdorf, J., Bouchez, B. (2016). End wall heat transfer and pressure loss measurements in staggered arrays of adiabatic pin fins. *Applied Thermal Engineering*, vol. 103, p. 1048-1056, **DOI:10.1016/j.applthermaleng.2016.04.066**.

[2] Şara, O. N. (2003). Performance analysis of rectangular ducts with staggered square pin fins. *Energy Conversion and Management*, vol. 44, no. 11, p. 1787-1803, **DOI:10.1016/S0196-8904(02)00185-1**.

[3] Jeng, T.-M., Tzeng, S.-C. (2007). Pressure drop and heat transfer of square pin-fin arrays in in-line and staggered arrangements. *International Journal of Heat and Mass Transfer*, vol. 50, no. 11-12, p. 2364-2375, **DOI:10.1016/j.ijheatmasstransfer.2006.10.028**.

[4] Metzger, D. E., Berry, R. A., Bronson, J. P. (2009). Developing heat transfer in rectangular ducts with staggered arrays of short pin fins. *Journal of Heat Transfer*, vol. 104, no. 4, p. 700-706, **DOI:10.1115/1.3245188**.

[5] Agrawal, S., Terrence, W.S., North, M., Bissell, D., Cui, T. (2015). Heat transfer augmentation of a channel flow by active agitation and surface mounted cylindrical pin fins. *International Journal of Heat and Mass Transfer*, vol. 87, p. 557-567, **DOI:10.1016/j.ijheatmasstransfer.2015.04.036**.

[6] Park, S.-J., Jang, D., Yook, S.-J., Lee, K.-S. (2015). Optimization of a staggered pin-fin for a radial heat sink under free convection. *International Journal of Heat and Mass Transfer*, vol. 87, p. 184-188, **DOI:10.1016/j.ijheatmasstransfer.2015.04.036**.

[7] Huang, C.-H., Liu, Y.-C., Ay, H. (2015). The design of optimum perforation diameters for pin fin array for heat transfer enhancement. *International Journal of Heat and Mass Transfer*, vol. 84, p. 752–765, **DOI:10.1016/j.ijheatmasstransfer.2014.12.065**.

[8] Sahin, B., Demir, A. (2008). Performance analysis of a heat exchanger having perforated square fins. *Applied Thermal Engineering*, vol. 28, no. 5-6, p. 621-632, **DOI:10.1016/j.applthermaleng.2007.04.003**.

[9] Abdoli, A., Jimenez, G., Dulikravich, G. S. (2015). Thermo-fluid analysis of micro pin-fin array cooling configurations for high heat fluxes with a hot spot. *International Journal of Thermal Sciences*, vol. 90, p. 290-297, **DOI:10.1016/j.applthermaleng.2007.04.003**.

[10] Joo, Y., Kim, S. J. (2015). Comparison of thermal performance between plate-fin and pin-fin heat sinks in natural convection. *International Journal of Heat and Mass Transfer*, vol. 83, p. 345-356, **DOI:10.1016/j.ijheatmasstransfer.2014.12.023**.

[11] McNeil, D. A., Raeisi, A. H., Kew, P. A., Hamed, R. S. (2014). An investigation into flow boiling heat transfer and pressure drop in a pin–finned heat sink. *International Journal of Multiphase Flow*, vol. 67, p. 65-84, **DOI:10.1016/j.ijmultiphaseflow.2014.06.012**.

[12] Khan, W. A., Culham, J. R., Yovanovich, M. M. (2005). Modelling of cylindrical pin fin heat sinks for electronic packaging. *Proceedings of 21st IEEE Semiconductor Thermal Measurement and Management (SEMI-THERM) Symposium*, San Jose.

Strojniški vestnik - Journal of Mechanical Engineering 64(2018)6, 412-421

DOI:10.5545/sv-jme.2017.5023 *Original Scientific Paper*
Received for review: 2017-10-27
Received revised form: 2018-03-20
Accepted for publication: 2018-03-21

A Trajectory Compensation Model for Roll Hemming Applications

Eduardo Esquivel González[1,*] - José Pablo Rodríguez Arzate[2] - Giuseppe Carbone[3] - Marco Ceccarelli[3] - Juan Carlos Jáuregui[1]

[1]Autonomous University of Querétaro, Faculty of Engineering, México
[2]Technological Institute of Celaya, Department of Mechatronics, México
[3]University of Cassino, Laboratory of Robotics and Mechatronics, Italy

This paper presents a trajectory compensation model to correct the deviation in the roll hemming applications. First, the main defects and problems of roll hemming technology are established. A trajectory compensation proposal is analyzed as well as the kinematic and stiffness model of the robot and the material deformation model. The implementation of the model on an industrial robot is tested and simulated. Consequently, the viability of the model is discussed and compared with other works.

Keywords: roll hemming, wrinkling, tool center point, stiffness, trajectory

Highlights

- *An offline compensation strategy is implemented for roll hemming.*
- *The compensation strategy relies on the deviation due to the robot.*
- *The compensation strategy relies on the deviation due to the panel.*
- *The results show the new trajectory within the main parameters of the process.*

0 INTRODUCTION

Robots in automotive applications offer low-cost solutions for most of the manufacturing processes, opening new possibilities ranging from simple tasks, like pick and place, painting and sealing, to more complex tasks, like milling or welding [1]. This allows replacing the computer-navigated control (CNC) machines and stamping machines by using robotic manipulators in metal forming processes. They are also applicable for new processes like roll hemming, commonly used for doors, hoods and deck lids of the automotive industry. In the process, a serial robot moves a roller through the pre-hemming steps over the contour in order to attach the exterior panel to the interior panel of a door [2].

The roll hemming offers flexibility but different defects may appear in the final panel's shape. A common visible defect is the formation of waves on the flange, called wrinkles, related to the velocity and force of the roller. The origin of such defects relies on the capacity of the roller to deform the panel depending on the robot's pose. For example, an extended configuration pose demands higher torque and applies lower force than a constricted one that requires less torque and applies higher force. The stiffness of a robot (1 N/μm) is lower compared to a CNC machine (50 N/μm) [3], decreasing its capacity to follow a designated trajectory under external forces. As consequence, the final quality of the panel may vary along the trajectory. Most of the works of roll hemming process [4] are related to the finite element analysis and the prediction of the deformation patterns of the panel and few works [5] are focused on the dynamic performance of the robot. Accordingly, this paper proposes a compensation strategy for the roll hemming process based on the variable stiffness of the robot to minimize the tool deviation along the trajectory.

This paper proposes an offline compensation model for roll hemming with emphasis on determining the stiffness of the robot. A simulation of the process has been developed and the experimental tests show the error's results. If this compensation strategy is implemented, then a more accurate solution is achieved and a better quality of the product can be guaranteed.

This paper is structured in three main sections. The methods section establishes the trajectory compensation proposal and the analysis of each element concluding with the integration of the trajectory compensation model. The experimental section describes how the stiffness values were determined and how the forces and speed of the process were related to the wrinkling defect of the panel. Finally, the results section shows the values obtained from the computation of the algorithm and the deviation due to the error of the trajectory.

*Corr. Author's Address: Autonomous University of Querétaro, Cerro de las campanas S/N, Querétaro, México, je.esquivel@outlook.com

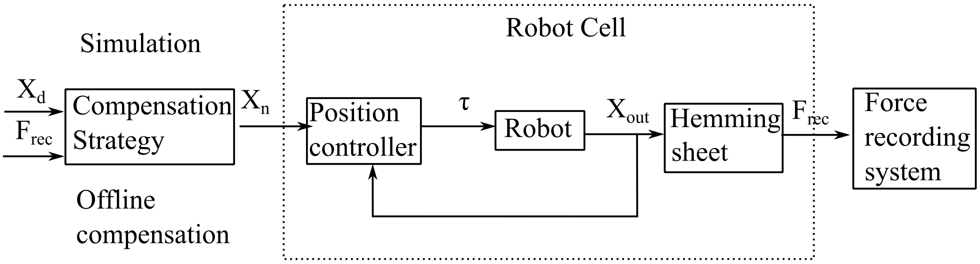

Fig. 1. *An offline compensation strategy based on the variable force of the process*

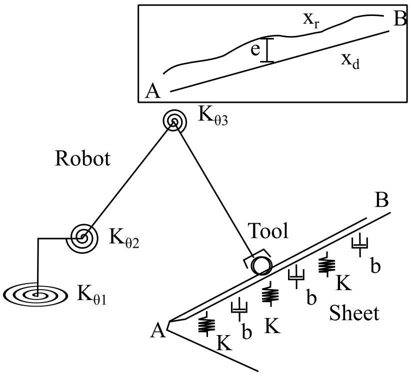

Fig. 2. *The model of the roll hemming process*

1 METHODS

1.1 A Trajectory Compensation Proposal

An offline compensation approach is defined in this paper. The Fig. 1 shows a trajectory compensation proposal related to the robot cell and the roll hemming process, where the desired position X_d and the recorded force F_{rec} are the inputs of the model. Once computed the new trajectory X_n, the position controller commands the robot toward the hemming process. The X_{out} represents the location's feedback.

The Fig. 2 shows the scheme of the process as the robot deforms the flange. The first three joints of the robot are modeled as torsional springs and the last three joints are used for orientation having a lower impact on the elasticity behavior. The sheet is modeled as linear spring with a damping effect. The tool center point (TCP) moves from position A to position B along its path but the material stiffness and the elasticity of the robot affect the desired trajectory X_d producing an error e in comparison with the real trajectory X_r.

A representative equation of the compensation strategy is

$$\begin{aligned} X_n &= X_d + e, \\ X_n &= X_d + \Delta_{robot} + \Delta_{sheet}, \end{aligned} \tag{1}$$

where e is the term of the error or deviation.

1.1.1 The Deviation Due to the Robot

This section describes the mathematical model to determine the deflection of the robot Δ_{robot}. The deflection vector has three terms for position and three for orientation due to the configuration and the stiffness of the robot. The general deflection equations are built from the stiffness in the Cartesian and joint spaces as

$$F = K_x \delta_x, \tau = K_\theta \delta_\theta, \tag{2}$$

where the vector F is the 6×1 vector of external forces and torques applied to the tool, the matrix K_x is the 6×6 Cartesian stiffness matrix, the vector δ_x is the 6×1 vector of linear and angular displacements, the vector τ is the 6×1 vector of joint torques, the matrix K_θ is the 6×6 joint stiffness matrix and the vector δ_θ is the 6×1 vector of joint displacements. Both displacements are related through the Jacobian relation

$$\delta_x = J(\Theta)\delta_\theta, \tag{3}$$

where the variable $J(\Theta)$ represents the 6×6 Jacobian matrix. By inserting this equation in Eq. (2) a new equation is obtained

$$\tau = K_\theta J^{-1}(\Theta)\delta_x, \tag{4}$$

this equation relates the two different spaces by the Jacobian matrix. Naming the principle of virtual work

$$F^T \delta_x = \tau^T \delta_\theta, \tag{5}$$

and combining this relation with Eq. (3) another equation is formed

$$\tau = J^T(\Theta)F, \tag{6}$$

which is similar to Eq. (3). Again, a substitution in Eq. (4) results in a new statement

$$J^T(\Theta)F = K_\theta J^{-1}(\Theta)\delta_x. \tag{7}$$

Table 1. *Denavit-Hartenberg parameters for the robot Fanuc 200IC*

i	α_{i-1}	a_{i-1}	d_i	θ_i
1	0	0	0	θ_1
2	$-\frac{\pi}{2}$	a_1	0	$\theta_2-\frac{\pi}{2}$
3	π	a_2	0	θ_3
4	$-\frac{\pi}{2}$	a_3	$-d_4$	θ_4
5	$\frac{\pi}{2}$	0	0	θ_5
6	$-\frac{\pi}{2}$	0	0	θ_6
T	0	0	$-d_t$	0

This last equation relates the force F and the displacement δ_x of the Cartesian space with the joint stiffness matrix. Expressing in explicit form

$$\Delta_{robot} = \delta_x = K_\theta^{-1} J(\Theta) J^T(\Theta) F^W. \qquad (8)$$

Observing this equation it is noted that the tool displacement depend on the force, the jacobian matrix and the joint stiffness matrix. The force and displacement are required to be expressed in the global reference frame. A general view of the last equation shows a similarity to Eq. (2) where forces and displacements are related through the Cartesian stiffness matrix.

1.1.2 The Kinematic Model of the Robot

The Fig. 3 shows the scheme of the robot with the reference frames attached to each joint and with 6 degrees of freedom. All the joints were considered as flexible and all the links as rigid bodies, the Table 1 shows the Denavit-Hartenberg parameters established for this robot, being $a_1 = 75$ mm, $a_2 = 300$ mm, $a_3 = 75$ mm, $d_1 = 330$ mm, $d_4 = 320$ mm, and the distance to the TCP $d_t = 80$ mm $+120$ mm, this parameters describe the kinematic behavior of the robot. The Jacobian matrix is proposed in order to relate the Cartesian displacement and the joint displacement as

$$J(\Theta) = \begin{pmatrix} J(\Theta)_1 & J(\Theta)_2 & J(\Theta)_3 \end{pmatrix}^T, \qquad (9)$$

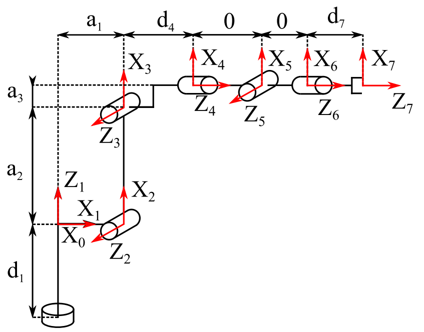

Fig. 3. *The scheme of the robot with the reference frames*

where each one of the terms is expressed as

$$J(\Theta)_1 = \begin{pmatrix} -sin(\theta_2+\theta_3)d_1 \\ sin(\theta_1+\theta_2) - cos(\theta_2+\theta_3)d_4 + sin\theta_2 a_2 - a_1 \\ cos(\theta_2+\theta_3)d_1 \end{pmatrix}. \qquad (10)$$

The second column corresponds to

$$J(\Theta)_2 = \begin{pmatrix} sin\theta_3 a_2 + d_4 \\ 0 \\ -cos\theta_3 a_2 - a_3 \end{pmatrix}, \qquad (11)$$

and the third column corresponds to

$$J(\Theta)_3 = \begin{pmatrix} d_4 \\ 0 \\ -a_3 \end{pmatrix}. \qquad (12)$$

This is the jacobian matrix considered for the deviation due to the robot.

1.1.3 A Method to Compute the Stiffness/Compliance of the Robot

This paper proposes to compute the joint stiffness matrix K_θ as a function of the vector of external forces and torques and the vector of linear and angular displacement expressed as

$$K_\theta = f(F, \delta_x). \qquad (13)$$

In order to obtain the last expression, the Eq. (8) is reordered in explicit form for the compliance vector as

$$\delta_x = \begin{pmatrix} \frac{1}{K_{\theta 1}}[\Sigma_{j=1}^6[J_{1j}(\Sigma_{i=1}^6 j_{ij}F_i)]] \\ \frac{1}{K_{\theta 2}}[\Sigma_{j=1}^6[J_{2j}(\Sigma_{i=1}^6 j_{ij}F_i)]] \\ \frac{1}{K_{\theta 3}}[\Sigma_{j=1}^6[J_{3j}(\Sigma_{i=1}^6 j_{ij}F_i)]] \\ \frac{1}{K_{\theta 4}}[\Sigma_{j=1}^6[J_{4j}(\Sigma_{i=1}^6 j_{ij}F_i)]] \\ \frac{1}{K_{\theta 5}}[\Sigma_{j=1}^6[J_{5j}(\Sigma_{i=1}^6 j_{ij}F_i)]] \\ \frac{1}{K_{\theta 6}}[\Sigma_{j=1}^6[J_{6j}(\Sigma_{i=1}^6 j_{ij}F_i)]] \end{pmatrix}, \qquad (14)$$

where the compliance matrix K_θ^{-1} has been integrated in the resultant vector of the displacement and substituted for the vector of compliance C

$$C = [\frac{1}{K_{\theta 1}} \frac{1}{K_{\theta 2}} \frac{1}{K_{\theta 3}} \frac{1}{K_{\theta 4}} \frac{1}{K_{\theta 5}} \frac{1}{K_{\theta 6}}], \qquad (15)$$

it is possible to present the Eq. (14) in the form

$$\delta_x = AC, \qquad (16)$$

where A is formed by the Jacobian and force terms. This equation is expressed as a linear matrix equation $Ax = b$ where the unknown values are those of the vector of compliance C. If $AC = \delta_x$ has no solution

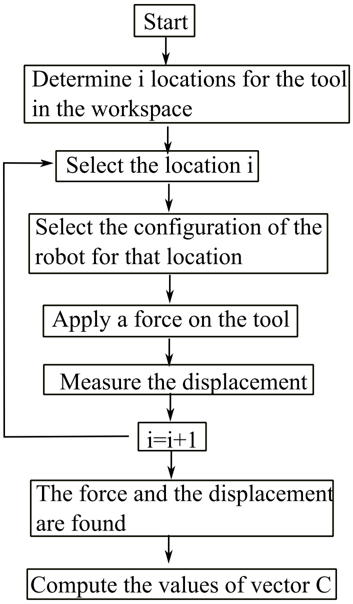

Fig. 4. *The flow chart to find the values of the compliance*

by finding A^{-1}, then we can find the minimum error $e = AC - \delta_x$ by the least square solution

$$C_0 = (A^T A)^{-1} A^T \delta_x, \tag{17}$$

where the vector of compliance C_0 relates every joint deflection to a specific torque. The precision of the compliance vector is related to the measurement of the forces and displacements of the tool. The Fig. 4 illustrates the procedure to determine the values of the compliance where the first steps is to determine the location i of the work-space to test the values of displacements and forces, the second step is to select a specific location for which the robot takes the specific configuration to reach that location, once in that configuration a specific force is applied on the tool and the displacements are measured, the procedure is repeated until covering the work-space and finally the Eq. (17) computes the values in a numerical software.

1.1.4 The Deviation Due to the Panel

The deviation due to the panel can be computed as

$$\Delta_{sheet} = \Delta_{ep} + \Delta_{wrinkling}, \tag{18}$$

where the total deflection of the sheet's flange Δ_{sheet} is the sum of the elastic and plastic deformation Δ_{ep} and the deformation due to the wrinkling defect $\Delta_{wrinkling}$ produced from the waves of the flange. This model gives a contribution to the common finite element models presented in the roll hemming overview. The Fig. 5 shows how the external force F, a scalar

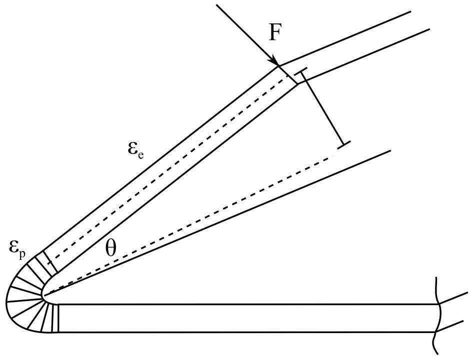

Fig. 5. *The material deformation scheme*

value for the panel, generates the plastic ε_p and elastic ε_e deformations as the flange inclines the angular position θ. This scheme can be modeled in the form $\varepsilon = \varepsilon_e + \varepsilon_p$ where the total deformation of the sheet ε is the sum of the elastic ε_e and the plastic ε_p deformation. The elastic deformation ε_e may be computed by considering the flange as a beam under bending load at the end for a specific section of the material. To model this deflection two relations are considered

$$1/R = \frac{M}{EI_z}, \quad \sigma = \frac{My}{I_z}, \tag{19}$$

where R is the radius of curvature, M is the bending moment, E is the Young's modulus, I_z is the second moment of area, σ is the stress of the beam and y is the distance from the neutral middle line on the beam towards the external fibers. The use of these two equations results in the deflection function

$$\delta_e = \frac{Fx^2(x-3l)}{6EI_z}, \tag{20}$$

where F is the load at the end of the flange, x is the distance at any given section of the flange, and l is the total length of the flange. If it is considered the distance $x = l$ for deflection, then the Eq. (20) becomes

$$\delta_e = -\frac{Fl^3}{3EI_z} = \frac{Yl^2}{3Eh}, \tag{21}$$

which states the deflection for the elastic part of the material at the end of a beam, where Y is the yield stress and h is the total height of the cross section from the neutral line to the external fiber.

Chakrabarty established that the longitudinal strain in a elastic beam is $\varepsilon_x = y/R$ and the transverse strains are $\varepsilon_y = \varepsilon_z = -\nu y/R$, where ν is the Poisson's ratio [6]. By using these relations the deflection v on

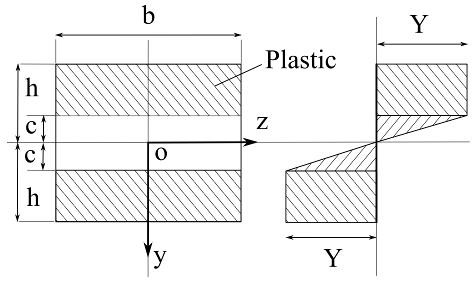

Fig. 6. *The plastic deformation on the rectangular cross section*

the y axis is established as

$$v = \frac{x^2 + \nu(y^2 - z^2)}{2R}. \quad (22)$$

The Fig. 6 shows the rectangular cross section during plastic deformation assuming an elastic, perfectly plastic behavior, where b is the width of the section. The bending moment M_e and the radius of curvature R_e at the elastic limit are established in view of Eq. (19) using an area moment of inertia $I_z = \frac{2bh^3}{3}$ at the initial yielding stress when $y = h$

$$M_e = \frac{2bh^2Y}{3}, \quad R_e = \frac{Eh}{Y}, \quad R = \frac{Ec}{Y}, \quad (23)$$

where R is the radius of curvature at any stage during the elastic/plastic bending. Then according to the material strain-hardening

$$\frac{\sigma}{Y} = (\frac{E\varepsilon}{Y})^n, \quad (24)$$

where $0 \leq n \leq 1$, n being the strain hardening exponent, and with the condition $\varepsilon \geq Y/E$. By considering that $\varepsilon = y/R$

$$\sigma = \begin{cases} Y(\frac{y}{c}), & 0 \leq y \leq c \\ Y(\frac{y}{c})^n, & c \leq y \leq h \end{cases}. \quad (25)$$

The bending moment at any stage of the plastic deformation is

$$M = 2b\int_0^h \sigma y dy. \quad (26)$$

By substituting Eq. (25) into Eq. (26) and integrating we obtain

$$\frac{M}{M_e} = \frac{1}{2+n}[3(\frac{R_e}{R})^n - (1-n)(\frac{R}{R_e})^2]. \quad (27)$$

The above equation applies for a non hardening material when $n = 0$ obtaining

$$\frac{R_e}{R} = \begin{cases} \frac{M}{M_e}, & M \leq M_e \\ (3 - 2\frac{M}{M_e})^{-1/2}, & M \geq M_e \end{cases}. \quad (28)$$

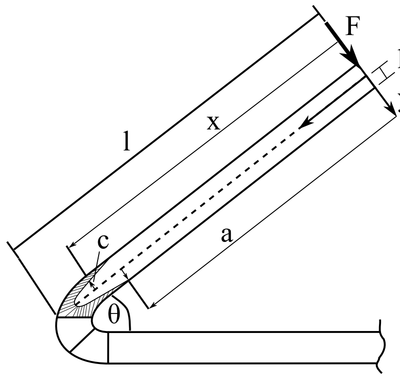

Fig. 7. *The plastic deformation model.*

Considering the second partial derivative of Eq. (22) respect to x we obtain

$$\frac{1}{R} = -\frac{\partial^2 v}{\partial x^2}. \quad (29)$$

The Fig. 7 illustrates a frontal view of the flange as a cantiliver beam with a terminal load, where l is the total length of the flange and θ is the inclination angle. This assumption involves the following relations

$$\frac{F_e}{F} = \frac{a}{l}, \quad \frac{M}{M_e} = -\frac{x}{l}, \quad (30)$$

where F_e is the load at the elastic/plastic boundary, a is the distance to the elastic/plastic boundary and M_e is the bending moment at the elastic/plastic boundary. By inserting Eq. (29) and Eq. (30) into the Eq. (28) we obtain

$$R_e\frac{\partial^2 v}{\partial x^2} = \begin{cases} (3 - 2\frac{x}{a})^{-1/2}, & x \geq a \\ \frac{x}{a}, & x \leq a \end{cases}. \quad (31)$$

for the case where $a \leq x \leq l$, we integrate the equation, knowing that $\partial v/\partial x$ vanishes when $x = l$ as a boundary condition, resulting

$$\frac{\partial v}{\partial x} = -\frac{a}{R_e}[\sqrt{3 - 2\frac{x}{a}} - \sqrt{3 - 2\frac{l}{a}}]. \quad (32)$$

The equation is integrated again applying the same boundary condition, the deflection v vanishes at $x = l$ obtaining

$$v = \frac{a^2}{3R_e}[(3 - \frac{2x}{a})^{3/2} - (3 + \frac{l - 3x}{a})\sqrt{3 - \frac{2l}{a}}]. \quad (33)$$

The Eq. (31) of limits $0 \leq x \leq a$ is integrated considering that $\partial v/\partial x$ is continuous across $x = a$, and we obtained

$$\frac{\partial v}{\partial x} = -\frac{a}{R_e}[\frac{1}{2}(3 - \frac{x^2}{a^2}) - \sqrt{3 - \frac{2l}{a}}]. \quad (34)$$

Integrating again this equation and considering that v is continuous across $x = a$ we obtain

$$v = \frac{a^2}{3R_e}[5 - \frac{x}{2a}(9 - \frac{x^2}{a^2}) - (3 + \frac{l-3x}{a})\sqrt{3 - \frac{2l}{a}}]. \quad (35)$$

The last equation represents the deflection at any distance x of the flange due to the plastic conditions. Knowing that

$$\delta_e = \frac{Yl^2}{3Eh} = \frac{l^2}{3R_e}, \quad (36)$$

and multiplying the left side of the Eq. (35) for the unity l^2/l^2, then the term δ_e appears in the equation.

$$v = \frac{a^2}{l^2}[5 - \frac{x}{2a}(9 - \frac{x^2}{a^2}) - (3 + \frac{l-3x}{a})\sqrt{3 - \frac{2l}{a}}]\delta_e. \quad (37)$$

If we apply $x = 0$ to the corresponding equation and considering the load (at the end of the deflection) then

$$\Delta_{ep} = v = (\frac{F_e}{F})^2[5 - (3 + \frac{F}{F_e})\sqrt{3 - \frac{2F}{F_e}}]\delta_e. \quad (38)$$

This equation contains the elastic/plastic deflection. By substituting the Eq. (21) into the last one, a new expression is obtained

$$\Delta_{ep} = -(\frac{F_e}{F})^2[5 - (3 + \frac{F}{F_e})\sqrt{3 - \frac{2F}{F_e}}]\frac{Fl^3}{3EI}. \quad (39)$$

The deflection is presented respect to the z axis of the tool reference frame. This relation expresses the first term of the Eq. (18).

A form to represent the wrinkling deviation $\Delta_{wrinkling}$ is the frequency model that relates the speed of the roller with the deflection in the form of

$$\Delta_{wrinkling} = Bsin(wt), \quad (40)$$

where B is the parameter of amplitude for the displacement, w is the number of waves and t is the time of the function. Considering $t = l_s/r_x$ the equation takes the form

$$\Delta_{wrinkling} = Bsin(w\frac{l_s}{r_x}), \quad (41)$$

where l_s is the length of the material sheet and the r_x is the speed of the roller over the material.

In the Eq. (41), the definition of B gives the error for the specific defect presented here. As a conclusion for the section, the deviation due to the panel for Eq. (18) takes the form of

$$\begin{aligned}\Delta_{sheet} = &-(\frac{F_e}{F})^2[5 - (3 + \frac{F}{F_e})\sqrt{3 - \frac{2F}{F_e}}]\frac{Fl^3}{3EI}, \\ &+ Bsin(w\frac{l_s}{r_x})\end{aligned} \quad (42)$$

completing the model for deformation due to the panel.

1.2 The Trajectory Compensation Model

By integrating the deviation due to the robot and the deviation due to the panel into the Eq. (1), the complete model would take the form of

$$\begin{aligned}X_n^W =& X_d^W \\ &+ K_\theta^{-1}J(\Theta)J^T(\Theta)F^W \\ &+ R_T^W\{\hat{Z}\{-(\frac{F_e}{F})^2[5 - (3 + \frac{F}{F_e})\sqrt{3 - \frac{2F}{F_e}}]\frac{F^T l^3}{3EI}\}\}, \\ &+ Bsin(w\frac{l_s}{r_x})\end{aligned} \quad (43)$$

where R_T^W is the transformation matrix form the tool reference frame to the world reference frame and the $\hat{Z}$ indicates the force is acting only in that component.

2 EXPERIMENTAL

2.1 The Stiffness/Compliance of the Robot

In order to compute the joint stiffness matrix k_θ the joint stiffness values are model as functions of force and displacement.

The proposal of the experiment consists in evaluating two different positions with the same value for Y and Z axis and different for X axis like the Fig. 8 shows, where the robot holds the roll hemming tool with a force sensor and two locations P_1 and P_2 are selected. In the two positions the intensity of the induced force in the Z axis direction was changed according to the Table 2, the force was varied from 20 N to 120 N in different sub-steps.

The Fig. 9 shows an instrument to apply an external load on the tool, where the Z in the reference

Table 2. *Parameters of the experiment*

Position [mm]	Run	Force [N]
$x = 660$	1	20
$y = 0$	2	40
$z = -350$	3	60
	4	80
	5	100
	6	120
$x = 425$	7	20
$y = 0$	8	40
$z = -350$	9	60
	10	80
	11	100
	12	120

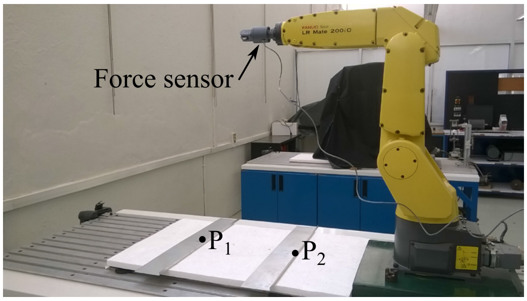

Fig. 8. *The robot and two work space location for different stiffness performance*

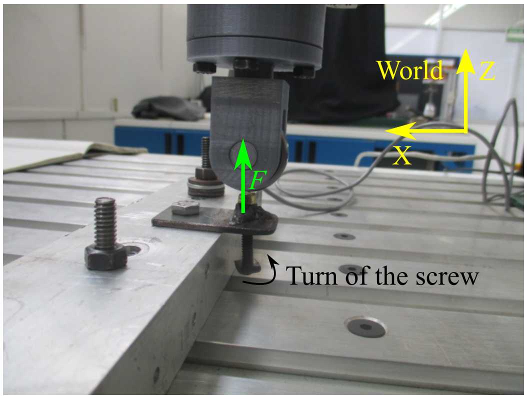

Fig. 9. *An instrument to apply an external force incrementally*

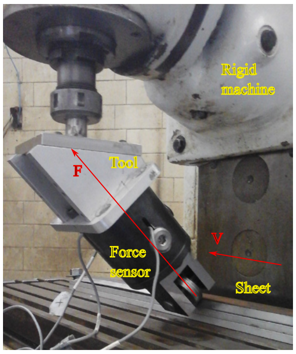

(a)

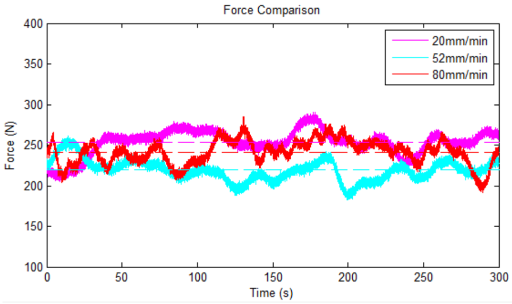

(b)

Fig. 10. *The roll hemming tests; a) The experimental set up, b) The forces measured in the tests*

frame corresponds to the direction of the force, this instrument increments a specific force accordingly to the displacement obtained from the turn of the screw, the distance is controlled and the force was applied in the TCP Z axis global direction.

2.2 The Tests of Deformation of the Panel

The experiment determines the process forces using a milling machine to avoid the compliance of the robot. One pre-hemming step at different low and high constant speeds was implemented. The Fig. 10(a) illustrates the tool end effector attached to the milling machine. The tool is at 45° in order to apply the first pre-hemming step along the flange, the milling machine is considered as a rigid machine with infinite stiffness and the sheet is fixed and constrained in its movement, the force sensor in the tool that measures the signals during the tests is observed in the figure. The material for the panel sheet was aluminum 6000 series, the angle of the pre-hemming step was 45°, the length of the panel was 60 mm, the force was measured in the Z axis of the tool end effector at different constant speeds.

The reported values of the forces were 200 N to 300 N which agrees well for a pre-hemming step. In the graph in Fig. 10(b), the force varies at different speeds due to material fluctuations. Three different data are observed, one for the speed at 20 mm/min, other at 52 mm/min and the last graph at 80 mm/min, all these graphs were taken at the same pre-hemming step and different averages are observed, which means that the initial set up of the sheet was different for every one, also the graphs present different fluctuation patterns corresponding to the material deformation.

2.3 The Roll Hemming Set Up

The robot Fanuc 200IC with capacity of 200 N of payload in the tool was implemented for the experiment and the simulation, it is an industrial serial robot with 6 joints (6R). This robot is useful for tests at small scale since the reduced parameters allow it for easy and practical implementations.

The Fig. 11 shows the roll hemming tool in the upper part of the plot with the reference frame according to the tool frame and attached to the robot, it has a sensor to measure the force. In the bottom of the plot it is observed the frame attached to the metal

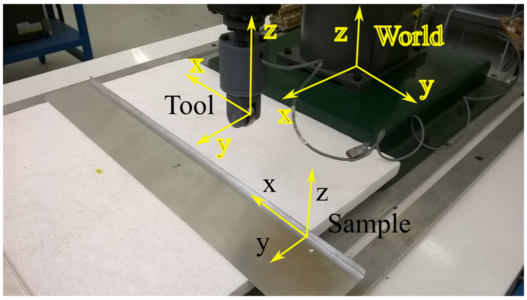

Fig. 11. *The reference frames in the tool and the sample sheet*

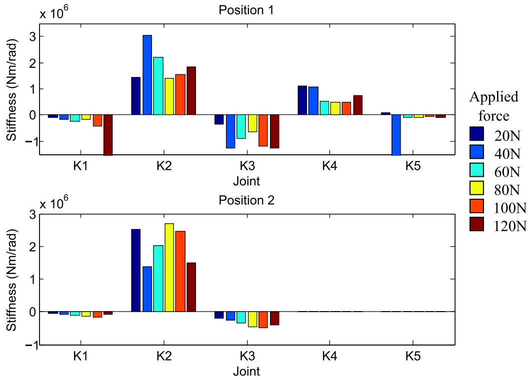

Fig. 12. *The joint stiffness values computed for each joint*

Table 3. *The trajectory of the robot*

Run	Position [mm]
	$Y = 0$ $Z = -326.319$
	X
1	425
2	451
3	477
4	503
5	529
6	555
7	581
8	607
9	633
10	660

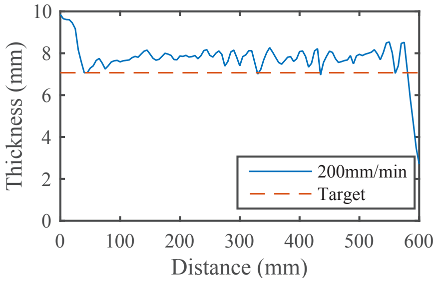

Fig. 13. *The wrinkling defect at 200 mm/min*

sheet and with the X component coincident to the tool frame. The global frame that is attached to the base of the robot is also shown in the picture, according to this global reference frame the compensation strategy should work during the analysis of deviation.

The Table 3 shows the different location in the X coordinate that were considered for the simulation, in this case the values of Y and Z coordinates remained constant and a total of ten points were obtained, for the simulation a force is applied in direction to the Z global reference coordinate.

3 RESULTS

According to section 2.1. The graph of Fig. 12 plots the stiffness calculation giving positive and negative values, those negative values result from the direction of displacements and the Jacobian configuration; there is no value of K_6 displayed in the figure, for this experiment all the K_6 are infinite due to the force is acting in the Z axis direction impeding its rotation. Also as we can observe from the figure the values of K_1 in the sixth run and K_2 in the second run overpass the graph scale, the two values are considered as atypical data. The values of all the runs, except the two atypical data, were averaged to result in the values of the Table 4. According to section 2.2. The Fig. 13 plots the graph of thickness and the distance along the sheet over the edge, the speed of the roll hemming was 200 mm/min which represents a high speed for the process, in the figure it is observed that the wrinkling defect appear in high frequency and the error of the path and the target path is high. This means that the wrinkling defect has a direct relation with the speed of the process increasing the error and deviating the trajectory along the edge of the sheet.

The graph in Fig. 14 shows the result of the compensation strategy considering a constant force applied to the tool end effector. At the initial position of the tool the distance is positive and as the roller moves in x direction the trajectory goes down until the value of the position in z is negative, this may be because the compensations considering the deviation of the tool due to the low stiffness and the configuration of the robot. This graph shows that at the end of the trajectory the value of the trajectory could be under the desired position. The force applied is considered as constant and the value of the deviation is around the 4×10^{-3} mm which is a low value in comparison with the location of the tool and the work-space.

Table 4. *The average of the stiffness values*

Joint 1	Mean stiffness [Nm/rad]
1	-0.160×10^6
2	2.001×10^6
3	-0.651×10^6
4	0.370×10^6
5	-0.020×10^6
6	inf

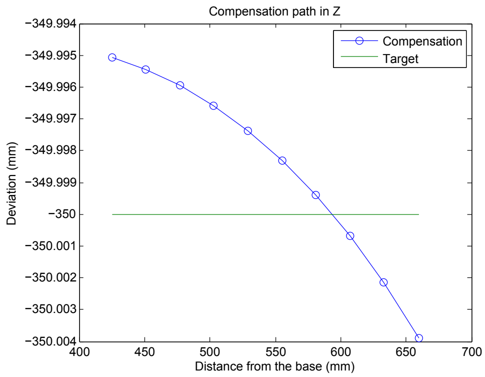

Fig. 14. *Deviation in Z constant force*

The Fig. 15 shows the trajectory after the compensation is implemented considering a variable force applied in the robot, it is observed that as the roller moves over the sheet the trajectory goes to the negative values this is because the stiffness in that point is low, the difference with the graph shown before is that this compensation trajectory considers the wrinkling defect of the material since the values of the force were obtained from the experimental behavior of the panel.

The Fig. 16 shows the thickness of the tested samples as a function of the distance along the flange. In the figure, the reference is at 1 mm of thickness due to the flange thickness is 0.5 mm and the pre-hemming steps were 45° and 0°. The trajectory without compensation appears slightly over the reference with a maximum thickness of 3.1 mm and the trajectory with the compensation appears closer to the reference with a maximum thickness of 2.8 mm.

4 DISCUSSIONS

The range of the error for the compensation strategy is 1×10^{-3} mm, so the robot characteristics should meet this requirement. For example, the Fanuc 200IC accuracy for the TCP location is 1×10^{-2} mm. Which means that this robot finds out limitations to implement

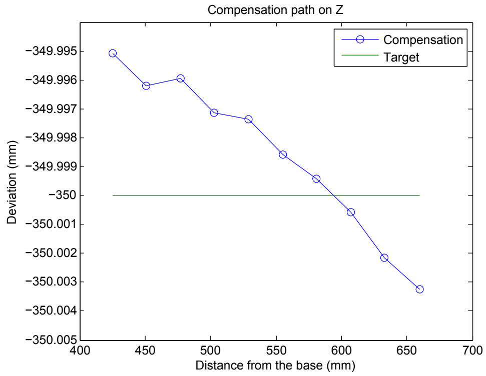

Fig. 15. *Deviation in Z with variable force*

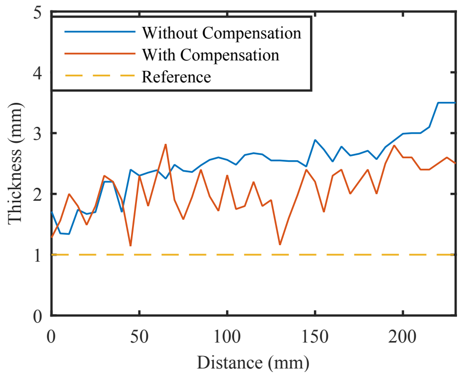

Fig. 16. *The thickness of the sample sheets*

this compensation strategy. Also, the accuracy of the previous process to the roll hemming will define the effectiveness of the compensation model. These graph results of Fig. 16 agree well compared to those of Posada et al. [7] where the translation errors were smaller than 0.1 mm. Posada et al. implemented a sensor-based stiffness compensation model instead of a model-based. He discussed that the sensor-based proposal, which takes the real values, ensures better results than a model-based system, which predicts via simulation.

In contrast, the experimental results of Kamali et al. [8] revealed the proposed elasto-geometrical calibration approach of the TCP is able to reduce the maximum position error to 0.960 mm. Such results agree well to the simulation results when the compensation method is implemented.

Hu et al. [9] developed a method to calculate the fracture limits of the material by developing several tests on the material fibers but a relation between the material properties and the robot parameters is not presented. LeMaout et al. [10] focused on the finite element analysis for pre-strain materials in roll hemming process. One of the focuses was to deal with the complex geometries of the panels. The authors of this paper want to encourage similar works looking for improvements to the material analysis and the FEM solutions by relating the robot parameters.

The works framed by Kohrt et al. [11] on posture optimization may be enriched by the results presented in this paper. The present paper may be cited by future works of roll hemming applications since the authors have been working on such topics [12].

5 CONCLUSIONS

This paper established the main problems of roll hemming process and an offline compensation strategy based on the variant force. The compensation proposal integrated a method to determine the deviation due to the robot and the deviation due to the panel. An improvement of 1 mm was observed from the results. The authors of this paper believe that if this model is enhanced and implemented in the industry, it may bring a complete solution for the roll hemming technology since the simulation with the experimental data showed good tendency in the correction of the trajectory during the process. Future works will consider: the previous internal strains of the material, the FEM simulation and a sensibility analysis of the variables.

6 ACKNOWLEDGEMENTS

The first author wishes to gratefully acknowledge Universidad Autónoma de Querétaro through grant scholarship of Conacyt (Consejo Nacional de Ciencia y Tecnología) for permitting his period of study at LaRM of Cassino University in the year 2016 within a double PhD degree program.

7 REFERENCES

[1] Guillo, M., Dubourg, L. (2016). Impact & improvement of tool deviation in friction stir welding: Weld quality & real-time compensation on an industrial robot. *Robotics and Computer-Integrated Manufacturing*, vol. 39, p. 22-31, **DOI:10.1016/j.rcim.2015.11.001**.

[2] Thuillier, S., Le Maoût, N., Manach, P.Y., Debois, D. (2008). Numerical simulation of the roll hemming process. *Journal of Materials Processing Technology,* vol. 198, no. 1-3, p. 226–233, **DOI:10.1016/j.jmatprotec.2007.07.004**.

[3] Zhang, H., Wang, J., Zhang, G., Gan, Z., Pan, Z., Cui, H., Zhu, Z. (2005). Machining with flexible manipulator: toward improving robotic machining performance. *Proceedings of IEEE/ASME International Conference on Advanced Intelligent Mechatronics*, p. 1127-1132, **DOI:10.1109/AIM.2005.1511161**.

[4] Le Maoût, N., Manach, P.Y., Thuillier, S. (2012). Influence of prestrain on the numerical simulation of the roller hemming process. *Journal of Materials Processing Technology*, vol. 212, no. 2, p. 450-457. **DOI:10.1016/j.jmatprotec.2011.10.008**.

[5] Drossel, W.-G., Pfeifer, M., Findeisen, M., Rössinger, M., Eckert, A., Barth, D. (2014). The influence of the robot's stiffness on roller hemming processes. *45th International Symposium on Robotics*, p. 531–538.

[6] Chakrabarty, J. (2006). *Theory of Plasticity, 3rd Edition*, Butterworth-Heinemann Elsevier, Oxford, .

[7] Diaz Posada, J.R., Schneider, U., Pidan, S., Geravand, M., Stelzer, P., Verl, A. (2016). High accurate robotic drilling with external sensor and compliance model-based compensation. *Proceedings of IEEE International Conference on Robotics and Automation,* p. 3901–3907. **DOI:10.1109/ICRA.2016.7487579**.

[8] Kamali, K., Joubair, A., Bonev, I.A., Bigras, P. (2016). Elasto-geometrical calibration of an industrial robot under multidirectional external loads using a laser tracker. *Proceedings of IEEE International Conference on Robotics and Automation*, p. 4320–4327, **DOI:10.1109/ICRA.2016.7487630**.

[9] Hu, X., Zhao, Y., Huang, S., Li, S., Lin, Z. (2012). Numerical analysis of the roller hemming process. *The International Journal of Advanced Manufacturing Technology,* vol. 62, no. 5-8, p. 543–550, **DOI:10.1007/s00170-011-3822-4**.

[10] Le Maoût, N., Thuillier, S., Manach, P.Y. (2010). Classical and roll-hemming processes of pre-strained metallic sheets. *Experimental Mechanics*, vol. 50, no. 7, p. 1087-1097, **DOI:10.1007/s11340-009-9297-7**.

[11] Kohrt, C., Stamp, R., Pipe, A.G., Kiely, J., Schiedermeier, G. (2013). An online robot trajectory planning and programming support system for industrial use. *Robotics and Computer-Integrated Manufacturing*, vol. 29, no. 1, p. 71-79, **DOI:10.1016/j.rcim.2012.07.010**.

[12] Esquivel, E., Carbone, G., Ceccarelli, M., Jáuregui, J. (2017). Requirements and constraints for a robotized roll hemming solution. *RAAD 2016: Advances in Robot Design and Intelligent Control*, Springer, Cham, p. 244-251, **DOI:10.1007/978-3-319-49058-8_27**.

Vsebina

Strojniški vestnik - Journal of Mechanical Engineering
letnik 64, (2018), številka 6
Ljubljana, junij 2018
ISSN 0039-2480

Izhaja mesečno

Razširjeni povzetki (extended abstracts)

Strojniški vestnik - Journal of Mechanical Engineering 64(2018)6, SI 53

Prejeto v recenzijo: 2017-12-29
Prejeto popravljeno: 2018-03-15
Odobreno za objavo: 2018-04-11

Modeliranje in napovedovanje podajalne sile in momenta pri vrtanju v material Al7075 po metodah ANN in RSM

Nikolaos Efkolidis[1,*] – César García Hernández[1] – José Luis Huertas Talón[1] – Panagiotis Kyratsis[2]
[1] Univerza v Zaragozi, Oddelek za konstruiranje in proizvodno strojništvo, Španija
[2] Univerza za aplikativne vede Zahodne Makadonije, Oddelek za strojništvo in industrijski dizajn, Grčija

Vrtanje spada med osnovne postopke obdelave z odvzemanjem materiala in zaradi njegove razširjenosti lahko vsaka optimizacija parametrov procesa pripomore k izboljšanju učinkovitosti trajnostne proizvodnje in k bolj zeleni obdelavi. Tehnologija rezalnih orodij je eden najpomembnejših vplivnih dejavnikov trajnostnosti obdelovalnih procesov in sistemov. Uporabniki CNC-strojev so pri obdelavi materialov za posebne aplikacije v letalski in vesoljski ter kemični industriji, kot je aluminijeva zlitina 7075, pogosto v dvomih glede izbire najprimernejših rezalnih parametrov za razpoložljivo rezalno orodje. Optimalna izkoriščenost rezalnih orodij je zanje ključnega pomena, saj lahko vpliva na celoten proizvodni proces tako glede ekonomike kot na področju varstva okolja.

V pričujoči študiji so bili raziskani vplivi rezalnih parametrov (rezalna hitrost, podajanje) in premera orodja na podajalno silo (*Fz*) in rezalni moment (*Mz*) pri vrtanju lukenj v obdelovance iz materiala Al7075 z orodji iz polne karbidne trdine. Opravljen je bil popoln nabor testov za vse kombinacije rezalne hitrosti, podajanja in premera orodja. Za napovedovanje podajalne sile in rezalnega momenta pri vrtanju lukenj v Al7075 sta bili uporabljeni tehniki modeliranja po metodologiji odzivne površine (RSM) in z umetnimi nevronskimi mrežami (ANN). Razviti modeli so se izkazali za zelo točne pri napovedovanju vrednosti *Fz* in *Mz* v razponu obravnavanih parametrov.

S povečevanjem premera se po pričakovanjih povečujeta tudi podajalna sila in rezalni moment. Enako velja tudi za povečevanje podajalne sile in rezalnega momenta s povečevanjem podajanja. Spreminjanje rezalne hitrosti po drugi strani nima večjega vpliva na eksperimentalne vrednosti. Vpliv premera rezalnega orodja in podajanja na podajalno silo in rezalni moment je bistveno večji od vpliva rezalne hitrosti.

Opravljena je bila primerjava modelov na osnovi RSM in ANN, kjer se je izkazalo, da je s predlaganimi modeli mogoče dobro napovedovati podajalno silo (*Fz*) in moment (*Mz*). Napoved rezultatov z modeli ANN je bila točnejša kot z modeli RSM: pri modelih ANN je bila ugotovljena točnost podajalne sile in momenta 2,18 % oz. 3,15 %, pri modelu RSM pa 3 % oz. 5,6 %. Sledi sklep, da sta obe strategiji primerni za modeliranje in napovedovanje podajalne sile in momenta pri vrtanju, metoda ANN pa je nekoliko točnejša od metode RSM.

Raziskava je jasno pokazala, da modeli za napovedovanje ustrezno opisujejo razmerja med neodvisnimi spremenljivkami, podajalno silo in rezalnim momentom. Raziskovalci in inženirji v industriji bodo lahko v okviru postavljenih omejitev izkoristili predstavljene matematične modele za napovedovanje podajalne sile in momenta z visoko stopnjo zaupanja. Glede na pregled literature predstavlja napovedovanje vrednosti podajalne sile (*Fz*) in rezalnega momenta (*Mz*) pri vrtanju v material Al7075 ter eksperimentiranje z različnimi premeri rezalnega orodja (8 mm, 10 mm, 12 mm in 14 mm), podajanji (0,2 mm/vrt., 0,4 mm/vrt. in 0,6 mm/vrt.) in rezalnimi hitrostmi (10 m/min, 40 m/min in 70 m/min) nov, kombiniran eksperimentalni pristop.
Ključne besede: trajnostna proizvodnja, Al7075, umetne nevronske mreže, metodologija odzivne površine, podajalna sila, moment

*Naslov avtorja za dopisovanje: Univerza v Zaragozi, Oddelek za konstruiranje in proizvodno strojništvo, Španija. efkolidi@unizar.es

Strojniški vestnik - Journal of Mechanical Engineering 64(2018)6, SI 54

Prejeto v recenzijo: 2017-11-25
Prejeto popravljeno: 2018-03-10
Odobreno za objavo: 2018-03-28

Metodika konstruiranja linijskih zobnikov s koplanarnimi osmi in nadzorovano drsno stopnjo

Yangzhi Chen – Zheng Li – Xiongdun Xie – Yueling Lyu*
Tehniška univerza Južne Kitajske, Kitajska

Linijske zobniške dvojice (LG) so nova vrsta zobniških mehanizmov s točkovnim stikom, zasnovanih na podlagi teorije prostorskih ubirnic. V članku je predstavljena metodika konstruiranja linijskih zobniških dvojic s koplanarnima osema in nadzorovano drsno stopnjo.

Kontaktna krivulja zobniške dvojice LG s koplanarnima osema je bila na podlagi diferencialne geometrije, teorije prostorskih ubirnic, numeričnih metod in eksperimentalnih meritev razširjena s krožne vijačnice na konično vijačnico s spremenljivim kotom stožca. Podan je predlog za novo vrsto linijskega zoba s kontaktno krivuljo na obeh straneh, ki omogoča prenos v smeri naprej in nazaj brez zračnosti. Površina zoba je oblikovana z gibanjem običajnega profila vzdolž kontaktne krivulje in pomožne krivulje debeline zoba. Izpeljane so formule kontaktnih krivulj, pomožnih krivulj debeline in prostorskih cilindričnih površin novega zoba, ki oblikujejo teoretično osnovo za standardizacijo industrijske proizvodnje zobniških dvojic LG. Izračuni z dvojicami LG kažejo, da je drsno stopnjo mogoče zmanjšati s kontaktno krivuljo v obliki konične vijačnice.

Preizkusne dvojice LG so bile izdelane po stereolitografskem postopku 3D-tiskanja (SLA) in nato je bila na eksperimentalni platformi preizkušena njihova kinematika. Rezultati kažejo, da trenutno prestavno razmerje niha okrog projektirane teoretične vrednosti, relativna napaka pa je manjša od 0,01 %. Največja trenutna relativna napaka pri vrtenju naprej/nazaj je bila 0,314 % oz. 0,389 %. Rezultati eksperimentalnega preizkusa kinematike vodijo do sklepa, da je dvojica LG, zasnovana po predlagani metodiki, zmožna prenosa v dveh smereh brez zračnosti in z nadzorovano drsno stopnjo.

V prihodnjih raziskavah bo mogoče preučiti še kriterije za izbiro geometrijskih parametrov, eksperimentalne metode za merjenje drsne stopnje, kriterije odpovedi, upogibno in kontaktno trdnost, izkoristek prenosnika itd.
Ključne besede: linijski zobnik, drsna stopnja, kontaktna krivulja, površina zoba, brez zračnosti, prenos naprej in nazaj

*Naslov avtorja za dopisovanje: Tehniška univerza Južne Kitajske, Guangzhou, Kitajska, lvyl88@scut.edu.cn

Strojniški vestnik - Journal of Mechanical Engineering 64(2018)6, SI 55

Prejeto v recenzijo: 2017-11-30
Prejeto popravljeno: 2018-03-18
Odobreno za objavo: 2018-04-16

Konstruiranje komponent iz feritno-perlitne nodularne litine s površinskimi diskontinuitetami za utrujanje

Márton Gróza* – Károly Váradi
Univerza za tehniko in ekonomijo v Budimpešti, Oddelek za konstruiranje strojev in izdelkov, Madžarska

Cilj predstavljene raziskave je razvoj metodologije zagotavljanja kakovosti za kontrolo površinskih napak pri varnostno pomembnih ulitkih, kot so deli železniških zavornih sistemov. Na trajno dinamično trdnost nodularne litine močno vpliva populacija napak v materialu. Proces utrujanja se običajno začne pri napakah na površini ali v bližini površine (velika hrapavost, votline, vključki peska, lunkerji, oksidi). Upoštevanje realnih lastnosti materiala (npr. površinskih diskontinuitet) pri vrednotenju utrujanja je zelo pomembno za zanesljivost obratovanja in ekonomično proizvodnjo.

Visokociklične utrujenostne lastnosti materiala brez napak za enoosno obremenitveno stanje so opisane s preprostim in uveljavljenim modificiranim Goodmanovim pristopom. Trajna dinamična trdnost kot funkcija velikosti napak na mestu iniciacije razpoke (Kitagawovo razmerje) je modelirana z različnimi metodami: s pristopom gradienta napetosti napake, po Murakamiju, z linearno elastično lomno mehaniko in na osnovi efektivnega praga napredovanja razpoke. Primerjava rezultatov simulacij in rezultati eksperimentov so podani v Kitagawovih diagramih in v obliki kart dovoljene velikosti napak, izrisanih v postprocesorju FEA (analiza po metodi končnih elementov).

Smernice za kontrolo so bile izpeljane iz rezultatov analize po MKE in dodatnih izračunov na osnovi mehanike kontinuuma in lomov, v katerih je bila določena največja dovoljena ekvivalentna velikost napake za vsako točko na površini komponente.

Opravljeni so bili utrujenostni preizkusi za analizo raztrosa utrujenostnih lastnosti materiala v kvaliteti po ISO1083/JS/500-7 NCI. Pri poliranih vzorcih različnih komponent iz nodularne litine 500-7 je bila ugotovljena do 40-odstotna razlika v trajni dinamični trdnosti. Za primerjavo metod na predvidenem področju uporabe so bile izrisane karte dovoljene velikosti površinskih napak za preprost analitični premer. Površinske diskontinuitete velikostnega reda 1000 μm lahko zmanjšajo trajno dinamično trdnost nodularne litine za faktor 2,5 (poloblaste napake v cilindričnih preskušancih pri natezno-tlačni obremenitvi tipa R-1 [1]). Pristop gradienta napetosti napak modelira večosno utrujenostno vedenje materialov brez napak in z napakami v območju visokocikličnega utrujanja, zato je bolj splošen od ostalih analiziranih metod.

Uporaba predlaganega pristopa (oz. najbolj splošnega pristopa gradienta napetosti napak) je omejena na proporcionalno večosno visokociklično utrujanje in na kovinske materiale, pri katerih v visokociklični utrujenostni trajnostni dobi prevladuje faza iniciacije razpoke. Avtorji so prepričani, da razvoj tovrstnih metod ne bi smel biti usmerjen zgolj v iskanje determinističnih rezultatov, ampak bi se moral posluževati tudi probabilističnega pristopa.

V članku so podani novi podatki o utrujenostnih preizkusih nodularne litine ISO1083/JS/500-7. Objavljeni so tudi rezultati za preskušance s kompleksnimi umetnimi površinskimi napakami pri različnih obremenitvah. Takšni podatki so redki in dragoceni. Primerjane so različne metode za opisovanje vpliva površinskih diskontinuitet na zmanjšanje trajne dinamične trdnosti. V članku je predstavljena neposredna primerjava kart dovoljene velikosti napak. Gre za nov pristop, ki bo primeren tako za znanstveno skupnost kot za industrijo. Podan je predlog neposredno uporabne metode za računanje dovoljene velikosti napak po MKE pri kompleksnih komponentah. Uporabna bo za vse inženirje, ki se ukvarjajo s konstrukcijo, simulacijami ali kontrolo kakovosti, kakor tudi za livarje.

Ključne besede: visokociklično utrujanje, analiza po metodi končnih elementov, lomna mehanika, površinske napake, večosno utrujanje, nodularna litina

*Naslov avtorja za dopisovanje: Univerza za tehniko in ekonomijo v Budimpešti, Műegyetem rkp. 3, Budapest 1111, Madžarska, groza.marton@gt3.bme.hu

Strojniški vestnik - Journal of Mechanical Engineering 64(2018)6, SI 56

Prejeto v recenzijo: 2017-12-01
Prejeto popravljeno: 2018-03-29
Odobreno za objavo: 2018-04-26

Pripomoček po načelu plavutnega trna s pnevmatično mišico za rehabilitacijo zapestja

Ioana Petre – Andrea Deaconescu – Flavius Sârbu – Tudor Deaconescu*
Transilvanska univerza v Brasovu, Romunija

Za rehabilitacijo dlani se uporabljajo pripomočki, ki z razgibavanjem pospešijo vračanje specifičnih funkcij ter omogočajo gladko socialno reintegracijo pacientov z minimalnimi stroški. V pričujočem članku je v tem kontekstu predstavljen in obravnavan pripomoček s pnevmatično mišico, ki omogoča istočasno rehabilitacijo radiokarpalnega, metakarpofalangealnih in interfalangealnih sklepov.

Rehabilitacija zapestja se izvaja s pasivnim razgibavanjem, pri katerem je gibanje poškodovanega sklepa doseženo mehansko in brez obremenjevanja pacientovih mišic. To je možno s posebno opremo, ki omogoča optimalne gibe za rehabilitacijo zapestja.

Analizira opreme za rehabilitacijo zapestja na trgu je razkrila, da se pri obstoječih rešitvah mobilizira vsak sklep posebej. Večina opreme ima električni pogon, medtem ko so pnevmatski pogoni zanemarjeni. Avtorji članka so zato razvili nov pripomoček, ki istočasno mobilizira sklepe zapestja in prstov, za pogon pa uporablja pnevmatično mišico. Novost predlagane rešitve je tudi v konstrukciji opore za dlan, za katero navdih prihaja iz biologije oz. od trnov v ribjih plavutih. Prednost predlagane rešitve je v tem, da kompleksno gibanje različnih delov dlani pomaga pri izboljševanju mišičnega tonusa in stanja sklepov. Opisana oprema tako poleg blaženja sklepne bolečine pomaga tudi pri vzdrževanju oz. povečevanju vzdražljivosti mišic v zdravih segmentih.

Obravnavani rehabilitacijski sistem dosega mobilizacijo z zveznim istočasnim pasivnim razgibavanjem radiokarpalnega, metakarpofalangealnih in interfalangealnih sklepov. Pripomoček v vseh omenjenih sklepih reproducira fleksijo in ekstenzijo.

Rehabilitacijski pripomoček izpolnjuje zahteve, kot so kompaktnost konstrukcije in manjša masa za prenosljivost opreme, preprosto upravljanje in prijaznost do uporabnika, ter prilagodljivost glede na prag bolečine osebe na rehabilitaciji. Zadnja zahteva je izpolnjena s t.i. nastavljivimi podajnimi izvršnimi členi (ACA) za pogon opreme. Uporaba nastavljivih podajnih motorjev zagotavlja prilagodljivost rehabilitacijskega pripomočka vsakokratni delovni situaciji, ki je spremenljiva in odvisna od pacientovega praga bolečine.

V predstavljenem rehabilitacijskem pripomočku za sklepe dlani sta vgrajena dva vzporedna in togo povezana mehanizma tipa plavutnega trna, ki zagotavljata potrebno širino za pozicioniranje dlani. Gibanje rehabilitacijskega pripomočka se prenaša prek zobate letve s pnevmatično mišico kot linearnim motorjem, ki poganja letev za linearno recipročno gibanje.

Opravljene teoretične in eksperimentalne raziskave so pokazale, da rehabilitacijski pripomoček zagotavlja fleksijo in ekstenzijo radiokarpalnega, metakarpofalangealnih in interfalangealnih sklepov do meje gibljivosti zdrave dlani.

Prednost mobilizacije s pnevmatično mišico je v podajnosti rehabilitacijskega pripomočka, ki prispeva k prilagodljivosti sistema za individualen prag bolečine vsakega pacienta. Slabost uporabe pnevmatičnih mišic kot izvršnih členov je v histerezi, ki zmanjšuje točnost pozicioniranja mehanskega sestava za mobilizacijo sklepov. Ker pa ima pacientovo udobje pri rehabilitaciji sklepov dlani prednost pred točnostjo pozicioniranja, je predlagani pripomoček praktična alternativa za rehabilitacijsko opremo, ki je trenutno na voljo na trgu.

Ključne besede: podajnost, učinek plavutnega trna, pnevmatične mišice, pripomoček za rehabilitacijo zapestja

*Naslov avtorja za dopisovanje: Transilvanska univerza, 29 Eroilor Bd., Brasov, Romunija, tdeacon@unitbv.ro

Strojniški vestnik - Journal of Mechanical Engineering 64(2018)6, SI 57

Prejeto v recenzijo: 2017-12-30
Prejeto popravljeno: 2018-02-19
Odobreno za objavo: 2018-04-16

Nov hibridni sistem strojnega učenja in statistično razpoznavanje vzorcev z 3D grafi vidljivosti

Matej Babič[1,*] – Karolj Skala[2] – Dookhitram Kumar[3] – Roman Šturm[4]
[1] Inštitut Jožef Stefan, Slovenija
[2] Inštitut Ruđer Bošković, Hrvaška
[3] Tehniška univerza, Mauricius
[4] Univerza v Ljubljani, Fakulteta za strojništvo, Slovenija

Inteligentni sistemi so odlično orodje za reševanje zapletenih problemov na področju industrijskih aplikacij. V članku uporabljamo matematično metodo fraktalne geometrije in teorijo grafov pri tehniki laserskega kaljenja. Mikrostruktura robotsko-lasersko kaljenih vzorcev je zelo kompleksna; vendar jo lahko predstavimo z uporabo grafov vidljivosti v 3D prostoru. Mikrostrukturne slike rasterskega elektronskega mikroskopa (SEM) pretvorimo v 3D graf in izračunamo gostoto omrežja grafov vidljivosti v 3D prostoru. Topografske lastnosti kaljenih vzorcev analiziramo z uporabo algoritma za konstrukcijo grafov vidljivosti v 3D prostoru. Razvili smo nov hibridni sistem strojnega učenja za napovedovanje vsebnosti karbida v lasersko kaljenih vzorcih z uporabo multiple regresije, nevronskih mrež in genetskega programiranja. Ugotovili smo statistično signifikantnost med parametri laserske celice za kaljenje, topološkimi lastnosti grafov vidljivosti v 3D prostoru in vsebnosti karbidov v lasersko kaljenih vzorcih.

Prispevek predstavlja nov način konstrukcije grafov vidljivosti v 3D prostoru, nov način opisovanja kompleksnosti 3D prostora in nov hiperhibridni sistem strojnega učenja in njegovo uporabo v strojništvu za napovedovanje topografskih lastnosti robotsko lasersko kaljenih vzorcev. Prispevek predstavlja metodo uporabe grafov vidljivosti v 3D prostoru in fraktalno geometrijo za analizo kompleksnosti robotsko lasersko kaljenih vzorcev. Analiziranje kompleksnosti površin robotsko lasersko kaljenih vzorcev je zelo težavno. Ta nova metoda ima številne aplikacije pri prepoznavanju vzorcev, računalniški grafiki, računalniški geometriji in drugje.

Pokazali smo kako parametri hitrosti in temperature vplivajo na topološke lastnosti grafov vidljivosti v 3D prostoru. Izračunali smo statistične lastnosti topoloških lastnosti števila ekstremov, števila robov in triadnega popisa tipa 16-300 omrežja 3D vidljivosti za vzorce, ki so bili lasersko kaljeni. Najprej smo izračunali osnovne statistične lastnosti povprečje, standardni odklon, standardno napako, mediano, geometrijsko sredino in harmonično sredino topoloških lastnosti grafov vidljivosti v 3D prostoru robotsko lasersko kaljenih vzorcev. Ugotovili smo pomembna pozitivna razmerja med kurtozo, Fisherjevim G2, koeficientom variacije, koeficientom disperzije in topološkimi lastnostmi grafov vidljivosti v 3D prostoru robotsko lasersko kaljenih vzorcev.

Glavne ugotovitve je mogoče povzeti takole:

1. Za analizo mikrostrukture uporabljamo metodo teorije grafov in fraktalno geometrijo.
2. Za napovedovanje vsebnosti karbida v utrjenih vzorcih uporabljamo metode inteligentnih sistemov; nevronske mreže, multiplo regresijo in genetsko programiranje.
3. Predstavimo nov sekvenčni spiralni hibrid.
4. Prispevek uvaja novo metodo strojnega učenja v metalurgiji.
5. Ugotovili smo statistično signifikanco med parametri robotske laserske celice, med eksperimentalnimi in napovedanimi podatki.
6. V prispevku primerjamo tri metode inteligentnih sistemov, in sicer multiplo regresijo, nevronske mreže in genetsko programiranje, s hibridnim sistemom inteligentnih sistemov.

Ključne besede: fraktalna geometrija, hibridni sistem, lasersko kaljenje, graf vidljivosti, statistično razpoznavanje vzorcev

*Naslov avtorja za dopisovanje: Inštitut Jožef Stefan, Ljubljana, Slovenija, babicster@gmail.com

Strojniški vestnik - Journal of Mechanical Engineering 64(2018)6, SI 58

Prejeto v recenzijo: 2017-11-14
Prejeto popravljeno: 2018-02-01
Odobreno za objavo: 2018-02-14

Parametrična toplotna analiza trikotnih reber za izboljšan prenos toplote s prisilno konvekcijo

Saroj Yadav – Krishna Murari Pandey*
Nacionalni inštitut za tehnologijo Silchar, Assam, Indija

Namen predstavljene raziskave je izboljšanje toplotnega toka z zmanjšanjem tokovnih izgub v sistemu na minimum.

S ciljem učinkovitega odvajanja toplote iz delovnega prostora je bila opravljena študija s trikotnimi rebri različnih geometrij. Preučen je bil tudi vpliv Nusseltovega števila, koeficienta prenosa toplote, količnika trenja in količnika tlaka s spreminjanjem razporeditve, usmeritve in števila reber. Delo je bilo razdeljeno v več podsklopov.

1) Razvoj numeričnega 3D-modela cilindričnega rebra s programom za reševanje po MKE.
2) Validacija programa za reševanje z eksperimentalnimi in empiričnimi rezultati.
3) Toplotna in tokovna analiza trikotnih reber v različnih pogojih vsiljene konvekcije.

Eksperiment je bil postavljen z navpičnim kanalom pravokotnega prereza in aksialnim ventilatorjem. Zrak vstopa v kanal od spodaj in izstopa na vrhu. Sistem medsebojno zamaknjenih reber na osnovni plošči je povezan z grelnikom, ki greje spodnji del plošče. Rebra je mogoče skupaj z grelno enoto vložiti v testni odsek kanala. Rebra so v testnem odseku postavljena tako, da zrak priteka pravokotno glede na rebra. Na vhodu in na izhodu kanala so nameščena zaznavala, ki merijo temperaturo dovodnega in odvodnega zraka.

Rezultati in ugotovitve

- Pri konstantni vrednosti Reynoldsovega števila na vhodu daje medsebojno zamaknjena razporeditev reber skoraj 22-odstotno izboljšanje koeficienta prenosa toplote glede na razporeditev v vrsti.
- Rebra, ki so medsebojno zamaknjena in postavljena pod kotom 45° glede na smer zračnega toka, zagotavljajo večje vrednosti Nu in *h* kot vse ostale konfiguracije.
- Ugotovljeno je bilo tudi, da se s povečevanjem števila reber ne poveča nujno tudi toplotni tok. Konfiguracija 3-2-3 je učinkovita z ozirom na prenos toplote.
- Medsebojno zamaknjena rebra v tej študiji zagotavljajo večje vrednosti C_p in C_f kot rebra, ki so razporejena v vrsti.
- Rebra, ki so vzporedna s smerjo toka, so bolj aerodinamična in imajo manjše tlačne izgube. Pri usmeritvi reber pod kotom 0° se povečajo torne izgube. Sistem medsebojno zamaknjenih trikotnih reber pod kotom 45° glede na smer toka imajo prednost zaradi boljšega toplotnega toka.
- Konfiguracija 3-2-3 je optimalna v pogledu tornih izgub.

Študija prinaša napredek na področju trikotnih reber. Z numerično simulacijo je bilo izboljšano razumevanje prenosa toplote in tokovnih razmer na rebrih s trikotno geometrijo in omejeno dolžino pretočnega kanala do izhoda.

Glavni prispevek raziskave je v izboljšanem razumevanju fizike hlajenja z uporabo trikotnih krilc (reber) v elektronskih napravah, kjer je malo prostora.

Ključne besede: konjugiran prenos toplote, razširjene površine, metoda končnih elementov, koeficient prenosa toplote, Nusseltovo število, trikotna rebra

*Naslov avtorja za dopisovanje: Nacionalni inštitut za tehnologijo Silchar, Assam, Indija, kmpandey2001@yahoo.com

Strojniški vestnik - Journal of Mechanical Engineering 64(2018)6, SI 59

Prejeto v recenzijo: 2017-10-27
Prejeto popravljeno: 2018-03-20
Odobreno za objavo: 2018-03-21

Model za kompenzacijo trajektorije pri aplikacijah kolutnega robljenja

Eduardo Esquivel González[1,*] - José Pablo Rodríguez Arzate[2] - Giuseppe Carbone[3] - Marco Ceccarelli[3] - Juan Carlos Jáuregui[1]

[1] Avtonomna univerza v Querétaru, Tehniška fakulteta, Mehika
[2] Tehnološki inštitut v Celayi, Oddelek za mehatroniko, Mehika
[3] Univerza v Cassinu, Laboratorij za robotiko in mehatroniko, Italija

V članku je predstavljen model za kompenzacijo trajektorij, ki omogoča popravek odstopanj pri aplikacijah kolutnega robljenja. Roboti so cenovno ugodna rešitev za večino proizvodnih postopkov v avtomobilski industriji in so uporabni pri številnih nalogah, od pobiranja in odlaganja, lakiranja in zatesnjevanja pa do kompleksnejših nalog, kot je rezkanje ali varjenje. Serijski robot v postopku kolutnega robljenja premika kolut po konturi za pritrditev zunanjega vratnega panela na notranji vratni panel. Kolutno robljenje nudi določeno prilagodljivost, obenem pa se lahko pri tem postopku pojavijo različne napake v končni obliki panelov. Pogosta optična napaka je valovitost oz. gubanje prirobnice, ki je povezano s hitrostjo in silo koluta. Tovrstne napake so odvisne od zmogljivosti koluta za preoblikovanje panela v odvisnosti od položaja robota in končna kakovost panela se zato lahko spreminja vzdolž trajektorije. Večina študij postopka kolutnega robljenja se ukvarja z analizo po metodi končnih elementov in z napovedovanjem vzorcev deformiranja panela, le malo pa jih osvetljuje dinamično zmogljivost robota. V članku je zato predstavljen predlog kompenzacijske strategije za postopek kolutnega robljenja na osnovi spremenljive togosti robota, ki zmanjšuje odstopanja orodja vzdolž trajektorije na minimum.

Članek podaja predlog kompenzacijskega modela za kolutno robljenje s poudarkom na določanju togosti robota. Razvita je bila simulacija procesa in opravljeni so bili eksperimentalni testi za določitev napak v rezultatih. Uvedba te kompenzacijske strategije omogoča točnejšo rešitev in doseganje večje kakovosti izdelka. V poglavju o metodah je postavljen predlog za kompenzacijo trajektorije z analizo posameznih elementov in njihovim združevanjem v model za kompenzacijo trajektorije.

Rezultati kompenzacijske strategije s konstantno silo na vrhu robota so pokazali, da je lahko dejanski položaj na koncu trajektorije pod želenim položajem. Velikostni razred odstopanj je približno 4×10^{-3} mm, kar je majhna vrednost v primerjavi s položajem orodja in velikostjo delovnega prostora. Opravljena je bila tudi analiza rezultatov kompenzacijske strategije z variabilno silo. Izkazalo se je, da trajektorija med gibanjem koluta po pločevini zaradi majhne togosti leze proti negativnim vrednostim. V kompenzirani trajektoriji so bile upoštevane napake gubanja materiala, saj je bila vrednost sile določena eksperimentalno na osnovi vedenja panela. Rezultati meritev debeline panelov so pokazali, da je nekompenzirana trajektorija nekoliko nad referenčno z največjim odstopanjem debeline 2,1 mm, medtem ko je kompenzirana trajektorija bližje referenčni z največjim odstopanjem debeline 1,8 mm.

Razred napake pri kompenzacijski strategiji je znašal 1×10^{-3} mm in temu morajo ustrezati tudi zmogljivosti robota. Točnost položaja središča orodja pri robotu Fanuc 200IC je npr. 1×10^{-2} mm in to pomeni, da je ta robot omejen pri izvajanju opisane kompenzacijske strategije. Na uspešnost kompenzacije vpliva tudi točnost predhodnega procesa. V prihodnje raziskave bo zato treba vključiti tudi notranje napetosti v materialu zaradi predhodnih procesov, simulacijo po MKE in analizo občutljivosti spremenljivk.

Članek obravnava glavne probleme pri postopku kolutnega robljenja in kompenzacijsko strategijo na osnovi spremenljive sile. V predlog kompenzacije je vključena metoda za določanje odstopanj zaradi robota in odstopanj zaradi panela. Rezultati kažejo izboljšanje velikostnega reda 1 mm. Avtorji članka menijo, da bi bilo mogoče z dopolnitvijo in uvedbo modela v industrijski proizvodnji zagotoviti popolno rešitev za tehnologijo kolutnega robljenja, saj je simulacija z eksperimentalnimi podatki pokazala, da popravki trajektorije med izvajanjem postopka dajejo dobre rezultate.

Ključne besede: kolutno robljenje, gubanje, središče orodja, togost, trajektorija, kompenzacija

*NAslov avtorja za dopisovanje: Avtonomna univerza v Querétaru, Tehniška fakulteta, Cerro de las campanas S/N, Querétaro, Mehika, je.esquivel@outlook.com

Information for Authors

All manuscripts must be in English. Pages should be numbered sequentially. The manuscript should be composed in accordance with the Article Template given above. The maximum length of contributions is 10 pages. Longer contributions will only be accepted if authors provide juastification in a cover letter. For full instructions see the Information for Authors section on the journal's website: http://en.sv-jme.eu .

SUBMISSION:

Submission to SV-JME is made with the implicit understanding that neither the manuscript nor the essence of its content has been published previously either in whole or in part and that it is not being considered for publication elsewhere. All the listed authors should have agreed on the content and the corresponding (submitting) author is responsible for having ensured that this agreement has been reached. The acceptance of an article is based entirely on its scientific merit, as judged by peer review. Scientific articles comprising simulations only will not be accepted for publication; simulations must be accompanied by experimental results carried out to confirm or deny the accuracy of the simulation. Every manuscript submitted to the SV-JME undergoes a peer-review process.

The authors are kindly invited to submit the paper through our web site: http://ojs.sv-jme.eu. The Author is able to track the submission through the editorial process - as well as participate in the copyediting and proofreading of submissions accepted for publication - by logging in, and using the username and password provided.

SUBMISSION CONTENT:

The typical submission material consists of:
- A **manuscript** (A PDF file, with title, all authors with affiliations, abstract, keywords, highlights, inserted figures and tables and references),
- Supplementary files:
  - a **manuscript** in a WORD file format
  - a **cover letter** (please see instructions for composing the cover letter)
  - a ZIP file containing **figures** in high resolution in one of the graphical formats (please see instructions for preparing the figure files)
  - possible **appendicies** (optional), cover materials, video materials, etc.

Incomplete or improperly prepared submissions will be rejected with explanatory comments provided. In this case we will kindly ask the authors to carefully read the Information for Authors and to resubmit their manuscripts taking into consideration our comments.

COVER LETTER INSTRUCTIONS:

Please add a **cover letter** stating the following information about the submitted paper:
1. Paper **title**, list of **authors** and their **affiliations**.
2. **Type of paper**: original scientific paper (1.01), review scientific paper (1.02) or short scientific paper (1.03).
3. A **declaration** that neither the manuscript nor the essence of its content has been published in whole or in part previously and that it is not being considered for publication elsewhere.
4. State the **value of the paper** or its practical, theoretical and scientific implications. What is new in the paper with respect to the state-of-the-art in the published papers? Do not repeat the content of your abstract for this purpose.
5. We kindly ask you to suggest at least two **reviewers** for your paper and give us their names, their full affiliation and contact information, and their scientific research interest. The suggested reviewers should have at least two relevant references (with an impact factor) to the scientific field concerned; they should not be from the same country as the authors and should have no close connection with the authors.

FORMAT OF THE MANUSCRIPT:

The manuscript should be composed in accordance with the Article Template. The manuscript should be written in the following format:
- A **Title** that adequately describes the content of the manuscript.
- A list of **Authors** and their **affiliations**.
- An **Abstract** that should not exceed 250 words. The Abstract should state the principal objectives and the scope of the investigation, as well as the methodology employed. It should summarize the results and state the principal conclusions.
- 4 to 6 significant **key words** should follow the abstract to aid indexing.
- 4 to 6 **highlights;** a short collection of bullet points that convey the core findings and provide readers with a quick textual overview of the article. These four to six bullet points should describe the essence of the research (e.g. results or conclusions) and highlight what is distinctive about it.
- An **Introduction** that should provide a review of recent literature and sufficient background information to allow the results of the article to be understood and evaluated.
- A **Methods** section detailing the theoretical or experimental methods used.
- An **Experimental section** that should provide details of the experimental set-up and the methods used to obtain the results.
- A **Results** section that should clearly and concisely present the data, using figures and tables where appropriate.
- A **Discussion** section that should describe the relationships and generalizations shown by the results and discuss the significance of the results, making comparisons with previously published work. (It may be appropriate to combine the Results and Discussion sections into a single section to improve clarity.)
- A **Conclusions** section that should present one or more conclusions drawn from the results and subsequent discussion and should not duplicate the Abstract.
- **Acknowledgement** (optional) of collaboration or preparation assistance may be included. Please note the source of funding for the research.
- **Nomenclature** (optional). Papers with many symbols should have a nomenclature that defines all symbols with units, inserted above the references. If one is used, it must contain all the symbols used in the manuscript and the definitions should not be repeated in the text. In all cases, identify the symbols used if they are not widely recognized in the profession. Define acronyms in the text, not in the nomenclature.
- **References** must be cited consecutively in the text using square brackets [1] and collected together in a reference list at the end of the manuscript.
- **Appendix(-icies)** if any.

SPECIAL NOTES

Units: The SI system of units for nomenclature, symbols and abbreviations should be followed closely. Symbols for physical quantities in the text should be written in italics (e.g. v, T, n, etc.). Symbols for units that consist of letters should be in plain text (e.g. ms^{-1}, K, min, mm, etc.). Please also see: http://physics.nist.gov/cuu/pdf/sp811.pdf .

Abbreviations should be spelt out in full on first appearance followed by the abbreviation in parentheses, e.g. variable time geometry (VTG). The meaning of symbols and units belonging to symbols should be explained in each case or cited in a **nomenclature** section at the end of the manuscript before the References.

Figures (figures, graphs, illustrations digital images, photographs) must be cited in consecutive numerical order in the text and referred to in both the text and the captions as Fig. 1, Fig. 2, etc. Figures should be prepared without borders and on white grounding and should be sent separately in their original formats. If a figure is composed of several parts, please mark each part with a), b), c), etc. and provide an explanation for each part in Figure caption. The caption should be self-explanatory. Letters and numbers should be readable (Arial or Times New Roman, min 6 pt with equal sizes and fonts in all figures). Graphics (submitted as supplementary files) may be exported in resolution good enough for printing (min. 300 dpi) in any common format, e.g. TIFF, BMP or JPG, PDF and should be named Fig1.jpg, Fig2.tif, etc. However, graphs and line drawings should be prepared as vector images, e.g. CDR, AI. Multi-curve graphs should have individual curves marked with a symbol or otherwise provide distinguishing differences using, for example, different thicknesses or dashing.

Tables should carry separate titles and must be numbered in consecutive numerical order in the text and referred to in both the text and the captions as Table 1, Table 2, etc. In addition to the physical quantities, such as t (in italics), the units [s] (normal text) should be added in square brackets. Tables should not duplicate data found elsewhere in the manuscript. Tables should be prepared using a table editor and not inserted as a graphic.

REFERENCES:

A reference list must be included using the following information as a guide. Only cited text references are to be included. Each reference is to be referred to in the text by a number enclosed in a square bracket (i.e. [3] or [2] to [4] for more references; do not combine more than 3 references, explain each). No reference to the author is necessary.

References must be numbered and ordered according to where they are first mentioned in the paper, not alphabetically. All references must be complete and accurate. Please add DOI code when available. Examples follow.

Journal Papers:

Surname 1, Initials, Surname 2, Initials (year). Title. Journal, volume, number, pages, DOI code.

[1] Hackenschmidt, R., Alber-Laukant, B., Rieg, F. (2010). Simulating nonlinear materials under centrifugal forces by using intelligent cross-linked simulations. *Strojniški vestnik - Journal of Mechanical Engineering,* vol. 57, no. 7-8, p. 531-538, DOI:10.5545/sv-jme.2011.013.

Journal titles should not be abbreviated. Note that journal title is set in italics.

Books:

Surname 1, Initials, Surname 2, Initials (year). Title. Publisher, place of publication.

[2] Groover, M.P. (2007). *Fundamentals of Modern Manufacturing*. John Wiley & Sons, Hoboken.

Note that the title of the book is italicized.

Chapters in Books:

Surname 1, Initials, Surname 2, Initials (year). Chapter title. Editor(s) of book, book title. Publisher, place of publication, pages.

[3] Carbone, G., Ceccarelli, M. (2005). Legged robotic systems. Kordić, V., Lazinica, A., Merdan, M. (Eds.), Cutting Edge Robotics. Pro literatur Verlag, Mammendorf, p. 553-576.

Proceedings Papers:

Surname 1, Initials, Surname 2, Initials (year). Paper title. Proceedings title, pages.

[4] Štefanić, N., Martinčević-Mikić, S., Tošanović, N. (2009). Applied lean system in process industry. *MOTSP Conference Proceedings*, p. 422-427.

Standards:

Standard-Code (year). Title. Organisation. Place.

[5] ISO/DIS 16000-6.2:2002. *Indoor Air – Part 6: Determination of Volatile Organic Compounds in Indoor and Chamber Air by Active Sampling on TENAX TA Sorbent, Thermal Desorption and Gas Chromatography using MSD/FID.* International Organization for Standardization. Geneva.

WWW pages:

Surname, Initials or Company name. Title, from http://address, date of access.

[6] Rockwell Automation. Arena, from *http://www.arenasimulation.com,* accessed on 2009-09-07.

EXTENDED ABSTRACT:

When the paper is accepted for publishing, the authors will be requested to send an **extended abstract** (approx. one A4 page or 3500 to 4000 characters). The instruction for composing the extended abstract are published on-line: http://www.sv-jme.eu/information-for-authors/ .

COPYRIGHT:

Authors submitting a manuscript do so on the understanding that the work has not been published before, is not being considered for publication elsewhere and has been read and approved by all authors. The submission of the manuscript by the authors means that the authors automatically agree to transfer copyright to SV-JME when the manuscript is accepted for publication. All accepted manuscripts must be accompanied by a Copyright Transfer Agreement, which should be sent to the editor. The work should be original work by the authors and not be published elsewhere in any language without the written consent of the publisher. The proof will be sent to the author showing the final layout of the article. Proof correction must be minimal and executed quickly. Thus it is essential that manuscripts are accurate when submitted. Authors can track the status of their accepted articles on http://en.sv-jme.eu/.

PUBLICATION FEE:

Authors will be asked to pay a publication fee for each article prior to the article appearing in the journal. However, this fee only needs to be paid after the article has been accepted for publishing. The fee is 320 EUR (for articles with maximum of 6 pages), 400 EUR (for articles with maximum of 10 pages), plus 40 EUR for each additional page. The additional cost for a color page is 90.00 EUR. These fees do not include tax.

Strojniški vestnik -Journal of Mechanical Engineering
Aškerčeva 6, 1000 Ljubljana, Slovenia,
e-mail: info@sv-jme.eu

9 770039 248001
ISSN 0039-2480

http://www.sv-jme.eu

Contents

Papers